Quantitative Nanoscopy of Synaptic Sites

Dissertation

for the award of the degree

“Doctor rerum naturalium”

of the Georg-August-Universität Göttingen

within the doctoral program Cellular and Molecular Physiology of the Brain (CMPB)

and the Max-Planck-School Matter to Life (MPS-MtL)

of the Georg-August University School of Science (GAUSS)

submitted by

Clara-Marie Gürth

from Dresden

Göttingen 2022

Members of the Thesis Committee

Prof. Dr. Dr. h.c. mult. Stefan W. Hell (Referee)
Department of NanoBiophotonics
Max Planck Institute for Multidisciplinary Sciences
Department of Optical Nanoscopy
Max Planck Institute for Medical Research

Prof. Dr. Silvio O. Rizzoli (Referee)
Department of Neuro- and Sensory Physiology
University Medical Center Göttingen

Prof. Dr. Christian Tetzlaff
Institute for Neuro- and Sensory Physiology
Department of Computational Synaptic Physiology
University Medical Center Göttingen

Dr. Elisa D'Este
Head of the Optical Microscopy Facility
Max Planck Institute for Medical Research

Additional Members of the Exam Committee

Prof. Dr. Hauke Werner
Neurochemistry Group
Department of Neurogenetics
Max Planck Institute for Multidisciplinary Sciences

Prof. Dr. Thomas Dresbach
Department of Anatomy and Embryology
University Medical Center Göttingen

Oral examination: Göttingen, 25.08.2022

Summary

Synapses are the basic information processing unit of the brain. Neuronal activity and memory formation thereby require a vastly dynamic and rapidly changing synaptic environment and composition. In order to function, these changes need to be finely regulated and tailored to specific needs of individual synapses. How synaptic composition and function are connected and regulated is so far not fully understood.

New optical imaging techniques such as STED and MINFLUX nanoscopy have enabled to investigate the synaptic environment with molecular specificity at so far unprecedented detail. While qualitative measures become increasingly available, quantitative analyses in nanoscopic imaging data are still challenging. Precise quantitative measures are essential to shed light into vastly heterogenous populations such as synapses as well as complex dynamic processes such as synaptic plasticity.

To this aim different aspects of the synaptic composition and environment were quantitatively characterized within the context of synaptic activity combining different nanoscopy methods and implementing different labelling strategies.

Firstly, the presence and distribution of secretory pathway elements in synaptic proximity was quantified within the context of markers of synaptic strength and activity. This analysis revealed the tools single synapses potentially utilize for local protein synthesis or delivery and how these depend on both increased strength and activity.

Secondly, the content of cytoskeletal neurofilaments was quantified within postsynaptic spines with respect to the synaptic status. Here it was shown how different neurofilament isoforms depend differentially on both strength and activity of the individual synapse.

Thirdly, the regulation of the postsynaptic scaffolding protein PSD-95 was characterised at the single synapse level. Here gene editing tools combined with pulse-chase labelling approaches added temporal information to imaging data, enabling to visualise protein turnover at the nanoscale, while imaging with three-dimensional molecular resolution, revealed the structural rearrangements during synaptic plasticity.

Taken together this work combines different advanced imaging techniques, implements labelling tools and image analysis workflows to quantify how activity impacts the organization and composition of postsynaptic sites to better understand mechanisms of synaptic plasticity.

Acknowledgements

Science is never a lonely endeavour and also the work presented in this thesis is the result of fruitful teamwork and collaboration. I have been fortunate to receive support, guidance, and inspiration from so many people during this past three and a half years. I would like to acknowledge the contribution of everyone involved on a scientific professional or personal level who have made this journey such a special experience. In particular I would like to highlight the contribution of some people who made this thesis possible.

Firstly, I would like to express my gratitude to Stefan W. Hell who allowed me to be a part of this wonderful team of researchers and for giving me the opportunity to perform my PhD research in his labs. Thank you so much for your trust and for allowing me to explore such exciting projects. You put me in this extraordinary team and let me grow to who I am now and you had my back throughout the entire time.

Further I would like to thank the members of my thesis committee Silvio O. Rizzoli and Christian Tetzlaff. I very much valued your input, encouragement, and critical questions during our meetings. Thank you both for making sure that I stayed on track and for allowing me to learn so much from you and your group members. Your enthusiasm for synaptology and your sometimes humorous takes on the obstacles we faced were very inspiring to me.

My special thanks belong to Elisa D’Este who guided me along the path of the PhD. Thank you for all your encouragement, ideas, trust, patience, and direction whenever I needed it. I appreciated how you involved me in everything along the way, how you gave me advice on more than project related issues, and how you gave me the freedom that has made this time such an educational experience.

I would like to acknowledge my graduate schools Cellular and Molecular Physiology of the Brain and the Max-Planck-School Matter to Life that gave me support and so many possibilities to learn and broaden my horizon. It is a privilege to be a part of such an inspiring network of scientists.

I am grateful to Tal Dankovich for our close collaboration during the pandemic. Thank you for teaming up with me on this project for this intensive, productive time. I enjoyed very much working together with you.

My thanks belong to all current and former members of the optical nanoscopy department. I am well aware how fortunate I am being a part of this wonderful research family. Many of us are taking this journey together and I was great sharing experiences or learning from each other over coffee or food. You all have made this PhD a wonderful adventure for me and it feels far too soon that the time has already come for me to move on and leave. I could have gone on like this forever and hope that all our paths will cross again.

Many aspects of this thesis would not exist if it wasn’t for the support of our neuro-team. Victor and Angel, I had so much fun working with you and taking the PhD journey together with you. Thank you

so much, Jasmine, for teaching me, for involving me in all the lab-fun, for taking over the things I could not handle, and for always having an open ear.

Thank you, Maria, for your support and for paving the way through my jungle of data. I am amazed how many things you made possible. Teaming up with you was a great pleasure and really admire your passion for code.

Thank you, Jessi, you brought me on board 6 years ago and I look back on the countless great memories we got along the way. Your advice has really helped me so many times and I look forward to being on the same team again.

Moreover, I want to thank my family for their support, not only during this PhD time but also throughout my entire academic journey. Without your encouragement, help, and understanding I would not be where I am today. I am especially thankful to my partner Gregor. You supported me in so many ways and you took so much load off my shoulders. You believing in me is an immense source of strength and without you this thesis would look very different.

Thank you all for your support.

Contents

Chapter 1 – Introduction and Overview

"Ideas do not last long. Something has to be done with them."

Santiago Ramon Y Cajal

At the heart of scientific progress are advances in techniques and methodology that enable scientist to face new challenges. Various breakthroughs in biological research have been made thanks to the contribution of ever improving light microscopy methods. Although microscopy has been present already in the earliest days of scientific research, its constant development and progress in methodology have made it remain one of the key techniques in research until today (Hell 2015). Second only to the high spatial resolution of electron microscopy, its high molecular specificity, and the possibility to study dynamic processes in their physiological environment have kept fluorescence microscopy a go to technique. Already early on, progressing accumulation of discoveries let to the constant demand of better resolution. This was the main objective in the improvement of microscopes in the following centuries. These improvements included among others the optimisation of light sources for sample illumination or adaption of lens composition to reduce chromatic aberrations and the development of protocols to selectively visualise cellular features. Nonetheless, for decades the diffraction limit set an insuperable barrier to the performance of optical microscopy.

Since the turn of the millennium new fluorescent microscopy methods have revolutionized the field by allowing to study objects smaller than the resolution limit of light microscopy as defined by the diffraction barrier of light. These breakthroughs in optical microscopy have made it possible to study processes at the nanoscale with high molecular specificity and even in living tissues and cells which enabled many new discoveries.

Optical nanoscopy led to the discovery of – among many others – mitochondrial substructures and membrane dynamics (Große et al. 2016), the characterization of the nuclear pore structure (Szymborska et al. 2013), heterochromatin architecture, HIV maturation processes, or centriole and nuclear structures (all reviewed in Sahl et al. 2017; Sigal et al. 2018).

These new developments have been of special interest to the fields of neurobiology due the discovery of a periodic actin cytoskeleton in neuronal cells (Xu et al. 2013; D'Este et al. 2015). Synaptology also benefitted from the nanoscopy since conventional microscopes cannot resolve most neuronal and synaptic features (Owald et al. 2010).

In the following chapter, I describe the beginnings of microscopy in the last centuries and the development of new nanoscopy principles during the last decades towards optical microscopy capable of achieving single digit nanometre resolution. I briefly highlight the basic principles with a focus on STED and MINFLUX nanoscopy which were applied in the studies within the framework of this dissertation on the investigation and quantification of synaptic characteristics at the nanoscale. Thereafter, I will introduce synapses, the subject of my studies, and how nanoscopy fostered research in this field.

The early history of optical microscopy

The first appearance of the magnification of small objects with a lens dates back already to the 16th century. At this point the word microscope had not been termed yet and the biological unit of a cell was not discovered. Possibly the first men to construct a magnifying tool resembling what we would call a microscope today were Hans and Zacharias Jansen - Dutch lens makers, who combined two glass lenses in a first compound microscope already before 1600 (Wollman et al. 2015; Saka 2014). Galileo Galilei had shortly after invented a construct of two lenses to collect light and magnify objects in 1609, which was then later called microscope for the first time by Giovanni Faber in 1625 (Wollman et al. 2015). In the 1660s Robert Hooke applied versions of these compound microscopes with elaborate illumination systems to first observe and describe different biological specimen such as insects or plant material which he illustrated and published in the "Micrographia" in 1665. Hooke developed a way to prepare thin samples from cork that he illuminated at an angle and saw its composition from separate segments that he then termed "cells". Thereby he paved the way of biological understanding at the time (Gest 2009).

His contemporary, Antony van Leeuwenhoek similarly made early observations on biological samples however with a very different technique. He built several hundreds of optical devices that in essence all consisted of one single spherical lens in a small aperture with adjustable pins as specimen holders. This single lens handheld microscope allowed him to observe living biological specimen with even higher resolution than compound microscopes could achieve at this time. Thereby he managed to observe moving protozoa, bacteria, blood or muscle cells, and sperm at for the time unmatched detail. Despite their simple structure, such single lens instruments are still used today as they provide a portable, robust, and low-cost alternative to other more elaborate light microscopes (Cybulski et al. 2014).

A similar microscopic setup with a single lens was also used by the botanist Robert Brown in the 19th century for his botanical observations and his discovery of the nucleus in plant cells. Next to biological samples he also investigated inorganic material and observed their common random movement of particles today known as Brownian motions (Gray 2001).

The superiority of single lens microscopes at that time was in their limited chromatic and spherical aberrations, which multiply with the addition of more lenses in compound microscopes. However, the pioneering works of Carl Zeiss, Ernst Abbe, Otto Schott, and August Köhler brought major improvements to microscopic setups in the 19th century, reducing some of these flaws. Zeiss enhanced microscope systems, by improving manufacturing and quality standards, and by standardizing lens designs based on calculations of his colleague Abbe. Abbe calculated the theoretical basis of microscope optics based on refractive index and aperture. As a lens designer he developed the apochromat to correct for chromatic aberration. These specialized lenses were made possible by Schotts progress in glass science. His expertise enabled to control the optical properties of glass, and thereby modulate the refractive index of manufactured lenses. Köhler improved the illumination system of the microscope that set the basis for transmission light microscopy (Wimmer 2017; Masters 2007).

Next to the developments in designing optical setups, the major driving force of advances in microscopy methods was the growing expertise and developments in the preparation and labelling of biological specimen. A fundamental problem in the investigation of biological samples is that they usually lack contrast. Most cellular features are nearly transparent and share a similar refractive index which makes them indistinguishable in bright field and phase contrast microscopy. Investigations with optical microscopy have only been made possible by the introduction of contrast-enhancing protocols. Already early on, efforts have been made to distinguish biological structures based on selective staining.

Among the earliest was the method developed in 1873 by Camillo Golgi a silver staining method that enabled the visualisation of neurons in brain tissue, on which Ramon y Cajal based most of his neuroanatomical discoveries such as dendritic spines (**Fig. 1**). Shortly after Hans Christian Gram developed in 1884 a bacterial stain that stained bacterial cell wall and thereby set the fundament for bacterial classification. Such contrast enhancing dyes are still widely applied today in histology and medical routine diagnostics, however the utilisation of fluorescent stains revolutionised microscopical applications.

Besides chromophores, the introduction of fluorescent labelling has introduced even higher contrast and specificity making fluorescent microscopy the most popular microscopy method today. The fluorescence concept was first reported in the 19th century by John Herschel and George Gabriel Stokes (Stokes 1852), and already in the beginning of the 20th century the first fluorescence microscopes were produced. Since then different variants of fluorescence microscopes were developed all taking advantage of the excellent contrast enhancing properties of fluorescent labels. Among these labels are most popular immunofluorescent labelling with antibodies, and the discovery and utilization of the green fluorescent protein (GFP) which was a milestone especially for the observation of proteins in living samples (Shimomura 2009).

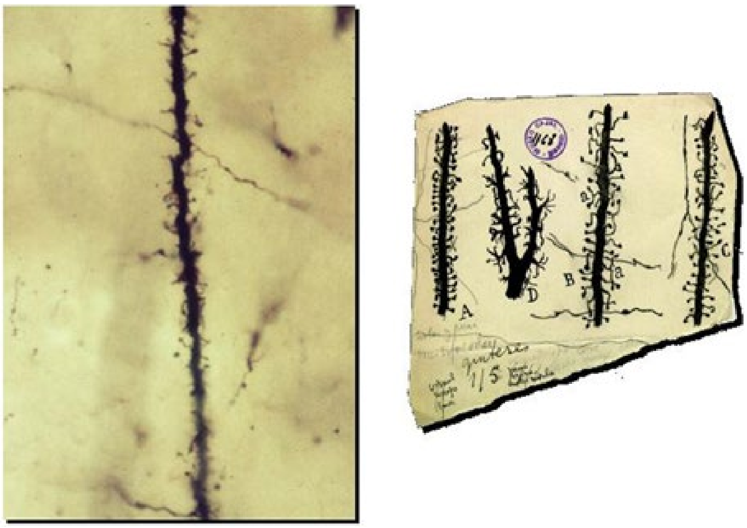

Figure 1. The Golgi method and Cajals discovery of dendritic spines
Adopted from Yuste 2015 by curtesy of the Cajal Institute Madrid. A silver staining protocol developed by Golgi and adopted by Cajal allowed for the selective labelling of single neurons in brain tissue. The photomicrograph (left) and respective drawings of Cajal (right) show individual labelled dendrites in different species with their protruding dendritic spines.

General principles, resolution, and the diffraction barrier

Despite several improvements in precision and execution, the working principle of optical microscopes still remains the same today. Optical microscopes operate in the far field and focus light through lenses to resolve structures in the focal plane. Technical improvements on the fabrication and handling of a microscope can enhance its ability to resolve small structures, however only up to a certain point.

Therefore, until the end of the 20th century, optical microscopy was limited in its resolution due to diffraction. The basic principle of diffraction is that an optical lens cannot focus light to an infinitely small point, which is due to the fact that light propagates as a wave.

Already in 1873, Ernst Abbe described how the performance of a microscope is limited by the diffraction of light when it passes through openings and thereby sets a barrier to the spatial resolution of a microscope (Abbe 1873). The resolution is hereby the minimum distance between two separate structures that can be distinguished as individual elements. The diffraction barrier that Abbe described limits the resolution of a microscope to half the wavelength of light, corresponding to 200-300 nm in the range of visible light. Hence, light with shorter wavelength results in better resolved structures. Von Helmholtz determined the lateral resolution based on Abbes descriptions in the following formula (Helmholtz 1874):

$$d \approx \frac{\lambda}{2n \sin \alpha}$$

where λ is the wavelength of the used light, n is the diffractive index of the immersion medium and alpha is the angle of the objective lens aperture. $n \sin \alpha$ also corresponds to the numerical aperture, a property of objective lenses. Considering an optimal refractive index, the best possible resolution of a microscope can be achieved by short wavelength of light, and high numerical aperture lenses. This results in a maximum theoretical resolution of ~200 nm, which is in practice even reduced by sample characteristics and optical aberration. Therefore, resolution can be estimated to 200-250 nm. In axial direction the resolution is described by the formula:

$$d \approx \frac{2\lambda}{n^2 sin^2 \alpha}$$

consequently, resulting in a maximum axial resolution of around 500 nm. For the case of fluorescence microscopy this means that within a diffraction limited illumination spot, usually multiple fluorescent molecules are being excited simultaneously. Hence a distinction of these simultaneously excited fluorophores is made impossible. Additionally, diffraction occurs again on the level of detection since also on a detector or camera emission light is projected as diffraction limited spot. Thereby each individual fluorescent molecule emits to one diffraction limited spot on the detection side. Since the diffraction limited spots overlap it is impossible to discern molecules lower than the diffraction barrier. As a result, the minimum distance of two discernible spots described as the Rayleigh criterion is a measure of resolution for optical microscopes. This blurred diffraction pattern created by a spot source of light was first described by George Biddell Airy (Airy 1835). He described the characteristics of the diffraction pattern with a centre interference maximum (Airy disk) and the surrounding diffraction rings (Airy pattern). This intensity pattern that is produced in the image plane by a point source of light can similarly be described by the so-called point spread function (PSF) together with its full width half maximum (FWHM) which today is commonly used to characterise the performance of an optical microscope (Pawley 2010).

Nanoscopy methods and the developments towards single digit nanometre resolution

Abbes resolution theory was long believed to be the ultimate limit of light microscopy until the beginning of the 21st century, when it has been shown that is possible to overcome this limit with the help of physics and physical chemistry. These development of microscopy techniques which break the diffraction barrier and transform microscopy into nanoscopy was awarded with the Nobel prize in chemistry in 2014.

As a first method to be demonstrated, stimulated emission depletion (STED) microscopy proved that it is possible to achieve a spatial resolution of about 20 nm which is around 10 times larger than conventional methods. In STED, stimulated emission keeps fluorescent molecules in the ground state (**Fig. 2A**). This is achieved by making use of molecular transitions through a beam of light which pushes excited molecules back to the ground state, simultaneously emitting two photons at the same wavelength of the depletion beam (Hell and Wichmann 1994, **Fig. 2B**). The depletion beam is doughnut shaped with an intensity minimum at the centre. Therefore, only the molecules in the periphery of the excitation spot are affected by the depletion beam, resulting in an emission pattern below the diffraction limit. Furthermore, the steepness of the intensity zero, and therefore the size of the effective PSF, can be modulated by tuning the power of the STED laser (**Fig. 2C**). Additionally, to Abbes original formula for the diffraction limit, now the resolution is determined by the light intensity distribution I, the saturation intensity I_{sat}, and b as the shape of the donut intensity zero, resulting in the following formula:

$$d = \frac{\lambda}{2n \sin \alpha \sqrt{1 + b \, \frac{I}{I_{sat}}}}$$

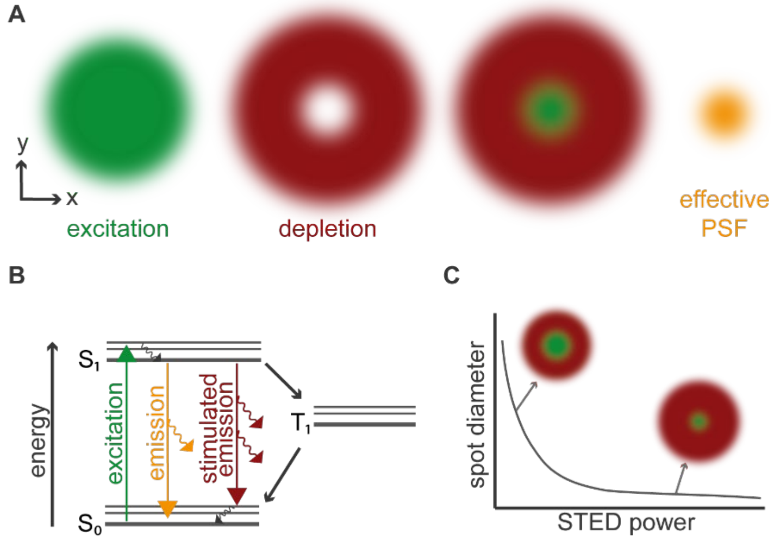

Figure 2. The principle of a STED microscope
(A) Light pattern of the diffraction limited excitation (green) and depletion (red) beams of a STED microscope, resulting in an effective emission spot (orange) smaller than the diffraction limit. (B) Simplified Jablonski diagram with the molecular energy states in STED microscopy, including singlet ground state (S0), first excited state (S1), and triplet state (T1). (C) The intensity of the STED laser determines the size of the zero-intensity spot in the centre and thereby the resolution.

At the beginning of the 2000s, other concepts to break the Abbe diffraction limit by relying on the visualization of single molecules were developed and demonstrated. The common feature of these techniques is the use of molecular transitions of fluorophores to switch between a non-fluorescent and a fluorescent state. By preparing the sample to have the majority of molecules in a non-fluorescent state and allowing only a subset of fluorophores to emit light, emitters are distinguishable over time in a stochastic manner. With a camera detector the position of the emission light of individual emitters can be determined and the more precise coordinate can be calculated based on the PSF. Depending on the molecular transition utilized for the switching of molecules, different approaches have been implemented, with the first ones being photoactivated localization microscopy (PALM and FPALM), that use photoactivatable fluorescent proteins (Hess et al. 2006; Betzig et al. 2006), stochastic optical reconstruction microscopy (STORM), which uses a fluorescence resonance energy transfer (FRET) pair (Rust et al. 2006), ground-state depletion microscopy (GSDIM), which benefits from the triplet state of fluorophores (Fölling et al. 2008), and dSTORM, relying on the direct blinking of the dyes (Heilemann et al. 2008). For these approaches, the theoretical diffraction limit is amended by the number of collected photons *N* resulting in the following formula:

$$d = \frac{\lambda}{2n \sin \alpha \sqrt{N}}$$

Now-a-day several nanoscopy techniques exist, that all can be generalized into coordinate-targeted approaches - such as STED - and coordinate-stochastic approaches – such as the single molecule approaches PALM and STORM (Hell 2007). Both approaches share one common principle: the distinction of neighbouring fluorophores via on and off switching. Their basic element is therefore the transition of fluorescent molecules from a non-fluorescent to a fluorescent state. From a theoretical point of view, the previously described nanoscopy methods are diffraction unlimited and should be able to achieve molecule size resolution. However, in practice, resolutions are rarely better than 20 nm, although some exceptions in special conditions, with specific fluorophores or in solid state, achieved resolutions down to the single nanometre regime (Arroyo-Camejo et al. 2013). This is not a general case due to limiting factors such as fluorophore bleaching, finite number of photons that a molecule can emit, background, and limited laser power.

While in PALM/STORM many photons are required from the emitter to determine the position of the molecule, in STED many photons are required from the laser to switch off the fluorophores. While in the latter case the laser can provide an infinite number of photons, the first case is problematic since fluorescent probes have a limited photon budget and can bleach or turn into a dark state. On the other hand, single molecule localizations routinely achieve higher localization precisions than STED.

In more recent years MINFLUX has aimed to combine the strengths of the different nanoscopy strategies in a new concept with increased photon efficiency (Balzarotti et al. 2017). In this technique single emitters are being localised via an excitation pattern with a central intensity zero which is iterated over the molecule position (**Fig. 3A**). MINFLUX still relies on single molecules but defines their localization by using a pattern of light featuring an intensity zero, such as a doughnut, to determine the localization by excitation instead of depletion. Thereby this method circumvents the limitations of previous methods, especially the limited photon budget of fluorophores. Indeed, in theory if a molecule is at the centre of the doughnut, it will not be excited but its localization can still be determined with high precision since the position of the doughnut is known. In practice, few photons are needed to localize the molecule and MINFLUX measures only the fluorescence that is emitted when the doughnut is slightly off-centred, and therefore excites the molecule with low laser intensities. The exact position of the emitting fluorophore is estimated by slightly displacing the light pattern by a distance L near the emitter and interpolating the number of photons collected for the individual exposures (**Fig. 3B**). It thereby aims to localize single molecules with minimum excitation and emission and hence with a minimum of photons from the fluorescent molecules. This brings the additional benefit that this method is wavelength independent, and the main factor determining the localization precision is L. MINFLUX uses 20-100 fewer detections to achieve a high localization precision compared to PALM/STORM. Furthermore, MINFLUX can also be used for tracking of molecules with high spatial and temporal resolution (<1 ms).

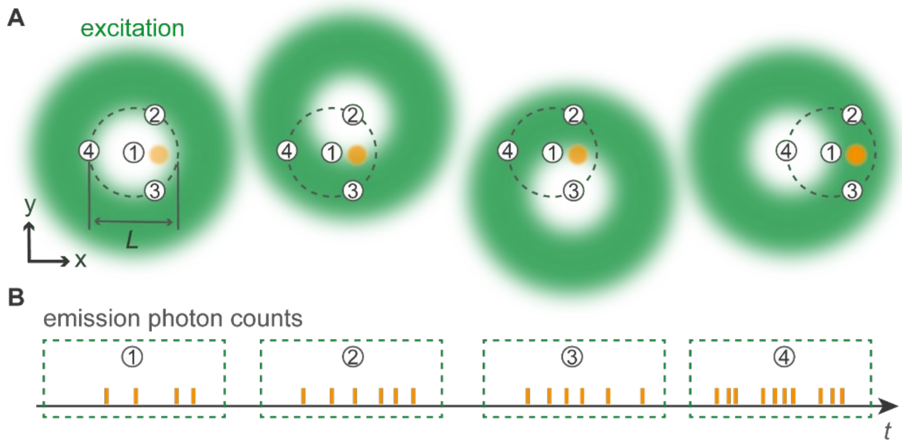

Figure 3. The MINFLUX principle
(A) The combined aspects of targeted and stochastic approach of MINFLUX with a single molecule emitter (orange) that is localises via the intensity minimum of a doughnut shaped excitation beam (green) which is displaced over the estimated position of the emitter (1-4). (B) The triangulation of emission (orange) at different beam positions (1-4) allows for the determination of the exact fluorophore position.

Labelling strategies for nanoscopy

The new possibilities brought by the new nanoscopy methods come with new challenges and requirements for biological sample preparation.

Firstly, both stochastic and targeted nanoscopy methods require specific and different fluorophore properties to achieve optimal resolutions. While STED requires bright photostable fluorophores, stochastic methods demand activatable, switching or blinking fluorophores.

Secondly, the labelling of the structure of interest should be as complete as possible. Indeed, at the resolution achieved by MINFLUX each individual molecule can be identified in the sample and for this, it needs to be tagged or labelled.

A third consideration has to me made in regard to the labelling method, meant as the strategy by which a reporter fluorophore is brought in proximity of the target structure with a high specificity. While conventional epi-fluorescent or confocal microscopy mostly rely on indirect immunofluorescence with primary and secondary antibody labelling to detect proteins of interest, this approach shows caveats in nanoscopic methods mostly due to the label size. The primary-secondary antibody complex can reach sizes of over 20 nm, creating a linkage error from fluorophore to target structure that is often larger than the resolution of the nanoscopic method (Maidorn et al. 2016). The large size of the primary antibodies is also a limitation for the complete labelling of the structures of interest, since epitopes might be masked by the presence of the bulky antibody. Lastly, the bivalent nature of antibodies tends to lead to the clustering of molecules (Sograte-Idrissi et al. 2020). Therefore, alternative labelling strategies have been increasingly applied. An overview of such different labels and their sizes is reviewed in Liu et al. 2022. Camelid-derived single domain antibodies (also called nanobodies) or Fab fragments represent a smaller alternative for conventional immunolabeling and provide decoration at much smaller fluorophore displacement without having to manipulate the biological system (Ries et al. 2012; Mikhaylova et al. 2015). This smaller size not only ensures better biological resolution, but also further improves label penetration in crowded protein environments and minimises steric hindrance, enhancing the labelling efficiency of the antigen (Sograte-Idrissi et al. 2020). In comparison to secondary antibodies, fluorescently labelled nanobodies possess a defined number of fluorophores per molecule, leading to a linear antigen-to-fluorophore relation, that can be useful for quantitative analyses of fluorescence intensities in imaging data. Since nanobodies are formed by a single peptide chain, they can be produced by *in vitro* methods, drastically simplifying their production procedure and reducing batch to batch variations (Chen et al. 2021).

While for some targets nanobodies in fusion with a reporter can be expressed in living cells and act as "intrabodies", the majority still requires fixation and membrane permeabilization to decorate the structure of interest, similarly to conventional antibody decoration. An alternative is the use of self-labelling protein tags such as Halo or SNAP tags (Hinner and Johnsson 2010).

These proteins, which are smaller than 40 kDa, are enzyme based, engineered suicide proteins that covalently bind a specific substrate (Hoelzel and Zhang 2020). Thus, they can be introduced into living cells directly, via overexpression, or through gene editing and can be expressed as fusion protein with any protein of interest similarly to fluorescent proteins. Therefore, self-labelling protein tags are, in combination with live cell compatible fluorophores, an optimal method for investigations in living systems.

Possibly the smallest linkage error can be achieved by directly labelling proteins via either small molecules such as phalloidin, jasplakinolide or paclitaxel, or with click chemistry at introduced unnatural amino acids results in (Lukinavičius et al. 2016; Lukinavicius et al. 2014). The first approach does not require the genetic manipulation of the cells as it relies on the use of small drugs targeting the endogenous structure of interest, and which therefore can impact the biological function of the proteins, as discussed below. The latter approach, on the other hand, requires the cellular availability of the machinery necessary to introduce a new tRNA synthetase, limiting its application in neuroscience.

Besides the label size the perturbance of the biological system have to be considered. Protein tags and fusion proteins can have a severe impact on protein function and organisation. This can be due to the expression level for the case of overexpression of modified proteins, since overexpression artefacts can easily occur (Moriya 2015; Uemura et al. 2016; Jensen 2012).

The development of CRISPR/Cas9 technology now offers the possibility of elegantly overcoming the overexpression induced artefacts by knock-in of the tag of interest at genomic level. In such way, the gene is expressed under the endogenous promoter (Knott and Doudna 2018; Lee et al. 2018; Ratz et al. 2015). However also gene edited proteins can be altered in their function and dynamics depending on the influence and position of the tag. A major advantage of protein tags is that they can be used for live cell labelling, given that they are used with a live-cell compatible and cell permeable fluorescent substrate. This allows for investigations in the intact cellular environment with minimal disturbance.

Although live-cell investigations are desirable for many biological applications, live-cell nanoscopy is still highly challenging in multicolour and reaches a relatively low throughput. Therefore, fixated samples are still a promising option for many applications especially when the need for multiplexing and high resolution requires extended measurement times and no reagents for live-labelling are available. Immuno-fluorescent labelling with antibodies or nanobodies and the use of non-permeant or cytotoxic fluorophores is possible in fixated samples, however it is important to consider the possibility of fixation artefacts by the different fixation methods. Therefore, the careful selection of the right fixation protocol should be basis for any labelling strategy (Richter et al. 2018).

Nanoscopy in synaptology

The mammalian brain is a highly complex organ with billions of neurons forming a densely connected network. The smallest information processing unit within this network is the synapse (Sheng and Hoogenraad 2007). Thereby the functioning of this information processing unit relies on its synaptic morphology, composition, and its ability to dynamically adjust to the rapidly changing demands connected to synaptic signalling. Especially the postsynapse can undergo rapid morphological rearrangements in the context of synaptic stimulation (Turrigiano and Nelson 2004; Turrigiano 2008).

For the majority of excitatory synapses, the signal is received at dendritic spines, which are membranous protrusion emerging from the dendritic shaft. These spines, that often consist of a wider head region and a narrower neck, connecting it to the dendrite. Thereby the spine morphology is believed to serve functional aspects and is reflected in synapse plasticity and maturation (Lamprecht 2021; Araya et al. 2014). Through the wide head and narrow neck dendritic spines compartmentalise postsynaptic signal effects by locally limiting calcium fluxes or by providing an electrical resistance to postsynaptic potentials resulting in more confined voltage gradients and favouring the modulation of synaptic transmission (Noguchi et al. 2005; Araya et al. 2006). Thereby a major driver for the shaping of spine morphology and trafficking of components is the synaptic cytoskeleton (Goellner and Aberle 2012).

Spines harbour a vast variety of functional proteins required for signal transduction, many of which can be found in the postsynaptic density (PSD), a characteristic feature, that was first discovered as a dense protein region in electron microscopy (PALAY 1956). This dense protein network can consist more than thousand different proteins within a volume of only less than half a micron in diameter (Bayés et al. 2011; Carlin et al. 1980; Helm et al. 2021). As many other small synaptic structures, it therefore requires imaging methods that can resolve features close or below the diffraction limit. Hence, optical nanoscopy methods such as STED, STORM or MINFLUX have increasingly been facilitating studies on synapse structure and organization. Nanoscopic studies have since then led to the several advances in synaptology as for example the analysis of the structural composition of the presynapse (Wilhelm et al. 2014; Testa et al. 2015; Urban et al. 2011). Moreover it has shed light onto receptor distribution and trafficking at the postsynapse, and the organisation in so-called nanodomains (Frank and Grant 2017; Choquet 2010; Upmanyu et al. 2022).

The PSD is known to be involved in the organisation and positioning of neurotransmitter receptors such as for AMPA or NMDA, cytoskeletal components and other scaffolding proteins (Buonarati et al. 2019; Frank and Grant 2017; Nair et al. 2013). One of the most abundant proteins within this complex is PSD-95 and its highly dynamic behaviour has previously been elucidated by *in vivo* STED microscopy (Masch et al. 2018; Wegner et al. 2018; Wegner et al. 2022; Choquet and Triller 2013; Sun et al. 2021).

The synaptic cytoskeleton plays a key role in synapse formation and plasticity as well as the dynamics of synaptic organelles. So far, only little is known about the distribution and plasticity of individual cytoskeletal components at synaptic sites (Glebov et al. 2017; Borovac et al. 2018). The postsynaptic cytoskeleton has been prominent subject of investigating morphological changes at the post synapse (Cingolani and Goda 2008; Dillon and Goda 2005; Korobova and Svitkina 2010; Bonilla-Quintana et al. 2021; Urban et al. 2011; Hu et al. 2008). Understanding of the role of other cytoskeletal elements such as microtubules and neurofilaments in the regulation of synaptic activity and synapse morphology is however still limited (Jaworski et al. 2009; Roots 1983; Yuan et al. 2015; Hu et al. 2008).

Considering the dynamic nature of synaptic structures, there is a constant demand of synaptic components to meet the needs of individual synaptic sites (Grochowska et al. 2022). At the same time long-lived neuronal signalling patterns that determine our cognition and memory formation, far exceeding the lifetime of individual proteins need to be established and maintained (Crick 1984; Fornasiero et al. 2018; Bulovaite et al. 2021). Thus, a tightly balanced and finely regulated synthesis and delivery of required proteins that determines the rate of protein turnover of synaptic proteins is consequently essential to synaptic function (Alvarez-Castelao and Schuman 2015). Therefore, also sub-cellular organelles such as components of the secretory pathway, or the spine apparatus play an important role in synapse function and plasticity.

Increasing evidence of local protein synthesis directly at ore in close proximity to synaptic sites further shape our view of the synapse as independent functional unit (Biever et al. 2019; Biever et al. 2020; Perez-Alvarez et al. 2020; Perez and Schuman 2022; Hanus and Ehlers 2008; Hanus et al. 2016).

Although the spine itself was already visualised in the 19th century, due to their sub-micron to nanometre size, the majority of the above-mentioned synaptic elements could not be resolved within the context of spines before the advent of nanoscopy methods. Therefore, nanoscopic approaches play a vital role for studying the synaptic organisation (Dankovich and Rizzoli 2021).

References

Abbe, E. (1873): Beiträge zur Theorie des Mikroskops und der mikroskopischen Wahrnehmung. In *Archiv f. mikrosk. Anatomie* 9 (1), pp. 413–468. DOI: 10.1007/BF02956173.

Airy, G. B. (1835): On the Diffraction of an Object-glass with Circular Aperture. In *Transactions of the Cambridge Philosophical Society* 5, p. 283.

Alvarez-Castelao, Beatriz; Schuman, Erin M. (2015): The Regulation of Synaptic Protein Turnover. In *The Journal of biological chemistry* 290 (48), pp. 28623–28630. DOI: 10.1074/jbc.R115.657130.

Araya, Roberto; Jiang, Jiang; Eisenthal, Kenneth B.; Yuste, Rafael (2006): The spine neck filters membrane potentials. In *Proceedings of the National Academy of Sciences of the United States of America* 103 (47), pp. 17961–17966. DOI: 10.1073/pnas.0608755103.

Araya, Roberto; Vogels, Tim P.; Yuste, Rafael (2014): Activity-dependent dendritic spine neck changes are correlated with synaptic strength. In *Proceedings of the National Academy of Sciences of the United States of America* 111 (28), E2895-904. DOI: 10.1073/pnas.1321869111.

Arroyo-Camejo, Silvia; Adam, Marie-Pierre; Besbes, Mondher; Hugonin, Jean-Paul; Jacques, Vincent; Greffet, Jean-Jacques et al. (2013): Stimulated emission depletion microscopy resolves individual nitrogen vacancy centers in diamond nanocrystals. In *ACS nano* 7 (12), pp. 10912–10919. DOI: 10.1021/nn404421b.

Balzarotti, Francisco; Eilers, Yvan; Gwosch, Klaus C.; Gynnå, Arvid H.; Westphal, Volker; Stefani, Fernando D. et al. (2017): Nanometer resolution imaging and tracking of fluorescent molecules with minimal photon fluxes. In *Science (New York, N.Y.)* 355 (6325), pp. 606–612. DOI: 10.1126/science.aak9913.

Bayés, Alex; van de Lagemaat, Louie N.; Collins, Mark O.; Croning, Mike D. R.; Whittle, Ian R.; Choudhary, Jyoti S.; Grant, Seth G. N. (2011): Characterization of the proteome, diseases and evolution of the human postsynaptic density. In *Nature neuroscience* 14 (1), pp. 19–21. DOI: 10.1038/nn.2719.

Betzig, Eric; Patterson, George H.; Sougrat, Rachid; Lindwasser, O. Wolf; Olenych, Scott; Bonifacino, Juan S. et al. (2006): Imaging intracellular fluorescent proteins at nanometer resolution. In *Science (New York, N.Y.)* 313 (5793), pp. 1642–1645. DOI: 10.1126/science.1127344.

Biever, Anne; Donlin-Asp, Paul G.; Schuman, Erin M. (2019): Local translation in neuronal processes. In *Current opinion in neurobiology* 57, pp. 141–148. DOI: 10.1016/j.conb.2019.02.008.

Biever, Anne; Glock, Caspar; Tushev, Georgi; Ciirdaeva, Elena; Dalmay, Tamas; Langer, Julian D.; Schuman, Erin M. (2020): Monosomes actively translate synaptic mRNAs in neuronal processes. In *Science (New York, N.Y.)* 367 (6477). DOI: 10.1126/science.aay4991.

Bonilla-Quintana, Mayte; Wörgötter, Florentin; D'Este, Elisa; Tetzlaff, Christian; Fauth, Michael (2021): Reproducing asymmetrical spine shape fluctuations in a model of actin dynamics predicts self-organized criticality. In *Scientific reports* 11 (1), p. 4012. DOI: 10.1038/s41598-021-83331-9.

Borovac, Jelena; Bosch, Miquel; Okamoto, Kenichi (2018): Regulation of actin dynamics during structural plasticity of dendritic spines: Signaling messengers and actin-binding proteins. In *Molecular and cellular neurosciences* 91, pp. 122–130. DOI: 10.1016/j.mcn.2018.07.001.

Bulovaite, Edita; Qiu, Zhen; Kratschke, Maximilian; Zgraj, Adrianna; Fricker, David G.; Tuck, Eleanor J. et al. (2021): A brain atlas of synapse protein lifetime across the mouse lifespan.

Buonarati, Olivia R.; Hammes, Erik A.; Watson, Jake F.; Greger, Ingo H.; Hell, Johannes W. (2019): Mechanisms of postsynaptic localization of AMPA-type glutamate receptors and their regulation during long-term potentiation. In *Science signaling* 12 (562). DOI: 10.1126/scisignal.aar6889.

Carlin, R. K.; Grab, D. J.; Cohen, R. S.; Siekevitz, P. (1980): Isolation and characterization of postsynaptic densities from various brain regions: enrichment of different types of postsynaptic densities. In *The Journal of cell biology* 86 (3), pp. 831–845. DOI: 10.1083/jcb.86.3.831.

Chen, Xun; Gentili, Matteo; Hacohen, Nir; Regev, Aviv (2021): A cell-free nanobody engineering platform rapidly generates SARS-CoV-2 neutralizing nanobodies. In *Nature communications* 12 (1), p. 5506. DOI: 10.1038/s41467-021-25777-z.

Choquet, Daniel (2010): Fast AMPAR trafficking for a high-frequency synaptic transmission. In *The European journal of neuroscience* 32 (2), pp. 250–260. DOI: 10.1111/j.1460-9568.2010.07350.x.

Choquet, Daniel; Triller, Antoine (2013): The dynamic synapse. In *Neuron* 80 (3), pp. 691–703. DOI: 10.1016/j.neuron.2013.10.013.

Cingolani, Lorenzo A.; Goda, Yukiko (2008): Actin in action: the interplay between the actin cytoskeleton and synaptic efficacy. In *Nature reviews. Neuroscience* 9 (5), pp. 344–356. DOI: 10.1038/nrn2373.

Crick, F. (1984): Memory and molecular turnover. In *Nature* 312 (5990), p. 101. DOI: 10.1038/312101a0.

Cybulski, James S.; Clements, James; Prakash, Manu (2014): Foldscope: origami-based paper microscope. In *PloS one* 9 (6), e98781. DOI: 10.1371/journal.pone.0098781.

Dankovich, Tal M.; Rizzoli, Silvio O. (2021): Challenges facing quantitative large-scale optical super-resolution, and some simple solutions. In *iScience* 24 (3), p. 102134. DOI: 10.1016/j.isci.2021.102134.

D'Este, Elisa; Kamin, Dirk; Göttfert, Fabian; El-Hady, Ahmed; Hell, Stefan W. (2015): STED nanoscopy reveals the ubiquity of subcortical cytoskeleton periodicity in living neurons. In *Cell reports* 10 (8), pp. 1246–1251. DOI: 10.1016/j.celrep.2015.02.007.

Dillon, Christian; Goda, Yukiko (2005): The actin cytoskeleton: integrating form and function at the synapse. In *Annual review of neuroscience* 28, pp. 25–55. DOI: 10.1146/annurev.neuro.28.061604.135757.

Fölling, Jonas; Bossi, Mariano; Bock, Hannes; Medda, Rebecca; Wurm, Christian A.; Hein, Birka et al. (2008): Fluorescence nanoscopy by ground-state depletion and single-molecule return. In *Nat Methods* 5 (11), pp. 943–945. DOI: 10.1038/nmeth.1257.

Fornasiero, Eugenio F.; Mandad, Sunit; Wildhagen, Hanna; Alevra, Mihai; Rammner, Burkhard; Keihani, Sarva et al. (2018): Precisely measured protein lifetimes in the mouse brain reveal differences across tissues and subcellular fractions. In *Nature communications* 9 (1), p. 4230. DOI: 10.1038/s41467-018-06519-0.

Frank, René Aw; Grant, Seth Gn (2017): Supramolecular organization of NMDA receptors and the postsynaptic density. In *Current opinion in neurobiology* 45, pp. 139–147. DOI: 10.1016/j.conb.2017.05.019.

Gest, Howard (2009): Homage to Robert Hooke (1635-1703): new insights from the recently discovered Hooke Folio. In *Perspectives in biology and medicine* 52 (3), pp. 392–399. DOI: 10.1353/pbm.0.0096.

Glebov, Oleg O.; Jackson, Rachel E.; Winterflood, Christian M.; Owen, Dylan M.; Barker, Ellen A.; Doherty, Patrick et al. (2017): Nanoscale Structural Plasticity of the Active Zone Matrix Modulates Presynaptic Function. In *Cell reports* 18 (11), pp. 2715–2728. DOI: 10.1016/j.celrep.2017.02.064.

Goellner, Bernd; Aberle, Hermann (2012): The synaptic cytoskeleton in development and disease. In *Developmental neurobiology* 72 (1), pp. 111–125. DOI: 10.1002/dneu.20892.

Gray, J. A. (2001): The evolution of screening. In *Pharmacoepidemiology and drug safety* 10 (1), pp. 49–54. DOI: 10.1002/pds.583.

Grochowska, Katarzyna M.; Andres-Alonso, Maria; Karpova, Anna; Kreutz, Michael R. (2022): The needs of a synapse-How local organelles serve synaptic proteostasis. In *The EMBO journal* 41 (7), e110057. DOI: 10.15252/embj.2021110057.

Große, Lena; Wurm, Christian A.; Brüser, Christian; Neumann, Daniel; Jans, Daniel C.; Jakobs, Stefan (2016): Bax assembles into large ring-like structures remodeling the mitochondrial outer membrane in apoptosis. In *The EMBO journal* 35 (4), pp. 402–413. DOI: 10.15252/embj.201592789.

Hanus, Cyril; Ehlers, Michael D. (2008): Secretory outposts for the local processing of membrane cargo in neuronal dendrites. In *Traffic (Copenhagen, Denmark)* 9 (9), pp. 1437–1445. DOI: 10.1111/j.1600-0854.2008.00775.x.

Hanus, Cyril; Geptin, Helene; Tushev, Georgi; Garg, Sakshi; Alvarez-Castelao, Beatriz; Sambandan, Sivakumar et al. (2016): Unconventional secretory processing diversifies neuronal ion channel properties. In *eLife* 5. DOI: 10.7554/eLife.20609.

Heilemann, Mike; van de Linde, Sebastian; Schüttpelz, Mark; Kasper, Robert; Seefeldt, Britta; Mukherjee, Anindita et al. (2008): Subdiffraction-resolution fluorescence imaging with conventional fluorescent probes. In *Angewandte Chemie International Edition* 47 (33), pp. 6172–6176. DOI: 10.1002/anie.200802376.

Hell, S. W. (2007): Far-field optical nanoscopy. In *Science* 316 (5828), pp. 1153–1158. DOI: 10.1126/science.1137395.

Hell, S. W.; Wichmann, J. (1994): Breaking the diffraction resolution limit by stimulated emission: stimulated-emission-depletion fluorescence microscopy. In *Optics letters* 19 (11), pp. 780–782. DOI: 10.1364/ol.19.000780.

Hell, Stefan W. (2015): Nanoscopy with Focused Light (Nobel Lecture). In *Angewandte Chemie International Edition* 54 (28), pp. 8054–8066. DOI: 10.1002/anie.201504181.

Helm, Martin S.; Dankovich, Tal M.; Mandad, Sunit; Rammner, Burkhard; Jähne, Sebastian; Salimi, Vanessa et al. (2021): A large-scale nanoscopy and biochemistry analysis of postsynaptic dendritic spines. In *Nature neuroscience* 24 (8), pp. 1151–1162. DOI: 10.1038/s41593-021-00874-w.

Helmholtz, H. von (1874): Die theoretische Grenze für die Leistungsfähigkeit der Mikroskope. Available online at https://books.google.de/books?id=cpF9nQAACAAJ.

Hess, Samuel T.; Girirajan, Thanu P. K.; Mason, Michael D. (2006): Ultra-high resolution imaging by fluorescence photoactivation localization microscopy. In *Biophysical journal* 91 (11), pp. 4258–4272. DOI: 10.1529/biophysj.106.091116.

Hinner, Marlon J.; Johnsson, Kai (2010): How to obtain labeled proteins and what to do with them. In *Current opinion in biotechnology* 21 (6), pp. 766–776. DOI: 10.1016/j.copbio.2010.09.011.

Hoelzel, Conner A.; Zhang, Xin (2020): Visualizing and Manipulating Biological Processes by Using HaloTag and SNAP-Tag Technologies. In *Chembiochem : a European journal of chemical biology* 21 (14), pp. 1935–1946. DOI: 10.1002/cbic.202000037.

Hu, Xindao; Viesselmann, Chris; Nam, Sookin; Merriam, Elliott; Dent, Erik W. (2008): Activity-dependent dynamic microtubule invasion of dendritic spines. In *The Journal of neuroscience : the official journal of the Society for Neuroscience* 28 (49), pp. 13094–13105. DOI: 10.1523/JNEUROSCI.3074-08.2008.

Jaworski, Jacek; Kapitein, Lukas C.; Gouveia, Susana Montenegro; Dortland, Bjorn R.; Wulf, Phebe S.; Grigoriev, Ilya et al. (2009): Dynamic microtubules regulate dendritic spine morphology and synaptic plasticity. In *Neuron* 61 (1), pp. 85–100. DOI: 10.1016/j.neuron.2008.11.013.

Jensen, Ellen C. (2012): Use of fluorescent probes: their effect on cell biology and limitations. In *Anatomical record (Hoboken, N.J. : 2007)* 295 (12), pp. 2031–2036. DOI: 10.1002/ar.22602.

Knott, Gavin J.; Doudna, Jennifer A. (2018): CRISPR-Cas guides the future of genetic engineering. In *Science (New York, N.Y.)* 361 (6405), pp. 866–869. DOI: 10.1126/science.aat5011.

Korobova, Farida; Svitkina, Tatyana (2010): Molecular architecture of synaptic actin cytoskeleton in hippocampal neurons reveals a mechanism of dendritic spine morphogenesis. In *Mol Biol Cell* 21 (1), pp. 165–176. DOI: 10.1091/mbc.e09-07-0596.

Lamprecht, Raphael (2021): Actin Cytoskeleton Role in the Maintenance of Neuronal Morphology and Long-Term Memory. In *Cells* 10 (7). DOI: 10.3390/cells10071795.

Lee, Seung Hwan; Kim, Sunghyun; Hur, Junho K. (2018): CRISPR and Target-Specific DNA Endonucleases for Efficient DNA Knock-in in Eukaryotic Genomes. In *Molecules and cells* 41 (11), pp. 943–952. DOI: 10.14348/molcells.2018.0408.

Liu, Sheng; Hoess, Philipp; Ries, Jonas (2022): Super-Resolution Microscopy for Structural Cell Biology. In *Annual review of biophysics* 51, pp. 301–326. DOI: 10.1146/annurev-biophys-102521-112912.

Lukinavicius, G.; Reymond, L.; D'Este, E.; Masharina, A.; Gottfert, F.; Ta, H. et al. (2014): Fluorogenic probes for live-cell imaging of the cytoskeleton. In *Nat Methods* 11 (7), pp. 731–733. DOI: 10.1038/nmeth.2972.

Lukinavičius, Gražvydas; Reymond, Luc; Umezawa, Keitaro; Sallin, Olivier; D'Este, Elisa; Göttfert, Fabian et al. (2016): Fluorogenic Probes for Multicolor Imaging in Living Cells. In *Journal of the American Chemical Society* 138 (30), pp. 9365–9368. DOI: 10.1021/jacs.6b04782.

Maidorn, Manuel; Rizzoli, Silvio O.; Opazo, Felipe (2016): Tools and limitations to study the molecular composition of synapses by fluorescence microscopy. In *The Biochemical journal* 473 (20), pp. 3385–3399. DOI: 10.1042/BCJ20160366.

Masch, Jennifer-Magdalena; Steffens, Heinz; Fischer, Joachim; Engelhardt, Johann; Hubrich, Jasmine; Keller-Findeisen, Jan et al. (2018): Robust nanoscopy of a synaptic protein in living mice by organic-fluorophore labeling. In *Proceedings of the National Academy of Sciences of the United States of America*. DOI: 10.1073/pnas.1807104115.

Masters, Barry R. (2007): Ernst Abbe and the Foundation of Scientific Microscopes. In *Optics & Photonics News, OPN* 18 (2), p. 18. DOI: 10.1364/OPN.18.2.000018.

Mikhaylova, Marina; Cloin, Bas M. C.; Finan, Kieran; van den Berg, Robert; Teeuw, Jalmar; Kijanka, Marta M. et al. (2015): Resolving bundled microtubules using anti-tubulin nanobodies. In *Nature communications* 6, p. 7933. DOI: 10.1038/ncomms8933.

Moriya, Hisao (2015): Quantitative nature of overexpression experiments. In *Molecular biology of the cell* 26 (22), pp. 3932–3939. DOI: 10.1091/mbc.E15-07-0512.

Nair, Deepak; Hosy, Eric; Petersen, Jennifer D.; Constals, Audrey; Giannone, Gregory; Choquet, Daniel; Sibarita, Jean-Baptiste (2013): Super-resolution imaging reveals that AMPA receptors inside synapses are dynamically organized in nanodomains regulated by PSD95. In *The Journal of neuroscience : the official journal of the Society for Neuroscience* 33 (32), pp. 13204–13224. DOI: 10.1523/JNEUROSCI.2381-12.2013.

Noguchi, Jun; Matsuzaki, Masanori; Ellis-Davies, Graham C. R.; Kasai, Haruo (2005): Spine-neck geometry determines NMDA receptor-dependent Ca2+ signaling in dendrites. In *Neuron* 46 (4), pp. 609–622. DOI: 10.1016/j.neuron.2005.03.015.

Owald, David; Fouquet, Wernher; Schmidt, Manuela; Wichmann, Carolin; Mertel, Sara; Depner, Harald et al. (2010): A Syd-1 homologue regulates pre- and postsynaptic maturation in Drosophila. In *The Journal of cell biology* 188 (4), pp. 565–579. DOI: 10.1083/jcb.200908055.

PALAY, S. L. (1956): Synapses in the central nervous system. In *The Journal of biophysical and biochemical cytology* 2 (4 Suppl), pp. 193–202. DOI: 10.1083/jcb.2.4.193.

Pawley, James (Ed.) (2010): Handbook of Biological Confocal Microscopy. 3rd ed. New York, NY: Springer (SpringerLink Bücher).

Perez, Julio D.; Schuman, Erin M. (2022): Subcellular RNA-seq for the Analysis of the Dendritic and Somatic Transcriptomes of Single Neurons. In *Bio-protocol* 12 (1), e4278. DOI: 10.21769/BioProtoc.4278.

Perez-Alvarez, Alberto; Yin, Shuting; Schulze, Christian; Hammer, John A.; Wagner, Wolfgang; Oertner, Thomas G. (2020): Endoplasmic reticulum visits highly active spines and prevents runaway potentiation of synapses. In *Nature communications* 11 (1), p. 5083. DOI: 10.1038/s41467-020-18889-5.

Ratz, Michael; Testa, Ilaria; Hell, Stefan W.; Jakobs, Stefan (2015): CRISPR/Cas9-mediated endogenous protein tagging for RESOLFT super-resolution microscopy of living human cells. In *Sci Rep* 5, p. 9592. DOI: 10.1038/srep09592.

Richter, Katharina N.; Revelo, Natalia H.; Seitz, Katharina J.; Helm, Martin S.; Sarkar, Deblina; Saleeb, Rebecca S. et al. (2018): Glyoxal as an alternative fixative to formaldehyde in immunostaining and super-resolution microscopy. In *The EMBO journal* 37 (1), pp. 139–159. DOI: 10.15252/embj.201695709.

Ries, Jonas; Kaplan, Charlotte; Platonova, Evgenia; Eghlidi, Hadi; Ewers, Helge (2012): A simple, versatile method for GFP-based super-resolution microscopy via nanobodies. In *Nature methods* 9 (6), pp. 582–584. DOI: 10.1038/nmeth.1991.

Roots, B. I. (1983): Neurofilament accumulation induced in synapses by leupeptin. In *Science (New York, N.Y.)* 221 (4614), pp. 971–972. DOI: 10.1126/science.6192501.

Rust, Michael J.; Bates, Mark; Zhuang, Xiaowei (2006): Sub-diffraction-limit imaging by stochastic optical reconstruction microscopy (STORM). In *Nat Methods* 3 (10), pp. 793–795. DOI: 10.1038/nmeth929.

Sahl, Steffen J.; Hell, Stefan W.; Jakobs, Stefan (2017): Fluorescence nanoscopy in cell biology. In *Nature reviews. Molecular cell biology* 18 (11), pp. 685–701. DOI: 10.1038/nrm.2017.71.

Saka, Sinem K. (2014): Light Microscopy and Resolution. In Eugenio F. Fornasiero, Silvio O. Rizzoli (Eds.): Super-Resolution Microscopy Techniques in the Neurosciences, vol. 86. Totowa, NJ: Humana Press (86), pp. 1–11.

Sheng, Morgan; Hoogenraad, Casper C. (2007): The postsynaptic architecture of excitatory synapses: a more quantitative view. In *Annual review of biochemistry* 76, pp. 823–847. DOI: 10.1146/annurev.biochem.76.060805.160029.

Sigal, Yaron M.; Zhou, Ruobo; Zhuang, Xiaowei (2018): Visualizing and discovering cellular structures with super-resolution microscopy. In *Science (New York, N.Y.)* 361 (6405), pp. 880–887. DOI: 10.1126/science.aau1044.

Sograte-Idrissi, Shama; Schlichthaerle, Thomas; Duque-Afonso, Carlos J.; Alevra, Mihai; Strauss, Sebastian; Moser, Tobias et al. (2020): Circumvention of common labelling artefacts using secondary nanobodies. In *Nanoscale*. DOI: 10.1039/d0nr00227e.

Stokes, G. (1852): On the change of refrangibility of light. In *Phil. Trans. R. Soc.* 142, pp. 463–562. DOI: 10.1098/rstl.1852.0022.

Sun, Ye; Smirnov, Michael; Kamasawa, Naomi; Yasuda, Ryohei (2021): Rapid Ultrastructural Changes in the PSD and Surrounding Membrane after Induction of Structural LTP in Single Dendritic Spines. In *The Journal of neuroscience : the official journal of the Society for Neuroscience* 41 (33), pp. 7003–7014. DOI: 10.1523/JNEUROSCI.1964-20.2021.

Szymborska, Anna; Marco, Alex de; Daigle, Nathalie; Cordes, Volker C.; Briggs, John A. G.; Ellenberg, Jan (2013): Nuclear pore scaffold structure analyzed by super-resolution microscopy and particle averaging. In *Science (New York, N.Y.)* 341 (6146), pp. 655–658. DOI: 10.1126/science.1240672.

Testa, I.; D'Este, E.; Urban, N. T.; Balzarotti, F.; Hell, S. W. (2015): Dual channel RESOLFT nanoscopy by using fluorescent state kinetics. In *Nano Lett* 15 (1), pp. 103–106. DOI: 10.1021/nl503058k.

Turrigiano, Gina G. (2008): The self-tuning neuron: synaptic scaling of excitatory synapses. In *Cell* 135 (3), pp. 422–435. DOI: 10.1016/j.cell.2008.10.008.

Turrigiano, Gina G.; Nelson, Sacha B. (2004): Homeostatic plasticity in the developing nervous system. In *Nature reviews. Neuroscience* 5 (2), pp. 97–107. DOI: 10.1038/nrn1327.

Uemura, Takeshi; Mori, Takuma; Kurihara, Taiga; Kawase, Shiori; Koike, Rie; Satoga, Michiru et al. (2016): Fluorescent protein tagging of endogenous protein in brain neurons using CRISPR/Cas9-mediated knock-in and in utero electroporation techniques. In *Sci Rep* 6, p. 35861. DOI: 10.1038/srep35861.

Upmanyu, Neha; Jin, Jialin; Emde, Henrik von der; Ganzella, Marcelo; Bösche, Leon; Malviya, Viveka Nand et al. (2022): Colocalization of different neurotransmitter transporters on synaptic vesicles is sparse except for VGLUT1 and ZnT3. In *Neuron* 110 (9), 1483-1497.e7. DOI: 10.1016/j.neuron.2022.02.008.

Urban, Nicolai T.; Willig, Katrin I.; Hell, Stefan W.; Nägerl, U. Valentin (2011): STED nanoscopy of actin dynamics in synapses deep inside living brain slices. In *Biophysical journal* 101 (5), pp. 1277–1284. DOI: 10.1016/j.bpj.2011.07.027.

Wegner, Waja; Mott, Alexander C.; Grant, Seth G. N.; Steffens, Heinz; Willig, Katrin I. (2018): In vivo STED microscopy visualizes PSD95 sub-structures and morphological changes over several hours in the mouse visual cortex. In *Sci Rep* 8 (1), p. 219. DOI: 10.1038/s41598-017-18640-z.

Wegner, Waja; Steffens, Heinz; Gregor, Carola; Wolf, Fred; Willig, Katrin I. (2022): Environmental enrichment enhances patterning and remodeling of synaptic nanoarchitecture as revealed by STED nanoscopy. In *eLife* 11. DOI: 10.7554/eLife.73603.

Wilhelm, Benjamin G.; Mandad, Sunit; Truckenbrodt, Sven; Kröhnert, Katharina; Schäfer, Christina; Rammner, Burkhard et al. (2014): Composition of isolated synaptic boutons reveals the amounts of vesicle trafficking proteins. In *Science (New York, N.Y.)* 344 (6187), pp. 1023–1028. DOI: 10.1126/science.1252884.

Wimmer, Wolfgang (2017): Carl Zeiss, Ernst Abbe, and Advances in the Light Microscope. In *Micros. Today* 25 (4), pp. 50–57. DOI: 10.1017/S155192951700058X.

Wollman, Adam J. M.; Nudd, Richard; Hedlund, Erik G.; Leake, Mark C. (2015): From Animaculum to single molecules: 300 years of the light microscope. In *Open biology* 5 (4), p. 150019. DOI: 10.1098/rsob.150019.

Xu, Ke; Zhong, Guisheng; Zhuang, Xiaowei (2013): Actin, spectrin, and associated proteins form a periodic cytoskeletal structure in axons. In *Science (New York, N.Y.)* 339 (6118), pp. 452–456. DOI: 10.1126/science.1232251.

Yuan, A.; Sershen, H.; Veeranna; Basavarajappa, B. S.; Kumar, A.; Hashim, A. et al. (2015): Functions of neurofilaments in synapses. In *Mol Psychiatry* 20 (8), p. 915. DOI: 10.1038/mp.2015.99.

Yuste, Rafael (2015): The discovery of dendritic spines by Cajal. In *Frontiers in neuroanatomy* 9, p. 18. DOI: 10.3389/fnana.2015.00018.

Motivation and aim of this thesis

Nanoscopy methods have paved the way to the investigation of proteins at so far unseen resolution and thereby enabled new discoveries in synaptology. However, qualitative measures of synaptic structures are not enough to understand processes at this vastly heterogenous and finely regulated compartment. This dissertation aims at the development of integrated nanoscopy approaches for the quantitative study of synaptic components in a functional context and at the single synapse level.

More specifically, this thesis aims at

(i) implementing strategies to quantify the abundance and distribution of synaptic targets of interests within the context of the synaptic activity. This is achieved by multicolour nanoscopy of protein of interest along with markers of the synaptic status and by implementing related image analysis routines. The strategy is used to study the presence of components of the secretory pathway and neurofilaments at the postsynapse with respect to pre- and postsynaptic strength and presynaptic activity (chapter 2 and 3, respectively);

(ii) visualizing protein turnover at the single synapse level within the context of synaptic plasticity, thereby adding time information to the images. By using pulse-chase experiments and gene editing tools, I aim at revealing how activity influences the incorporation of new proteins in the postsynaptic density. This aim is pursued in chapter 4, where I describe the new postsynaptic density 95 (PSD-95) protein synthesis at the single synapse level;

(iii) characterizing the structural rearrangements occurring at synaptic sites during plasticity with three-dimensional molecular resolution. By using MINFLUX nanoscopy, I aim at understanding how activity impacts the organization of postsynaptic sites, and in particular of PSD-95 (chapter 4).

All in all, this thesis aims to broaden scope of nanoscopy applications in neuroscience by adding new levels of information to imaging, ultimately supporting our understanding of the mechanisms underlying synaptic plasticity.

Chapter 2 – Synaptic Secretory Elements

The constant supply of synaptic sites with new secreted or transmembrane proteins is essential for the function of synapses. The following study focused on the quantification of several secretory pathway elements at synaptic sites. By means of multi-colour STED nanoscopy and optimised image processing pipelines this study analysed how single synapses recruit their own local protein synthesis and maturation machinery to support local protein turnover. The data show how synaptic activity and synaptic strength influence the composition of the synaptic environment.

Within this study I performed all experiments and acquired all image data. Furthermore, I executed manual or semi-automates image segmentation and supported the data analysis. I prepared all figures and wrote the manuscript with contributions of the other authors.

This manuscript was published in the journal Scientific Reports:

- Gürth, CM., Dankovich, T.M., Rizzoli, S.O. et al. **Synaptic activity and strength are reflected by changes in the post-synaptic secretory pathway**. Sci Rep 10, 20576 (2020). https://doi.org/10.1038/s41598-020-77260-2
- Shared first authorship
- Received: 25 May 2020
- Accepted: 09 November 2020
- Published: 25 November 2020
- Reproduced with permission from Springer Nature

Synaptic activity and strength are reflected by changes in the post-synaptic secretory pathway

Clara-Marie Gürth [1, 2, #], Tal M. Dankovich [3, #], Silvio O. Rizzoli [3], Elisa D'Este [4, *]

[1] Department of NanoBiophotonics, Max Planck Institute for Biophysical Chemistry, Am Fassberg 11, 37077 Göttingen, Germany

[2] Department of Optical Nanoscopy, Max Planck Institute for Medical Research, Jahnstr. 29, 69120 Heidelberg, Germany

[3] Institute for Neuro- and Sensory Physiology, University Medical Center Göttingen, Humboldtallee 23, 37073 Göttingen, Germany

[4] Optical Microscopy Facility, Max Planck Institute for Medical Research, Jahnstr. 29, 69120 Heidelberg, Germany

[#] Contributed equally to this work

[*] Corresponding author: elisa.deste@mr.mpg.de

Abstract

Neurons are highly asymmetric cells that span long distances and need to react promptly to local demands. Consequently, neuronal secretory pathway elements are distributed throughout neurites, specifically in post-synaptic compartments, to enable local protein synthesis and delivery. Whether and how changes in local synaptic activity correlate to post-synaptic secretory elements is still unclear. To assess this, we used STED nanoscopy and automated quantitative image analysis of post-synaptic markers of the endoplasmic reticulum, ER-Golgi intermediate compartment, trans-Golgi network, and spine apparatus. We found that the distribution of these proteins was dependent on pre-synaptic activity, measured as the amount of recycling vesicles. Moreover, their abundance correlated to both pre- and post-synaptic markers of synaptic strength. Overall, the results suggest that in small, low-activity synapses the secretory pathway components are tightly clustered in the synaptic area, presumably to enable rapid local responses, while bigger synapses utilise secretory machinery components from larger, more diffuse areas.

Introduction

The secretory pathway elements support cellular functions by ensuring local delivery and post-translational modifications of secreted and transmembrane proteins. These proteins are translated directly into the endoplasmic reticulum (ER) lumen, and transported to the Golgi apparatus via the ER-Golgi intermediate compartment (ERGIC) (Aebi et al. 2010; Gardiol et al. 1999). Then, cargoes exit the Golgi apparatus via the trans-Golgi network (TGN), where the proteins are sorted and transported to their respective sites of action (Griffiths and Simons 1986). Due to their highly asymmetrical shape, size and subcellular specialisation, neurons need to organise protein synthesis along their entire volume (for reviews Glock et al. 2017; Rangaraju et al. 2017; Terenzio et al. 2017; Biever et al. 2020; Holt et al. 2019). Protein processing through a secretory pathway organised exclusively in the soma would not allow a prompt supply of newly synthesised proteins to distal regions, and would not meet the specific needs of each subcellular compartment (Williams et al. 2016). To compensate for this limitation, the protein synthesis machinery (mRNAs and ribosomes) has been reported in both pre- and post-synaptic areas (Hafner et al. 2019), and other secretory pathway elements are also widespread or asymmetrically distributed, to ensure an adequate protein supply at specific subcellular locations (Kennedy and Hanus 2019).

The neuronal ER forms a branched network, stretching from the soma to dendrites and axonal pre-synaptic terminals, albeit it is far more abundant in dendrites than in axons (Kennedy and Hanus 2019; Ramírez and Couve 2011). Although it spans over long distances, the ER still remains one single membrane organelle, with a continuous lumen (Spacek and Harris 1997). The ER has been found within dendritic spines, where it shows high turnover, contributes to long-term potentiation (LTP), and a specialised, smooth ER variant forms the spine apparatus (SA) (Toresson and Grant 2005; Chirillo et al. 2019). The SA has been documented in a subset of spines and is involved in calcium storage, synaptic strength, and robust potentiation (Vlachos et al. 2009; Jedlicka and Deller 2017; Deller et al. 2007; Segal et al. 2010; Vlachos 2012). The SA is bound to the actin cytoskeleton of the spine by the marker and essential component synaptopodin (Mundel et al. 1997; Deller et al. 2000a; Deller et al. 2003). This protein is required for calcium regulation and actin remodelling (Deller et al. 2007; Segal et al. 2010; Vlachos 2012; Deller et al. 2000b). However, synaptopodin has also been shown to be a potential marker of SA-unrelated dynamics (Chirillo et al. 2019; Bas Orth et al. 2005).

Similar to the ER, the neuronal ERGIC is also found in the cell body and dendritic shafts, but is rarely present in spines (Kennedy and Hanus 2019; Bowen et al. 2017; Wu et al. 2017; Saraste and Marie 2018). Within the spine, ERGIC is often located in close proximity to recycling endosomes, which are similar in shape. Thus, discriminating between them unambiguously by electron microscopy is difficult (Bowen et al. 2017; Wu et al. 2017). Trafficking of ERGIC vesicles along dendrites is restricted by increased neuronal activity, indicating that this post-ER compartment can be subjected to synaptic activity-dependent regulation (Hanus et al. 2014).

Unlike the other organelles of the secretory pathway, the neuronal Golgi apparatus localises mainly around the nucleus and along the first portion of the apical or longer dendrite (Lowenstein et al. 1994; Horton et al. 2005). However, smaller Golgi outposts can be found in a subset of dendrites and small Golgi satellite structures have been observed throughout the entire dendritic tree, often in close association to the ERGIC (Horton et al. 2005; Mikhaylova et al. 2016). In addition, a marker of the trans-Golgi network, TGN38, has been observed along the whole dendritic tree, including small dendrites and spines (Gardiol et al. 1999; McNamara et al. 2004; Chen et al. 2012; Cox and Racca 2013). TGN38, whose synthesis can be modulated by neuronal activity, is present in vesicles that cycle between the plasma membrane and intracellular membranes, probably facilitating rapid changes in the protein composition of post-synaptic membranes (McNamara et al. 2004; Grigston et al. 2005).

Synapses are plastic and functionally diverse compartments where information is passed from the pre- to the post-synaptic cell. The amplitude of the post-synaptic response, commonly referred to as the synaptic strength, can be modulated by changes at both the pre- and post-synaptic levels (for reviews see (Murthy 1998; Atwood and Karunanithi 2002; Branco and Staras 2009; Tønnesen et al. 2018; Choquet and Triller 2013; Humeau and Choquet 2019). At the post-synapse, larger post-synaptic densities (PSD) reflect a higher number of functional receptors, and hence a stronger and more potentiated synapse (Meyer et al. 2014; Clifton et al. 2019). At the pre-synaptic level, synaptic strength can be modulated, among others, by the availability of vesicles and release machinery proteins (Jong et al. 2012). In glutamatergic neurons, pre-synaptic strength can be approximated by labelling the vesicular glutamate transporter (vGLUT1) (Grønborg et al. 2010), which reveals the entire vesicle pool. At the same time, synaptic activity can be approximated for the pre-synaptic compartment by measuring the size of the recycling pool of vesicles, using a live labelling of the vesicular protein synaptotagmin-1 (SYT1), which specifically reveals these vesicles (Willig et al. 2006; Westphal et al. 2008; Truckenbrodt et al. 2018). The recycling vesicles compose about 20 to 50% of all vesicles (Truckenbrodt et al. 2018). Their number is variable, and depends not only on the size of the total pool of vesicles, but also on many other parameters, as the metabolic age of the vesicles (Truckenbrodt et al. 2018). Therefore, although the last two measurements are related, they are not identical, with the vGLUT1 amounts providing only a measurement of the vesicle numbers, while the live SYT1 labelling also provides an indication of local activity.

The brief overview provided in this introduction indicates that the neuronal distribution of the secretory organelles is well studied, and that several lines of evidence connect them to synaptic dynamics. However, it is still unclear whether and how the characteristics of the synapses impact the abundance and localisation of the secretory pathway elements. Here, we used STED nanoscopy and quantitative image analysis to investigate the relationship between several secretory elements and synaptic activity.

By using calreticulin, ERGIC53, TGN38 and synaptopodin as markers for the ER, ERGIC, TGN and SA, respectively, we found a positive correlation between indicators of synaptic strength and the abundance of these markers in close proximity of the synaptic area. Furthermore, a read-out of presynaptic activity correlated strongly with the distribution of secretory pathway elements. Therefore, these results indicate that both the quantity and position of the secretory elements is dependent on synaptic strength and activity, presumably in order to enable an optimal synaptic response.

Methods

Sample preparation

Cultures of dissociated rat hippocampal primary neurons were prepared from postnatal P0-P2 Wistar rats of either sex and as described in (D'Este et al. 2015). Procedures were performed in accordance with the Animal Welfare Act of the Federal Republic of Germany (Tierschutzgesetz der Bundesrepublik Deutschland, TierSchG) and the Animal Welfare Laboratory Animal Regulations (Tierschutzversuchsverordnung). According to the TierSchG and the Tierschutzversuchsverordnung no ethical approval from the ethics committee is required for the procedure of sacrificing rodents for subsequent extraction of tissues, as performed in this study. The procedure for sacrificing P0-P2 rats performed in this study was supervised by animal welfare officers of the Max Planck Institute for Medical Research (MPImF) and conducted and documented according to the guidelines of the TierSchG (permit number assigned by the MPImF: MPI/T-35/18).

For the labelling of the actively recycled vesicle pool, mature cultures (17-20 days *in vitro*) were incubated for 1 hour with a Atto647N-labelled mouse antibody against the luminal domain of synaptotagmin 1 (Synaptic Systems, cat. 105 311AT1, 1:500 in culture medium). Afterwards cultures were washed three times in warm ACSF (126 mM NaCl, 2.5 mM KCl, 2.5 mM$CaCl_2$, 1.3 mM $MgCl_2$, with 30 mM Glucose, 27 mM Hepes). Labelled and unlabelled samples were fixed for 30 min in 4% PFA in PBS, pH 7.4, and quenched for 5 min in quenching buffer (PBS, 100 mM glycine, 100 mM ammonium chloride). Cells were permeabilised for 5 min in 0.1% Triton X-100 and blocked with 1% BSA for 1 hour. Samples were incubated with primary antibody dilutions in PBS for 1 hour at room temperature. Primary antibodies used were: homer1 (Synaptic Systems, cat. 160 004, 1:500 dilution), calreticulin (Cell Signaling, cat. 12238S, 1:100 dilution), ERGIC-53/p58 (Sigma E1031, 1:200 dilution), TGN38 (Sigma, cat. T9826, 1:100 dilution), synaptopodin (Synaptic Systems, cat. 163002, 1:200 dilution). Samples were washed and incubated with secondary antibody dilutions (Alexa Fluor 488 anti-guinea pig, Thermo Fisher, cat. A-11073 and Alexa Fluor 594 anti-rabbit, Thermo Fisher, cat. A-21207), Phalloidin (Alexa Fluor 405 Thermo Fisher, cat. A30104; all at 1:100 dilution) and single domain antibody against vGLUT1 (Synaptic Systems, cat. N1602-Ab635P-S, 1:200 dilution), for 1 hour at room temperature. After washing, samples were embedded in Mowiol supplemented with DABCO.

Imaging

Samples were imaged on an Abberior expert line (Abberior Instruments GmbH, Germany) with pulsed STED lines at 775 nm and 595 nm, excitation lasers at 355 nm, 405 nm, 485 nm, 580 nm, and 640 nm, and spectral detection. Detection windows were set to 650-725 nm, 600-630 nm, 505-540 nm, and 420-475 nm to detect Atto647N, Alexa Fluor 594, Alexa Fluor 488 and Alexa Fluor 405, respectively. Images were acquired with a 100x/1.4 NA magnification oil immersion lens. Pixel size was set to 30 nm, pinhole to 100 µm (1 AU). Laser powers, line accumulations and dwell times were kept consistent throughout the entire study. Alexa Fluor 594 and Atto647N were imaged semi-simultaneously during a first acquisition with STED at 775 nm, while Alexa Fluor 488 was imaged afterwards using STED at 595 nm. Confocal acquisition of the Alexa Fluor 488 channel was performed in all the image sequences to monitor lateral drift. Axial drift was minimized by the Z-focus drift compensation unit.

Image processing

Images were visualised and processed with Imspector (Abberior Instruments GmbH, Göttingen Germany) and ImageJ 1.52p (imagej.nih.gov/ij/). In the figures, images are shown as smoothed data with a low pass Gaussian filter and 5 % background subtraction. Brightness was adjusted uniformly throughout the images. For analysis of the radial intensity in average images, the ImageJ plugin radial profile plot was used. The ratio was calculated by dividing the average intensity of peripheral 35-45 radial pixels by the average intensity of the centre 10 pixels.

Data analysis

Analyses were performed in Matlab (MathWorks, Natick, MA, USA) and Python (Python Software Foundation) (**Supplementary Fig. 4**). For the automatic spine analysis, the homer, vGLUT1 or SYT1 channels were manually thresholded and used to locate the coordinates of the synapses within the image. Square regions of 3 x 3 µm, centered on the homer, vGLUT1 or SYT1 puncta were excised in order to obtain the average images shown in Fig. 2,3,4. The radial intensity values were then measured in the average images, and a ratio was calculated between a 10 pixel-wide ring in the periphery and in the center of the image. The individual image segments were binned in five ordinal groups based on the mean fluorescence intensity of the pre- or post-synapse markers, to include a similar number of synapses. For each experiment, the mean fluorescence was calculated in each bin, and was normalized to the median intensity of the experiment.

For the manual segmentation of spines **(Fig. 5 and Supplementary Fig. 7),** spines were selected based on the homer signal, which indicates the post-synaptic site, and on the actin signal, which provides the overall organization of the spine and of the dendritic shaft. A smaller selection area, of 3 x 3 µm, centred on the homer puncta, was then processed further.

The identity of the synapse was assigned (mushroom or stubby), and then the main landmarks of the spine were marked manually. These included the top, bottom, right and left borders of the head of the spine, the top and bottom points of the neck (in mushroom spines), as well as the position of the junction between the shaft and the spine neck. The spines were then aligned, relying on these landmarks, and they were overlaid, resulting in the images shown in **Fig. 5 and Supplementary Fig. 7**. The fluorescence intensity for the POIs and the synaptic markers was calculated as above. For the calculation of protein spot size, the images were automatically segmented into spots using a wavelet transformation with a Spot Detection plugin for icy (Chaumont et al. 2012; Olivo-Marin 2002). The scale 2 and an 80% threshold were used. All images were thresholded to remove background signal; regions above an empirically defined threshold were treated to contain real signals for further analysis. Outliers exceeding the range of mean ± 3 standard deviations were excluded from the analyses.

Results

Secretory pathway elements are present in proximity to post-synaptic sites

To determine whether the features of a synapse influence the local distribution and abundance of the elements of the secretory pathway, or their proximity to the synapse, we designed a high throughput experiment that enabled simultaneous super-resolution imaging of multiple proteins and parameters in cultured hippocampal neurons. The parameters selected to define synapses were the fluorescence signal intensities of the following: homer, a post-synaptic structural marker (Clifton et al. 2019); vGLUT1, a marker of the entire pre-synaptic vesicle population of excitatory nerve terminals in these cultures (Grønborg et al. 2010); and live labelling of SYT1 for identifying only the actively recycling synaptic vesicles in pre-synaptic boutons (Westphal et al. 2008). While the first two markers provide indications on the strength of the synapse, the latter is a proxy for synaptic activity (**Fig. 1a, b**). Next, we chose calreticulin, ERGIC53, TGN38 and synaptopodin as markers for the ER, ERGIC, TGN and SA, respectively. Lastly, dendritic spines were identified by phalloidin labelling of actin. Four-colour images were acquired on proximal dendrites (within ~80 µm from the soma) of primary hippocampal neurons (17-20 days *in vitro*), co-labelled with a component of the secretory pathway, homer, either vGLUT1 or SYT1, and phalloidin. All channels, with the exception of phalloidin, were acquired in STED mode, to allow an accurate localisation of the structures within the confined post-synaptic space. Using this approach, we could identify all components of the secretory pathway in proximity to the post-synaptic site in the dendritic compartment, and observed that none was present at substantial levels in the pre-synaptic boutons (**Fig. 1c, d, Supplementary Fig. 1**). The brightness of their signals was significantly higher than the background due to non-specific binding of the secondary antibody (**Supplementary Fig. 2**). While the synaptopodin signal was clearly concentrated in the spine head, calreticulin, ERGIC53 and TGN38 appeared as sparse, but distinct, spots in both the dendritic shaft and spines. On average, the number of spots per spine head was three or four, with synaptopodin being the most abundant, while calreticulin and TGN38 were the least abundant (**Supplementary Fig. 3**).

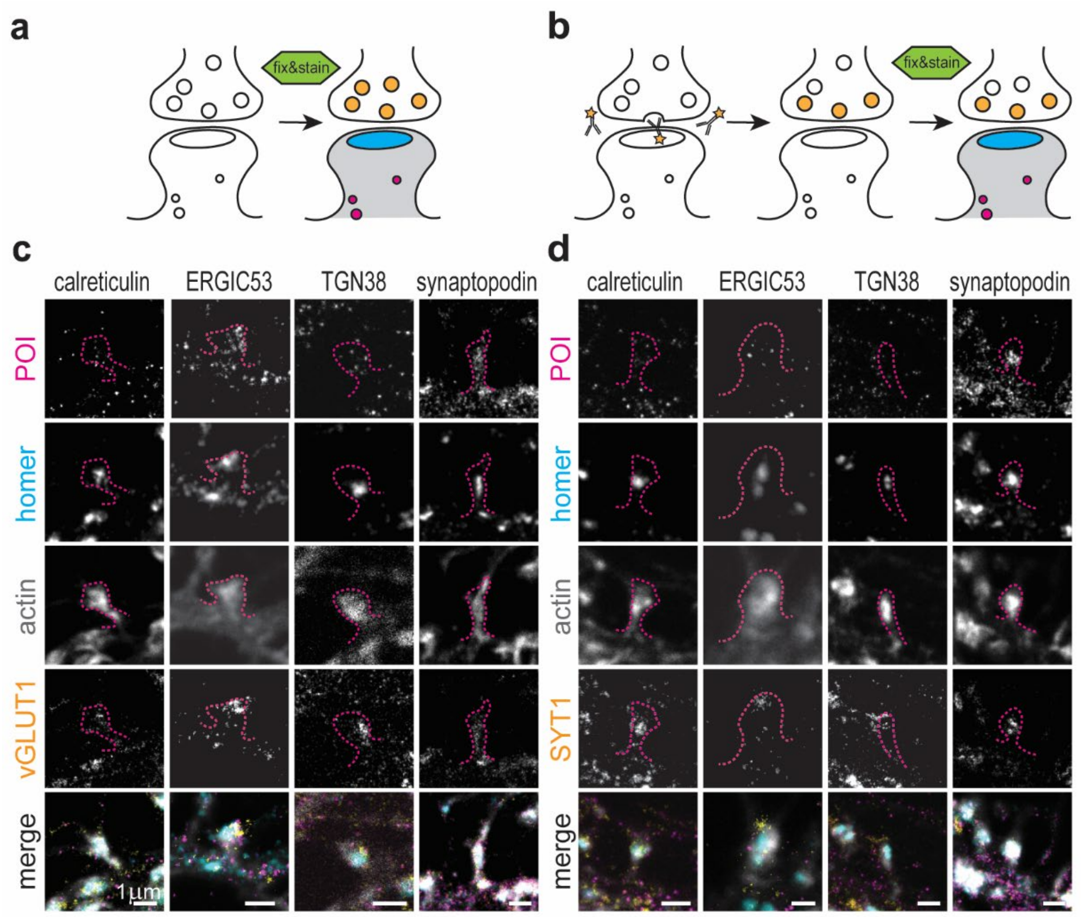

Figure 1. Experimental design and presence of secretory elements at post-synaptic sites

(a) Cells were either directly fixed and stained when visualising vGLUT1 or **(b)** incubated with an Atto647N-tagged anti-SYT1 antibody directed towards the extracellular domain of SYT1 prior to fixation. When a vesicle fuses with the pre-synaptic site, the SYT1 epitope becomes accessible to the antibody, which is incorporated by endocytosis within the recycling synaptic vesicle. Thereby, this label provides an estimate of activity at the respective synaptic boutons. **(c, d)** Representative STED images of individual synaptic sites in mature hippocampal neuron cultures. Samples were stained for several proteins of interest (POI: calreticulin, ERGIC53, TGN38, synaptopodin), with pre- and post-synaptic sites markers (vGLUT1 or SYT1, and homer, respectively), and phalloidin (actin, confocal). Secretory elements were found in the proximity of post-synaptic sites. Dashed lines represent the spine outline as labelled by phalloidin. Scale bars: 1 µm.

Post-synaptic structure correlates with the abundance of secretory pathway elements

Having identified several components of the secretory pathway in proximity to post-synaptic sites, we set out to investigate whether the post-synaptic strength influences the distribution of the dendritic secretory machinery. To this aim, we used an approach already applied for similar tasks (Wilhelm et al. 2014) and described in **Supplementary Fig. 4**. Briefly, a 3 x 3 µm area centred on the synaptic sites, regardless of its position with respect to the post-synaptic compartment, was cropped, and the homer signal intensity within this crop was evaluated. The area dimension was chosen to include the whole post-synaptic site (considering an average spine length of ~ 1.5 µm) and to minimise the contribution from neighbouring synapses or structures.

Crops were then sorted into five bins of equal size, based on homer signal intensity, and an average image of the protein of interest (POI) was generated for each bin. The average images represent the protein distribution around the synaptic sites, sorted by their respective homer intensity: a strong signal at the centre indicates a higher relative protein level in proximity of the synaptic site, while a more diffuse signal indicates that the protein is probably present in compartments more distant to the synaptic site, such as the dendritic shaft (**Fig. 2a**). Interestingly, while only a minor increase in the spread was noticed for calreticulin, ERGIC53 and synaptopodin at increasing homer intensities, TGN38 appeared vastly affected by low and intermediate post-synaptic strengths. To quantify this redistribution, a radial analysis was performed on the average images, and the ratio between the signal in the periphery and at the centre was calculated (**Fig. 2b**, **Supplementary Fig. 5a**). Low ratio values indicate a higher concentration of the POI at the synaptic site, while values close to 1 indicate a spread-out distribution. Such analysis revealed that calreticulin, ERGIC53, and synaptopodin exhibit a slight linear increase in their distribution in the area surrounding the synaptic site (the radial intensity profile ratio increased by 0.18, 0.15 and 0.13, respectively). On the other hand, TGN38 spread appeared to be modulated already by small increases in the post-synaptic strength (0.3 increase of radial intensity profile ratio between bin 1 and bin 3), but this modulation rapidly reached a plateau. From these results it could be concluded that the strength of the post-synapse has a minor influence on the distribution of the elements of the secretory pathway in the synaptic site.

To further investigate whether the observed effects on protein distribution are also connected to an increase in the protein abundance, the intensity of each POI within a bin was plotted against the intensity of the homer signal (**Fig. 2c**). A strong correlation was observed for all elements, suggesting that the abundance of these proteins is increased in the proximity of bigger post-synaptic sites. Altogether, these data indicate that homer intensity, as a proxy of the post-synaptic strength, differentially correlates with the distribution and abundance of elements of the secretory pathway.

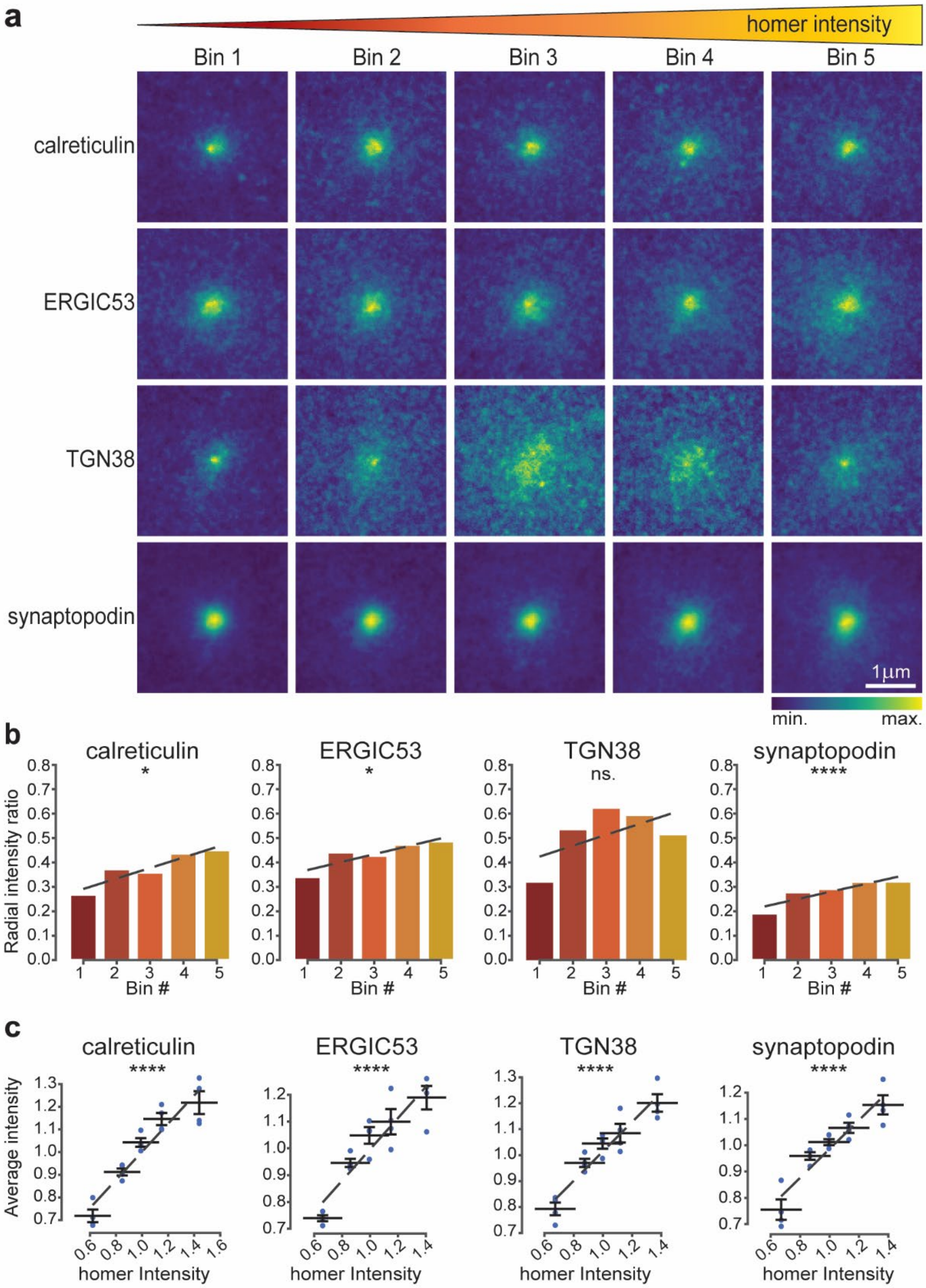

Figure 2. Correlation between post-synaptic strength and secretory pathway elements

(a) Average images for the different POIs based on five homer intensity bins displayed in 3 x 3 µm crops around the synaptic site. Bin 1 has the lowest homer intensity and bin 5 the highest. **(b)** Ratio between signal intensity at the periphery and at the centre of the average images, calculated by radial analysis. **(c)** Correlation of homer intensities and the average intensities of the POIs. Dashed lines are linear fits. All data was collected from four independent experiments. *=$p<0.05$, **=$p<0.01$, ***=$p<0.001$, ****=$p<0.0001$, and ns.=non-significant. Whiskers represent S.E.M. Number of synapses per bin and Spearman's rho are listed in Supplementary Table 1.

The abundance of post-synaptic secretory pathway elements also correlates with pre-synaptic strength

After having investigated the relationship between secretory pathway elements and post-synaptic site size, we wondered whether the same influence could be observed for the pre-synaptic site traits. The question is highly relevant, since in our experimental setup there is no significant correlation between pre- and post-synaptic site strength (**Supplementary Fig. 6**). Therefore, we performed the same analysis as conducted above, but we analysed the vGLUT1 intensity instead of that of homer, thereby estimating the size of the synaptic vesicle pool in the pre-synapse. Labelling of vGLUT1 was achieved using a primary nanobody, which provided a well-defined number of fluorophores per labelled structure (Sograte-Idrissi et al. 2020). The resulting averaged images for the different secretory elements showed a mixed pattern of responses (**Fig. 3a, b**, **Supplementary Fig. 5b**). Calreticulin and synaptopodin exhibit a linear redistribution at increasing vGLUT1 intensities, visible from both the average images and the radial analysis (the radial intensity profile ratios increased by 0.36 and 0.25, respectively). This increase was less pronounced, and was also non-linear, in the case of ERGIC53 (0.15 increase in radial intensity profile ratio), and was abolished for TGN38 (-0.05 decrease in radial intensity profile ratio), whose distribution fluctuated between the different bins. Therefore, the influence of vGLUT1 abundance, as representation of pre-synaptic strength, on the distribution of post-synaptic elements of the secretory pathways appears heterogeneous.

When analysing the intensities of the POIs with respect to vGLUT1 intensity, all elements exhibited a clear linear correlation, which was particularly strong for calreticulin, TGN38, and synaptopodin (**Fig. 3c**). These data indicate that larger quantities of secretory pathway proteins are recruited into the post-synapses opposing strong pre-synapses. With the exception of TGN38, the higher quantity of POIs seems also to be reflected by their more dispersed distribution in the dendritic regions neighbouring the post-synaptic site.

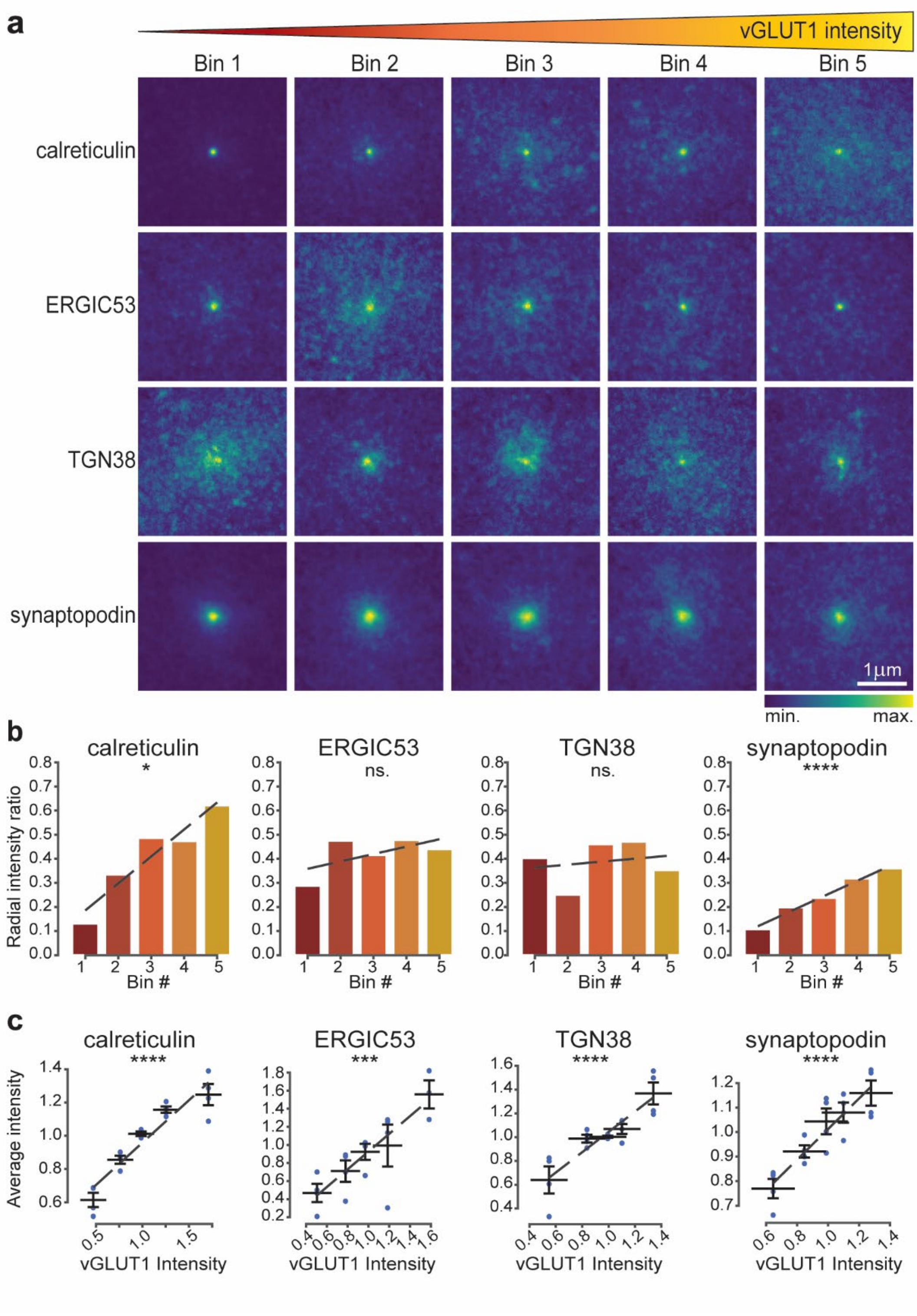

Figure 3. Correlation between pre-synaptic strength and secretory pathway elements

(a) Average images for the different POIs based on five vGLUT1 intensity bins displayed in 3 x 3 µm crops around the synaptic site. Bin 1 has the lowest vGLUT1 intensity and bin 5 the highest. **(b)** Ratio between signal intensity at the periphery and at the centre of the average images calculated based on radial analysis. **(c)** Correlation of vGLUT1 intensities and the average intensities of the POIs. Dashed lines are linear fits. All data was collected from four independent experiments. *=p<0.05, **=p<0.01, ***=p<0.001, ****=p<0.0001, and ns.=non-significant. Whiskers represent S.E.M. Numbers of synapses per bin and Spearman's rho are listed in Supplementary Table 1.

The distribution of post-synaptic secretory pathway elements is highly dependent on pre-synaptic activity

After having assessed the relationship between post- and pre-synaptic strength and secretory pathway components, we proceeded to address the existence of a functional correlation to synaptic activity. To this aim, we replaced vGLUT1 labelling by live-SYT1 staining in our experimental setup (**Fig. 1b, d**), which provided an estimate of synaptic activity based on the level of actively recycled vesicles. To our surprise, all POIs, including TGN38, showed a linear redistribution at increasing SYT1 intensities, as demonstrated by both average images and radial analysis (**Fig. 4a, b**, **Supplementary Fig. 5c**). For all POIs, the differences between the radial intensity profile ratios of bins 5 and 1 was higher than those observed for homer and vGLUT1 (**Fig. 2b, Fig. 3b**). This difference was least prominent for synaptopodin (0.3 increase in radial intensity ratio), and most prominent for calreticulin (0.45 increase in radial intensity ratio). Therefore, one can conclude that the localisation of all of the analysed post-synaptic elements of the secretory pathway is intimately linked to the amount of recycling vesicles and hence to pre-synaptic activity.

When correlating the POIs levels to SYT1 intensities, we found only a small correlation with calreticulin abundance in the region neighbouring the synaptic sites (**Fig. 4c**). On the contrary, the amounts of ERGIC53, TGN38, and synaptopodin were strongly correlated with SYT1 intensity. Taken together, these data indicate that the secretory organelles at the synapse are increasingly dispersed with increasing amounts of recycling vesicles, though the effect of activity on their abundance varies depending on the organelle.

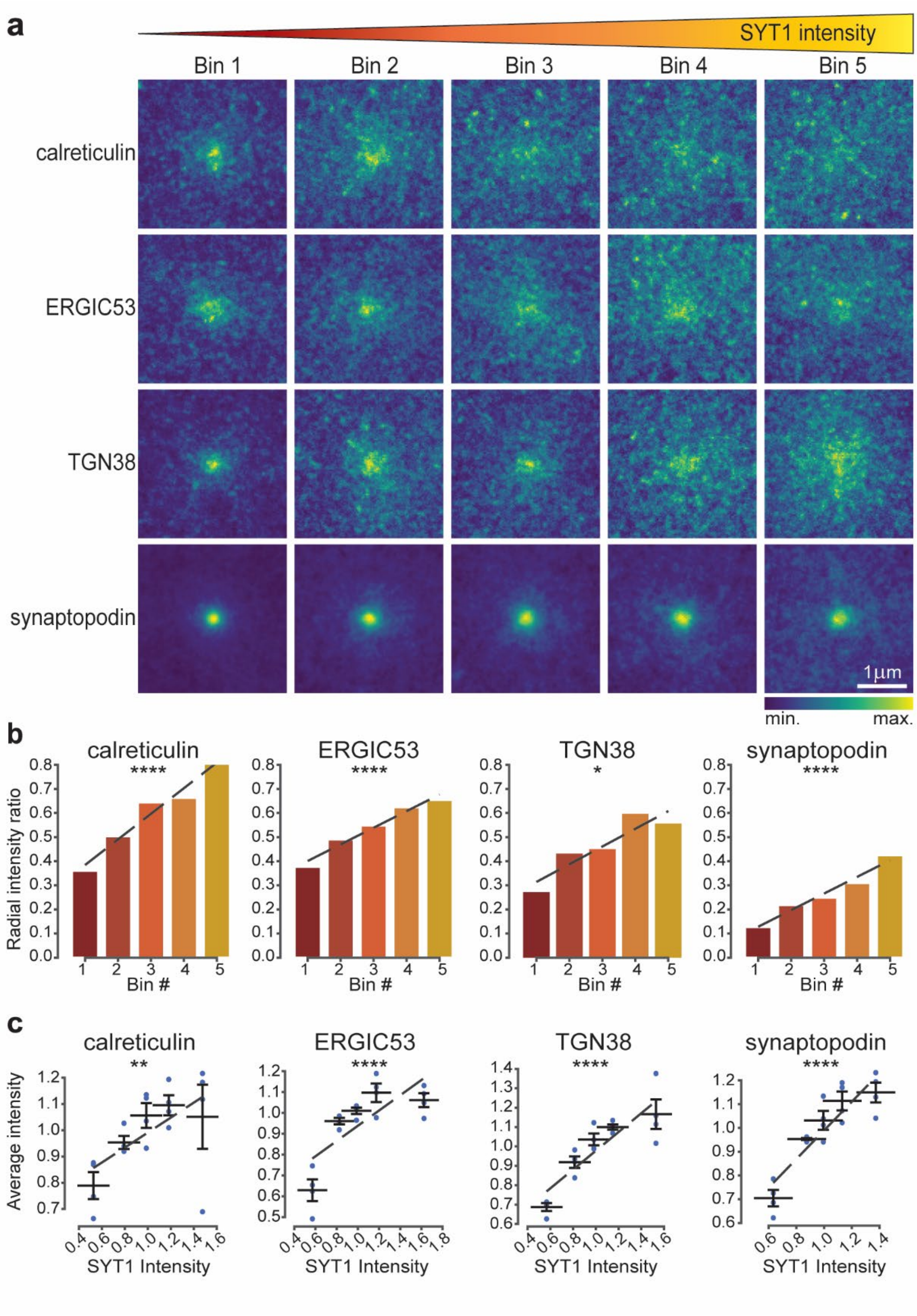

Figure 4. Correlation between pre-synaptic activity and secretory pathway elements

(a) Average images for the different POIs based on five SYT1 intensity bins displayed in 3 x 3 µm crops around the synaptic site. Bin 1 has the lowest SYT1 intensity and bin 5 the highest. **(b)** Ratio between signal intensity at the periphery and at the centre of the average images calculated based on radial analysis. **(c)** Correlation of SYT1 intensities and the average intensities of the POIs. Dashed lines are linear fits. All was data collected from four independent experiments. *=p<0.05, **=p<0.01, ***=p<0.001, ****=p<0.0001, and ns.=non-significant. Whiskers represent S.E.M. Numbers of synapses per bin and Spearman's rho are listed in Supplementary Table 1.

Post-synaptic strength strongly modulates the secretory machinery in mushroom spines

The analyses conducted so far assessed how synaptic strength and activity relate to the abundance of secretory pathway elements in the synapse and the extent of their dispersion, without considering the actual size of the spines containing them. Furthermore, it did not discriminate between different spine morphologies. To account for this, a manual classification and segmentation of spines was performed based on the actin (phalloidin) staining. In this way, spines that had a clear mushroom or stubby morphology were selected from the 3 x 3 μm crops, and their axes were aligned. The corresponding average images confirmed the results obtained with the automatic analysis in the previous figures, and demonstrated that the signal of the POIs derives predominantly from the dendritic, rather than the axonal compartment (**Fig. 5a** and **Supplementary Fig. 7**). The POIs were enriched in proximity to the synaptic site, with TGN38 having the most dispersed distribution, and synaptopodin the most confined distribution in both spine types. Furthermore, the average intensity for most of the POIs was comparable between both mushroom and stubby spines, and only synaptopodin showed a slight enrichment in mushroom spines, as expected from the literature (**Supplementary Fig. 8**) (Jedlicka and Deller 2017; Vlachos 2012).

The analysis of the manually segmented images indicated that the levels of all POIs strongly correlated with homer levels, regardless of the spine type. Moreover, in mushroom spines most POIs correlated with vGLUT1 intensity (**Fig. 5b, c** and **Supplementary Fig. 9**). This positive correlation is most likely due to the fact that the number of POI spots in the spine head grows with the size of the post-synaptic site. However, the size of the spots decreased with increasing post-synaptic density size (**Supplementary Fig. 10**), suggesting the presence of more but smaller organelles. These results confirmed the previously observed correlations between the abundance of secretory pathway elements and markers of pre- and post-synaptic strength, as was assessed with the automatic analysis presented above (**Fig. 2, 3**).

When analysing the synaptic activity in the manually segmented images, however, a correlation was observed exclusively in mushroom spines, and only for ERGIC53, TGN38, and synaptopodin (**Fig. 5d**). The previously observed correlation for calreticulin was lost in both spine types. Therefore, these results suggest that the structure of the pre- and post-synaptic site has a high impact in regulating the amount of secretory pathway elements present in the neighbouring post-synaptic regions, and that pre-synaptic activity has differential effects, depending on the post-synaptic morphology.

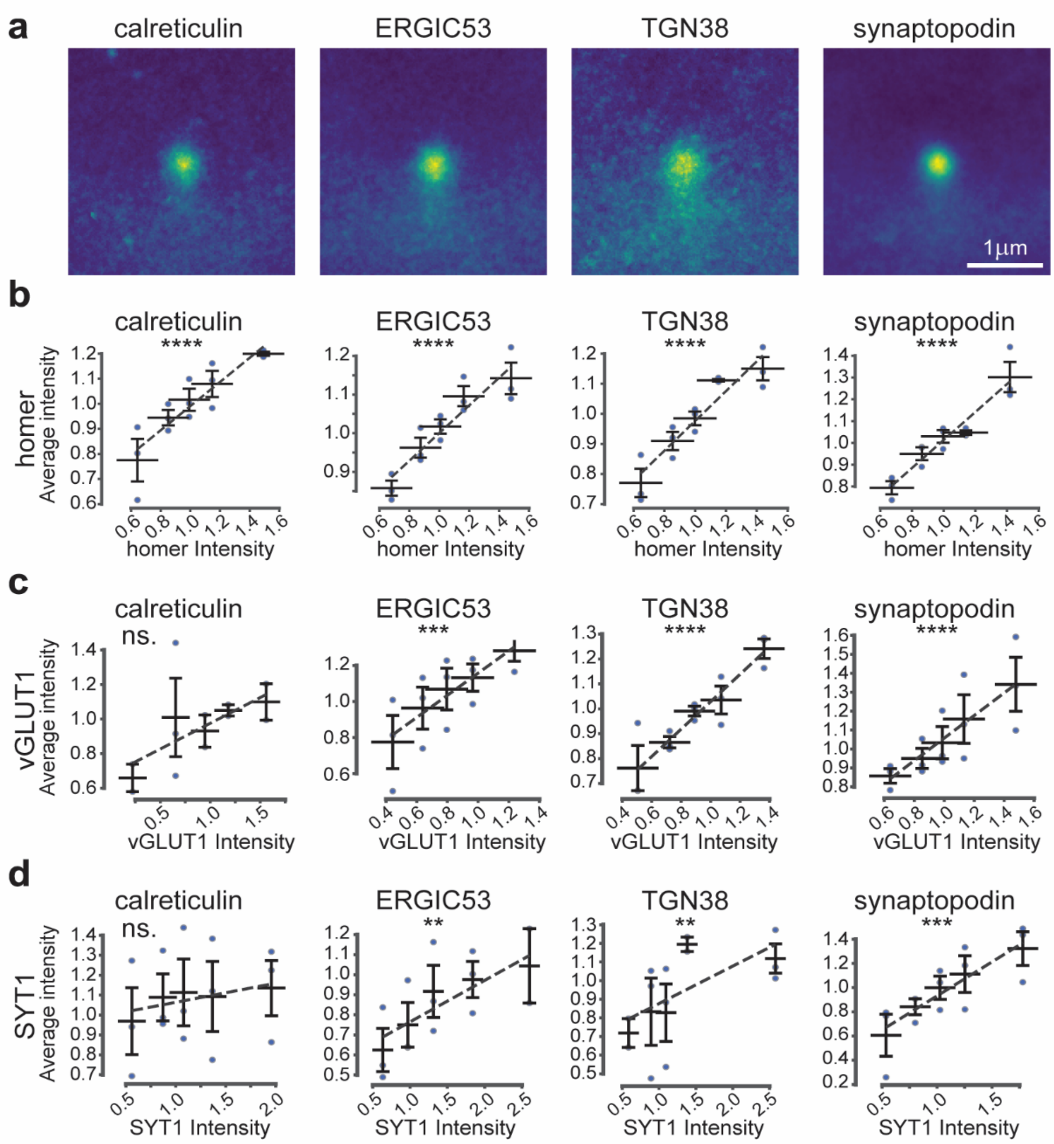

Figure 5. Correlations of secretory elements in mushroom spines

(a) Average 3 x 3 µm images of POIs in mushroom spines as defined by manual segmentation. Images were vertically aligned with the spine head at the centre and the dendritc shaft at the bottom. All data were collected from three independent experiments. **(b-d)** Average intesity correlations after manual spine segmentation and classification as mushroom type spines. Correlation of the average intesities of calreticulin, ERGIC53, TGN38, and synaptopodin with average intensities of homer **(b)**, vGLUT1 **(c)**, and SYT1 **(d)**. Where *=p<0.05, **=p<0.01, ***=p<0.001, ****=p<0.0001, and ns.=non-significant. Whiskers represent S.E.M. Number of synapses per bin and Spearman's rho are listed in Supplementary Table 1.

Discussion

Neurons have a highly elaborated network of secretory elements that allows for locally-independent production and processing of proteins (Rangaraju et al. 2017; Holt et al. 2019; Hafner et al. 2019; Nakahata and Yasuda 2018; Biever et al. 2019). However, the extent to which synaptic activity, size and morphology steer local protein synthesis machinery is not fully understood (Kennedy and Hanus 2019; Bailey et al. 2015). Here we systematically analysed the abundance and distribution of several secretory elements at synaptic sites by means of STED optical nanoscopy, in dependence of proxies of synaptic strength and activity. With quantitative image analysis, we investigated the correlations between the abundance and distribution of calreticulin (endoplasmic reticulum marker), ERGIC53 (ER-Golgi intermediate compartment marker), TGN38 (trans-Golgi network marker), and synaptopodin (spine apparatus marker), and the pre-synaptic markers vGLUT1 or SYT1, as well as the post-synaptic marker homer.

The use of optical nanoscopy has the advantage of providing molecular specificity and allowing the unambiguous discrimination of organelles, which can be difficult in electron microscopy (Wu et al. 2017). Furthermore, a higher throughput required for extensive analyses, and the visualisation of the entire three-dimensional synaptic site are both more easily achievable with optical microscopy. However, in case of overlapping structure, signal coming from superimposed compartments or synaptic sites could be misinterpreted, since the axial resolution in two-dimensional STED is limited to 500-700 nm. Moreover, the results are influenced by the specificity of the markers for the structures of interest and by the precision of the related antibodies, which were validated by western blot and STED imaging in cell lines (**Supplementary Fig. 11**). In the context of this study, this is relevant for synaptopodin, since it is not uniquely a spine apparatus marker, and it can be found in spines prior to the formation of the spine apparatus, as well as in the axon initial segment (Chirillo et al. 2019; Schlüter et al. 2017). Lastly, the presence of non-specific binding of the primary antibody cannot be completely ruled out and could only be verified on cultures derived from knock-out animals.

Our data analysis was largely automated, thus limiting biases in the image quantification and evaluation. With this approach, thousands of synaptic sites could be analysed to gain information on the behaviour of the “average” synaptic site. However, rare events are not represented, as they would require the manual inspection of each individual site in order to be identified. One bias of our analysis is that larger post-synaptic sites, particularly when considering the manually selected mushroom or stubby spines, will intrinsically lead to a higher occupancy of the image space and thus to higher protein levels (assuming that the proteins are homogeneously distributed in the spine head). However, none of the proteins we analysed exhibits a volume labelling-like staining, limiting this drawback. The manual identification of post-synaptic sites might also intrinsically predispose to the selection of bigger synaptic sites, whose behaviour may not be representative of all synapses. This influence might explain, to some extent, the differences observed between automated and manually selected synapse.

Lastly, it should be mentioned that in our experimental setup no correlation between the levels of vGLUT1 and homer was observed (**Supplementary Fig. 6**). Therefore, the responses of the POIs to pre- and post- synaptic strength can be considered independently from each other.

STED imaging showed a higher concentration of some of the chosen markers in the soma or along the apical dendrite. Nevertheless, in our experimental setup all POIs could be identified unambiguously in the dendritic shafts and at post-synaptic compartments. According to previous studies, the ERGIC was proposed to be rarely present in dendritic spines (Bowen et al. 2017). However, it should be noted that in electron microscopy the ERGIC resembles endosomes, which are often found in spines, and therefore this similarity might lead to misinterpretation of the images (Wu et al. 2017). Furthermore, fine ERGIC53 puncta could be easily overseen or mislocalised when using diffraction-limited light microscopy. Regarding TGN38, a detailed description of its presence at synaptic sites has so far been reported only in overexpression experiments, and was not investigated in detail at endogenous levels (Gardiol et al. 1999; McNamara et al. 2004; Cox and Racca 2013).

Overall, we found strong correlations of the expression levels of the components of the secretory pathway to synaptic strength and activity, and in particular to the post-synaptic size (**Fig. 6a**). However, several details should be discussed for each of the individual markers. Calreticulin distribution was dependent on post-synaptic size, and even stronger effects were observed for pre-synaptic strength and activity. The amounts of the protein were dependent on the strength of the synapse, but correlated less with synaptic activity. The correlation with pre-synaptic markers was heavily abolished when analysing mushroom and stubby spines specifically. These effects are in line with a model in which synaptic activity recruits the local ER resources to the synaptic site, thereby explaining the correlation between activity and calreticulin distribution. Later on, persistent activity results in the recruitment of the ER from more distant areas, thereby leading to an increase in ER abundance and explaining the correlation between calreticulin levels and synaptic strength. This model is in agreement with the evidence that the ER has a high turnover and that it primes new spines for future plasticity, contributing to LTP (Toresson and Grant 2005; Chirillo et al. 2019; Kulik et al. 2019).

ERGIC53 levels directly correlated with the levels of all three synaptic markers, also in mushroom spines, and its distribution was mainly affected by pre-synaptic activity. These results suggest that ERGIC-mediated protein trafficking is required for the maintenance of synaptic strength (and presumably for plasticity), and that it responds readily to synaptic activity, in agreement with previous investigations (Hanus et al. 2014).

The TGN38 behaviour was to some extent similar to that of ERGIC53. The TGN38 distribution in connection to post-synaptic strength appears highly sensitive to changes for low homer intensities, and becomes saturated for high values. The pre-synaptic strength appears to have no effect on the TGN38 localisation.

Pre-synaptic activity correlated strongly with both TGN38 distribution and levels, but this correlation was strongly reduced when manually segmenting spines. This difference might be ascribed to the analysis itself: (i) mushroom and stubby spines that can be identified unambiguously may already be relatively mature, and therefore maintenance mechanisms will predominate over plasticity; (ii) both spine types generally have the synaptic contact in the head region, and hence to some distance from the dendritic shaft, whose contribution in the analysis is therefore reduced. Therefore, a potential recruitment of TGN38 in the shaft region would be quantified in the automatic analysis, but would not be measured in the analysis of the individual spine types. We therefore propose that TGN38 is mobilised in the proximity of the post-synapse, in relation to activity, but not necessarily in the spine head. Some of the TGN38 molecules may have been synthesised in response to activity (Grigston et al. 2005), albeit this is only speculative, since the age of the compartments was not analysed in our experiments.

In principle, one would expect a strong similarity between the ERGIC and TGN compartments. However, neurons also have unconventional secretion pathways that bypass the TGN (Hanus et al. 2016), thereby explaining why these compartments do not behave in an identical fashion.

Synaptopodin showed a strong correlation to all synaptic markers and in both automatically and manually selected mushroom spines. On the other hand, synaptopodin distribution seemed to be less influenced by post-synaptic strength but more by pre-synaptic modulations. Because of its functions, synaptopodin is specifically accumulated in the spine head and neck in mushroom spines (Jedlicka and Deller 2017; Deller et al. 2007; Vlachos 2012). Therefore, it is not surprising that all tested synaptic characteristic proxies showed a good correlation with synaptopodin abundance, and that even at increasing post-synaptic strength, synaptopodin stayed in close synaptic proximity. However, it is important to consider that the presence of synaptopodin in the spines is not necessarily related to the presence of the SA, and therefore the results might be partially connected to the ability of synaptopodin to bind the actin cytoskeleton (Jedlicka and Deller 2017; Deller et al. 2007; Segal et al. 2010; Vlachos 2012).

Altogether, our data suggests that the pre-synaptic activity has the highest influence on the distribution of secretory pathway elements in the proximity of post-synaptic sites, while the post-synaptic architecture has the highest influence on their abundance. Therefore, we propose a model in which increased synaptic activity initially mobilises the locally available resources to the synaptic area. Sustained activity then leads to increases in synapse strength, and promotes the recruitment of more secretory organelles that are important for the maintenance of the large synapses (**Fig. 6b**). However, it should be noted that the observed effects are not homogenous for all the components of the secretory pathway, further proving the presence of unconventional pathways in neurons (Hanus et al. 2016).

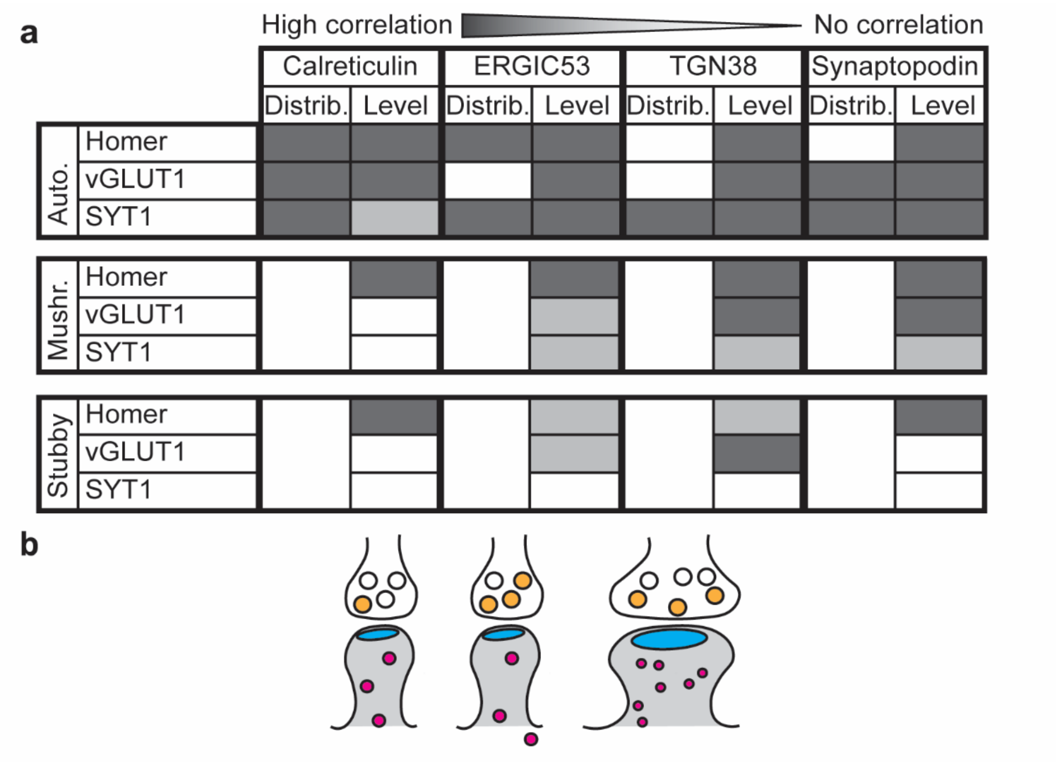

		Calreticulin		ERGIC53		TGN38		Synaptopodin	
		Distrib.	Level	Distrib.	Level	Distrib.	Level	Distrib.	Level
Auto.	Homer	■	■	■	■	□	■	□	■
	vGLUT1	■	■	□	■	□	■	■	■
	SYT1	■	▒	■	■	■	■	■	■
Mushr.	Homer	□	■	□	■	□	■	□	■
	vGLUT1		□		▒		■		■
	SYT1		□		▒		▒		▒
Stubby	Homer	□	■	□	▒	□	▒	□	■
	vGLUT1		□		▒		■		□
	SYT1		□		□		□		□

Figure 6. Summary of effects and proposed model

(**a**) Summary of the correlation between the elements of the secretory pathway (in terms of distribution and levels), and post-synaptic strength (homer), pre-synaptic strength (vGLUT1), or pre-synaptic activity (SYT1) for the different analysis performed (automatic analysis of all synapses, or manual analyses of mushroom spines and stubby spines). The different shades of gray correspond to high correlation/influence (darker gray), or less (light gray) to no (white) correlation/influence. (**b**) Model for the effect of synaptic strength and activity on the elements of the secretory pathway. Increased activity initially mobilizes the locally available resources, whose availability increases to support spine enlargement and maintenance.

A basic conclusion of our study is that both pre- and post-synaptic features correlate in multiple ways to the post-synaptic secretory pathway. Further work will be required to understand the exact synaptic mechanisms modulating protein secretion in the context of synaptic plasticity and activity. Finally, the behaviour of other organelles, such as the Golgi outposts and the recycling endosomes, should also be considered in the future.

Acknowledgements

The work has been supported by the Deutsche Forschungsgemeinschaft (DFG) (SFB1286/A03 to S.O.R. and SFB1286/A07 to E.D.). We thank Jasmine Hubrich for the support with experimental work. We thank Dr. Jade Cottam Jones, Dr. Richard Lincoln, Angel Cereceda Delgado, and Victor Macarron Palacios for the critical reading of the manuscript.

Author contributions

C.M.G and T.M.D. acquired and analysed data. S.O.R. and E.D. designed research. C.M.G., T.M.D., S.O.R. and E.D. wrote the manuscript.

Competing interest

S.O.R. is funder shareholder of NanoTag Biotechnologies. S.O.R. received compensation as consultant of NanoTag Biotechnologies. All the other authors declare no competing interests.

References

Aebi, Markus; Bernasconi, Riccardo; Clerc, Simone; Molinari, Maurizio (2010): N-glycan structures: recognition and processing in the ER. In *Trends in biochemical sciences* 35 (2), pp. 74–82. DOI: 10.1016/j.tibs.2009.10.001.

Atwood, Harold L.; Karunanithi, Shanker (2002): Diversification of synaptic strength: presynaptic elements. In *Nature reviews. Neuroscience* 3 (7), pp. 497–516. DOI: 10.1038/nrn876.

Bailey, Craig H.; Kandel, Eric R.; Harris, Kristen M. (2015): Structural Components of Synaptic Plasticity and Memory Consolidation. In *Cold Spring Harbor perspectives in biology* 7 (7), a021758. DOI: 10.1101/cshperspect.a021758.

Bas Orth, Carlos; Vlachos, Andreas; Del Turco, Domenico; Burbach, Guido J.; Haas, Carola A.; Mundel, Peter et al. (2005): Lamina-specific distribution of Synaptopodin, an actin-associated molecule essential for the spine apparatus, in identified principal cell dendrites of the mouse hippocampus. In *The Journal of comparative neurology* 487 (3), pp. 227–239. DOI: 10.1002/cne.20539.

Biever, Anne; Donlin-Asp, Paul G.; Schuman, Erin M. (2019): Local translation in neuronal processes. In *Current opinion in neurobiology* 57, pp. 141–148. DOI: 10.1016/j.conb.2019.02.008.

Biever, Anne; Glock, Caspar; Tushev, Georgi; Ciirdaeva, Elena; Dalmay, Tamas; Langer, Julian D.; Schuman, Erin M. (2020): Monosomes actively translate synaptic mRNAs in neuronal processes. In *Science (New York, N.Y.)* 367 (6477). DOI: 10.1126/science.aay4991.

Bowen, Aaron B.; Bourke, Ashley M.; Hiester, Brian G.; Hanus, Cyril; Kennedy, Matthew J. (2017): Golgi-independent secretory trafficking through recycling endosomes in neuronal dendrites and spines (6).

Branco, Tiago; Staras, Kevin (2009): The probability of neurotransmitter release: variability and feedback control at single synapses. In *Nature reviews. Neuroscience* 10 (5), pp. 373–383. DOI: 10.1038/nrn2634.

Chaumont, Fabrice de; Dallongeville, Stéphane; Chenouard, Nicolas; Hervé, Nicolas; Pop, Sorin; Provoost, Thomas et al. (2012): Icy: an open bioimage informatics platform for extended reproducible research. In *Nature methods* 9 (7), pp. 690–696. DOI: 10.1038/nmeth.2075.

Chen, Annie; Gössling, Enno K.; Witkowski, Leora; Bhindi, Amar; Bauch, Carola; Roussy, Geneviève et al. (2012): Regional and subcellular distribution of the receptor-targeting protein PIST in the rat central nervous system. In *The Journal of comparative neurology* 520 (5), pp. 889–913. DOI: 10.1002/cne.22774.

Chirillo, Michael A.; Waters, Mikayla S.; Lindsey, Laurence F.; Bourne, Jennifer N.; Harris, Kristen M. (2019): Local resources of polyribosomes and SER promote synapse enlargement and spine clustering after long-term potentiation in adult rat hippocampus. In *Scientific reports* 9 (1), p. 3861. DOI: 10.1038/s41598-019-40520-x.

Choquet, Daniel; Triller, Antoine (2013): The dynamic synapse. In *Neuron* 80 (3), pp. 691–703. DOI: 10.1016/j.neuron.2013.10.013.

Clifton, Nicholas E.; Trent, Simon; Thomas, Kerrie L.; Hall, Jeremy (2019): Regulation and Function of Activity-Dependent Homer in Synaptic Plasticity. In *Molecular neuropsychiatry* 5 (3), pp. 147–161. DOI: 10.1159/000500267.

Cox, David J.; Racca, Claudia (2013): Differential dendritic targeting of AMPA receptor subunit mRNAs in adult rat hippocampal principal neurons and interneurons. In *The Journal of comparative neurology* 521 (9), pp. 1954–2007. DOI: 10.1002/cne.23292.

Deller, T.; Merten, T.; Roth, S. U.; Mundel, P.; Frotscher, M. (2000a): Actin-associated protein synaptopodin in the rat hippocampal formation: localization in the spine neck and close association with the spine apparatus of principal neurons. In *The Journal of comparative neurology* 418 (2), pp. 164–181. DOI: 10.1002/(sici)1096-9861(20000306)418:2<164::aid-cne4>3.0.co;2-0.

Deller, T.; Mundel, P.; Frotscher, M. (2000b): Potential role of synaptopodin in spine motility by coupling actin to the spine apparatus. In *Hippocampus* 10 (5), pp. 569–581. DOI: 10.1002/1098-1063(2000)10:5<569::AID-HIPO7>3.0.CO;2-M.

Deller, Thomas; Bas Orth, Carlos; Del Turco, Domenico; Vlachos, Andreas; Burbach, Guido J.; Drakew, Alexander et al. (2007): A role for synaptopodin and the spine apparatus in hippocampal synaptic plasticity. In *Annals of anatomy = Anatomischer Anzeiger : official organ of the Anatomische Gesellschaft* 189 (1), pp. 5–16. DOI: 10.1016/j.aanat.2006.06.013.

Deller, Thomas; Korte, Martin; Chabanis, Sophie; Drakew, Alexander; Schwegler, Herbert; Stefani, Giulia Good et al. (2003): Synaptopodin-deficient mice lack a spine apparatus and show deficits in synaptic plasticity. In *Proceedings of the National Academy of Sciences of the United States of America* 100 (18), pp. 10494–10499. DOI: 10.1073/pnas.1832384100.

D'Este, Elisa; Kamin, Dirk; Göttfert, Fabian; El-Hady, Ahmed; Hell, Stefan W. (2015): STED nanoscopy reveals the ubiquity of subcortical cytoskeleton periodicity in living neurons. In *Cell reports* 10 (8), pp. 1246–1251. DOI: 10.1016/j.celrep.2015.02.007.

Gardiol, Alejandra; Racca, Claudia; Triller, Antoine (1999): Dendritic and Postsynaptic Protein Synthetic Machinery. In *J. Neurosci.* 19 (1), pp. 168–179. DOI: 10.1523/JNEUROSCI.19-01-00168.1999.

Glock, Caspar; Heumüller, Maximilian; Schuman, Erin M. (2017): mRNA transport & local translation in neurons. In *Current opinion in neurobiology* 45, pp. 169–177. DOI: 10.1016/j.conb.2017.05.005.

Griffiths, G.; Simons, K. (1986): The trans Golgi network: sorting at the exit site of the Golgi complex. In *Science (New York, N.Y.)* 234 (4775), pp. 438–443. DOI: 10.1126/science.2945253.

Grigston, Jeffrey C.; VanDongen, Hendrika M. A.; McNamara, James O.; VanDongen, Antonius M. J. (2005): Translation of an integral membrane protein in distal dendrites of hippocampal neurons. In *The European journal of neuroscience* 21 (6), pp. 1457–1468. DOI: 10.1111/j.1460-9568.2005.03999.x.

Grønborg, Mads; Pavlos, Nathan J.; Brunk, Irene; Chua, John J. E.; Münster-Wandowski, Agnieszka; Riedel, Dietmar et al. (2010): Quantitative comparison of glutamatergic and GABAergic synaptic vesicles unveils selectivity for few proteins including MAL2, a novel synaptic vesicle protein. In *J. Neurosci.* 30 (1), pp. 2–12. DOI: 10.1523/JNEUROSCI.4074-09.2010.

Hafner, Anne-Sophie; Donlin-Asp, Paul G.; Leitch, Beulah; Herzog, Etienne; Schuman, Erin M. (2019): Local protein synthesis is a ubiquitous feature of neuronal pre- and postsynaptic compartments. In *Science (New York, N.Y.)* 364 (6441). DOI: 10.1126/science.aau3644.

Hanus, Cyril; Geptin, Helene; Tushev, Georgi; Garg, Sakshi; Alvarez-Castelao, Beatriz; Sambandan, Sivakumar et al. (2016): Unconventional secretory processing diversifies neuronal ion channel properties. In *eLife* 5. DOI: 10.7554/eLife.20609.

Hanus, Cyril; Kochen, Lisa; Tom Dieck, Susanne; Racine, Victor; Sibarita, Jean-Baptiste; Schuman, Erin M.; Ehlers, Michael D. (2014): Synaptic control of secretory trafficking in dendrites. In *Cell reports* 7 (6), pp. 1771–1778. DOI: 10.1016/j.celrep.2014.05.028.

Holt, Christine E.; Martin, Kelsey C.; Schuman, Erin M. (2019): Local translation in neurons: visualization and function. In *Nature structural & molecular biology* 26 (7), pp. 557–566. DOI: 10.1038/s41594-019-0263-5.

Horton, April C.; Rácz, Bence; Monson, Eric E.; Lin, Anna L.; Weinberg, Richard J.; Ehlers, Michael D. (2005): Polarized secretory trafficking directs cargo for asymmetric dendrite growth and morphogenesis. In *Neuron* 48 (5), pp. 757–771. DOI: 10.1016/j.neuron.2005.11.005.

Humeau, Yann; Choquet, Daniel (2019): The next generation of approaches to investigate the link between synaptic plasticity and learning. In *Nature neuroscience* 22 (10), pp. 1536–1543. DOI: 10.1038/s41593-019-0480-6.

Jedlicka, Peter; Deller, Thomas (2017): Understanding the role of synaptopodin and the spine apparatus in Hebbian synaptic plasticity - New perspectives and the need for computational modeling. In *Neurobiology of learning and memory* 138, pp. 21–30. DOI: 10.1016/j.nlm.2016.07.023.

Jong, Arthur P. H. de; Schmitz, Sabine K.; Toonen, Ruud F. G.; Verhage, Matthijs (2012): Dendritic position is a major determinant of presynaptic strength. In *The Journal of cell biology* 197 (2), pp. 327–337. DOI: 10.1083/jcb.201112135.

Kennedy, Matthew J.; Hanus, Cyril (2019): Architecture and Dynamics of the Neuronal Secretory Network. In *Annual review of cell and developmental biology* 35, pp. 543–566. DOI: 10.1146/annurev-cellbio-100818-125418.

Kulik, Yelena D.; Watson, Deborah J.; Cao, Guan; Kuwajima, Masaaki; Harris, Kristen M. (2019): Structural plasticity of dendritic secretory compartments during LTP-induced synaptogenesis (8).

Lowenstein, P. R.; Morrison, E. E.; Bain, D.; Shering, A. F.; Banting, G.; Douglas, P.; Castro, M. G. (1994): Polarized distribution of the trans-Golgi network marker TGN38 during the in vitro development of neocortical neurons: effects of nocodazole and brefeldin A. In *The European journal of neuroscience* 6 (9), pp. 1453–1465. DOI: 10.1111/j.1460-9568.1994.tb01007.x.

McNamara, James O.; Grigston, Jeffrey C.; VanDongen, Hendrika M. A.; VanDongen, Antonius M. J. (2004): Rapid dendritic transport of TGN38, a putative cargo receptor. In *Brain research. Molecular brain research* 127 (1-2), pp. 68–78. DOI: 10.1016/j.molbrainres.2004.05.013.

Meyer, Daniel; Bonhoeffer, Tobias; Scheuss, Volker (2014): Balance and stability of synaptic structures during synaptic plasticity. In *Neuron* 82 (2), pp. 430–443. DOI: 10.1016/j.neuron.2014.02.031.

Mikhaylova, Marina; Bera, Sujoy; Kobler, Oliver; Frischknecht, Renato; Kreutz, Michael R. (2016): A Dendritic Golgi Satellite between ERGIC and Retromer. In *Cell reports* 14 (2), pp. 189–199. DOI: 10.1016/j.celrep.2015.12.024.

Mundel, P.; Heid, H. W.; Mundel, T. M.; Krüger, M.; Reiser, J.; Kriz, W. (1997): Synaptopodin: an actin-associated protein in telencephalic dendrites and renal podocytes. In *The Journal of cell biology* 139 (1), pp. 193–204. DOI: 10.1083/jcb.139.1.193.

Murthy, Venkatesh N. (1998): Synaptic plasticity: Step-wise strengthening. In *Current Biology* 8 (18), R650-R653. DOI: 10.1016/S0960-9822(07)00414-9.

Nakahata, Yoshihisa; Yasuda, Ryohei (2018): Plasticity of Spine Structure: Local Signaling, Translation and Cytoskeletal Reorganization. In *Frontiers in synaptic neuroscience* 10, p. 29. DOI: 10.3389/fnsyn.2018.00029.

Olivo-Marin, Jean-Christophe (2002): Extraction of spots in biological images using multiscale products. In *Pattern Recognition* 35 (9), pp. 1989–1996. DOI: 10.1016/S0031-3203(01)00127-3.

Ramírez, Omar A.; Couve, Andrés (2011): The endoplasmic reticulum and protein trafficking in dendrites and axons. In *Trends in cell biology* 21 (4), pp. 219–227. DOI: 10.1016/j.tcb.2010.12.003.

Rangaraju, Vidhya; Tom Dieck, Susanne; Schuman, Erin M. (2017): Local translation in neuronal compartments: how local is local? In *EMBO reports* 18 (5), pp. 693–711. DOI: 10.15252/embr.201744045.

Saraste, Jaakko; Marie, Michaël (2018): Intermediate compartment (IC): from pre-Golgi vacuoles to a semi-autonomous membrane system. In *Histochemistry and cell biology* 150 (5), pp. 407–430. DOI: 10.1007/s00418-018-1717-2.

Schlüter, Annabelle; Del Turco, Domenico; Deller, Thomas; Gutzmann, Annika; Schultz, Christian; Engelhardt, Maren (2017): Structural Plasticity of Synaptopodin in the Axon Initial Segment during Visual Cortex Development. In *Cerebral cortex (New York, N.Y. : 1991)* 27 (9), pp. 4662–4675. DOI: 10.1093/cercor/bhx208.

Segal, Menahem; Vlachos, Andreas; Korkotian, Eduard (2010): The spine apparatus, synaptopodin, and dendritic spine plasticity. In *The Neuroscientist : a review journal bringing neurobiology, neurology and psychiatry* 16 (2), pp. 125–131. DOI: 10.1177/1073858409355829.

Sograte-Idrissi, Shama; Schlichthaerle, Thomas; Duque-Afonso, Carlos J.; Alevra, Mihai; Strauss, Sebastian; Moser, Tobias et al. (2020): Circumvention of common labelling artefacts using secondary nanobodies. In *Nanoscale*. DOI: 10.1039/d0nr00227e.

Spacek, Josef; Harris, Kristen M. (1997): Three-Dimensional Organization of Smooth Endoplasmic Reticulum in Hippocampal CA1 Dendrites and Dendritic Spines of the Immature and Mature Rat. In *J. Neurosci.* 17 (1), pp. 190–203. DOI: 10.1523/JNEUROSCI.17-01-00190.1997.

Terenzio, Marco; Schiavo, Giampietro; Fainzilber, Mike (2017): Compartmentalized Signaling in Neurons: From Cell Biology to Neuroscience. In *Neuron* 96 (3), pp. 667–679. DOI: 10.1016/j.neuron.2017.10.015.

Tønnesen, Jan; Inavalli, V. V. G. Krishna; Nägerl, U. Valentin (2018): Super-Resolution Imaging of the Extracellular Space in Living Brain Tissue. In *Cell* 172 (5), 1108-1121.e15. DOI: 10.1016/j.cell.2018.02.007.

Toresson, Håkan; Grant, Seth G. N. (2005): Dynamic distribution of endoplasmic reticulum in hippocampal neuron dendritic spines. In *The European journal of neuroscience* 22 (7), pp. 1793–1798. DOI: 10.1111/j.1460-9568.2005.04342.x.

Truckenbrodt, Sven; Viplav, Abhiyan; Jähne, Sebastian; Vogts, Angela; Denker, Annette; Wildhagen, Hanna et al. (2018): Newly produced synaptic vesicle proteins are preferentially used in synaptic transmission. In *The EMBO journal* 37 (15). DOI: 10.15252/embj.201798044.

Vlachos, Andreas (2012): Synaptopodin and the spine apparatus organelle-regulators of different forms of synaptic plasticity? In *Annals of anatomy = Anatomischer Anzeiger : official organ of the Anatomische Gesellschaft* 194 (4), pp. 317–320. DOI: 10.1016/j.aanat.2011.10.014.

Vlachos, Andreas; Korkotian, Eduard; Schonfeld, Eldi; Copanaki, Ekaterini; Deller, Thomas; Segal, Menahem (2009): Synaptopodin regulates plasticity of dendritic spines in hippocampal neurons. In *The Journal of neuroscience : the official journal of the Society for Neuroscience* 29 (4), pp. 1017–1033. DOI: 10.1523/JNEUROSCI.5528-08.2009.

Westphal, Volker; Rizzoli, Silvio O.; Lauterbach, Marcel A.; Kamin, Dirk; Jahn, Reinhard; Hell, Stefan W. (2008): Video-rate far-field optical nanoscopy dissects synaptic vesicle movement. In *Science (New York, N.Y.)* 320 (5873), pp. 246–249. DOI: 10.1126/science.1154228.

Wilhelm, Benjamin G.; Mandad, Sunit; Truckenbrodt, Sven; Kröhnert, Katharina; Schäfer, Christina; Rammner, Burkhard et al. (2014): Composition of isolated synaptic boutons reveals the amounts of vesicle trafficking proteins. In *Science (New York, N.Y.)* 344 (6187), pp. 1023–1028. DOI: 10.1126/science.1252884.

Williams, Alex H.; O'Donnell, Cian; Sejnowski, Terrence J.; O'Leary, Timothy (2016): Dendritic trafficking faces physiologically critical speed-precision tradeoffs. In *eLife* 5. DOI: 10.7554/eLife.20556.

Willig, Katrin I.; Rizzoli, Silvio O.; Westphal, Volker; Jahn, Reinhard; Hell, Stefan W. (2006): STED microscopy reveals that synaptotagmin remains clustered after synaptic vesicle exocytosis. In *Nature* 440 (7086), pp. 935–939. DOI: 10.1038/nature04592.

Wu, Yumei; Whiteus, Christina; Xu, C. Shan; Hayworth, Kenneth J.; Weinberg, Richard J.; Hess, Harald F.; Camilli, Pietro de (2017): Contacts between the endoplasmic reticulum and other membranes in neurons. In *Proceedings of the National Academy of Sciences of the United States of America* 114 (24), E4859-E4867. DOI: 10.1073/pnas.1701078114.

Supplemental information

Supplementary Table 1: List of statistical values and number of synapses per individual experiments.

Type of analysis	Synaptic marker	POI	Synapses /bin	Total synapses	Rho	P (spearmen)
Automatic analysis of all synapses	homer	calreticulin	643	3215	0.956	0.00000000
		ERGIC53	680	3400	0.889	0.00000016
		TGN38	379-380	1899	0.925	0.00000000
		synaptopodin	542-543	2712	0.968	0.00000000
		vGLUT1	1138	5690	0.435	0.05505578
		SYT1	1156-1157	5781	0.754	0.00012247
	vGLUT1	calreticulin	487-488	2439	0.956	0.00000000
		ERGIC53	265-266	1326	0.765	0.00013235
		TGN38	117-118	588	0.876	0.00000039
		synaptopodin	159-160	796	0.833	0.00000492
	SYT1	calreticulin	249	1245	0.656	0.00168277
		ERGIC53	176-177	883	0.784	0.00004172
		TGN38	152-153	763	0.895	0.00000009
		synaptopodin	213-214	1068	0.882	0.00000025
Analysis of mushroom spines	homer	calreticulin	186	930	0.820	0.0000034
		ERGIC53	208	1040	0.901	0.0000001
		TGN38	122	610	0.860	0.0000006
		synaptopodin	140	700	0.840	0.0000016
	vGLUT1	calreticulin	99	495	0.351	0.0546565
		ERGIC53	100	500	0.583	0.0009192
		TGN38	75	375	0.781	0.0000124
		synaptopodin	79	395	0.705	0.0000665
	SYT1	calreticulin	87	435	0.026	0.5600091
		ERGIC53	107	535	0.448	0.0087806
		TGN38	47	235	0.482	0.0083918
		synaptopodin	61	305	0.687	0.0001321
	head size	calreticulin size	182-183	914	0.550	0.001554104
		ERGIC53 size	209-210	1047	0.761	0.00002167
		TGN38 size	131-132	657	0.001	0.90780719
		synaptopodin size	139-140	696	0.820	0.00000339
		calreticulin number	182-183	914	0.705	0.000008845
		ERGIC53 number	209-210	1047	0.901	0.00000006
		TGN38 number	131-132	657	0.653	0.0002669
		synaptopodin number	139-140	696	0.964	0.0000000
Analysis of stubby spines	homer	calreticulin	61	305	0.820	0.0000034
		ERGIC53	81	405	0.651	0.0002730
		TGN38	51	255	0.502	0.0030688
		synaptopodin	53	265	0.860	0.0000006
	vGLUT1	calreticulin	24	120	0.193	0.1757708
		ERGIC53	46	230	0.687	0.0001321
		TGN38	36	180	0.820	0.0000034
		synaptopodin	31	155	0.260	0.0620052
	SYT1	calreticulin	37	185	0.129	0.1874141
		ERGIC53	34	170	0.316	0.0363651
		TGN38	15	75	0.396	0.0378569
		synaptopodin	22	110	0.193	0.1325609

Supplementary Table 1 continued: List of statistical values and number of synapses per individual experiments.

Type of analysis	Synaptic marker	POI	Synapses /bin	Total synapses	Rho	P (spearmen)
Automatic analysis of all synapses - Radial redistribution	homer	calreticulin	643	3215	0.899	0.03738607
		ERGIC53	680	3400	0.899	0.03738607
		TGN38	379-380	1899	0.300	0.62383766
		synaptopodin	542-543	2712	0.999	0.00000000
	vGLUT1	calreticulin	487-488	2439	0.899	0.03738607
		ERGIC53	265-266	1326	0.499	0.39100221
		TGN38	117-118	588	0.199	0.74706007
		synaptopodin	159-160	796	0.999	0.00000000
	SYT1	calreticulin	249	1245	0.999	0.00000000
		ERGIC53	176-177	883	0.999	0.00000000
		TGN38	152-153	763	0.899	0.03738607
		synaptopodin	213-214	1068	0.999	0.00000000

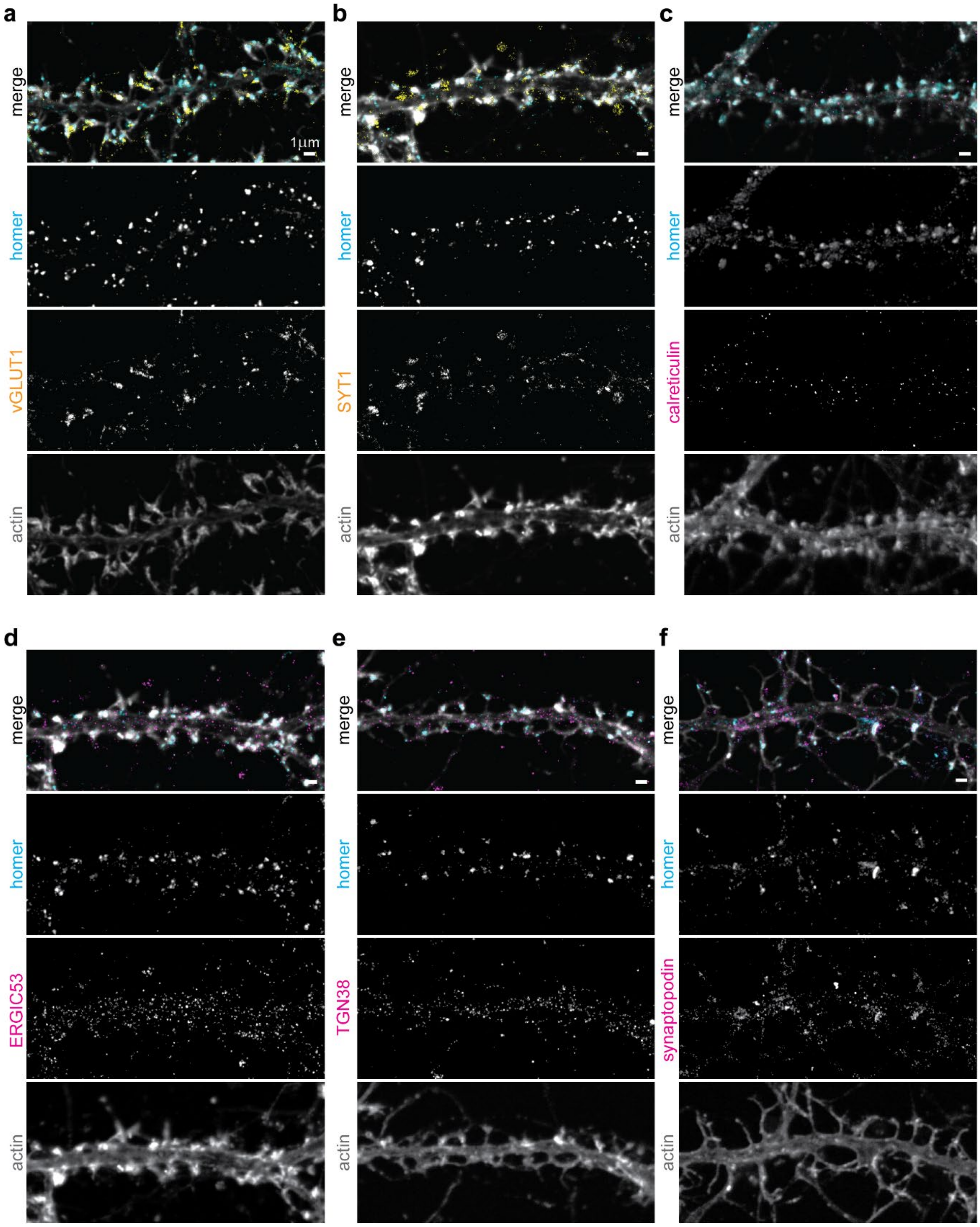

Supplementary Figure 1. Representative images of vGLUT1 and SYT1 compared to homer, and of the POIs stainings
Representative STED images of dendrites in mature hippocampal neuronal cultures. Samples were all stained with homer, phalloidin (actin, confocal), with pre- and post-synaptic sites markers vGLUT1 **(a)** or SYT1 **(b)**, and for the proteins of interest: calreticulin **(c)**, ERGIC53 (same dendrite as shown in b) **(d)**, TGN38 **(e)**, and synaptopodin **(f)**. Scale bars: 1 μm.

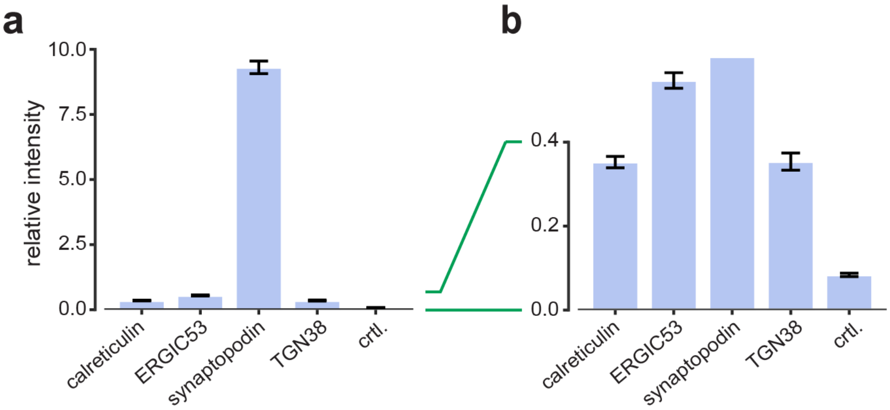

Supplementary Figure 2. Comparison of average intensities of the individual POIs

Average staining intensity of the different POIs and control samples in which the primary antibody was omitted. Comparison of all stainings (**a**) and close up on the lower intensities (**b**). All data was collected from 3 independent experiments. Whiskers represent S.E.M.

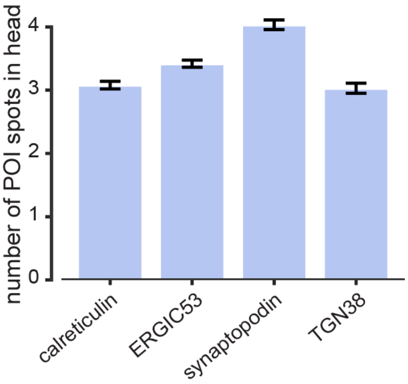

Supplementary Figure 3. Average spot number of secretory elements in mushroom spines

Average numbers of spots of calreticulin, ERGIC53, TGN38, and synaptopodin inside the spine head after manual segmentation. All data was collected from 3 independent experiments. Whiskers represent S.E.M.

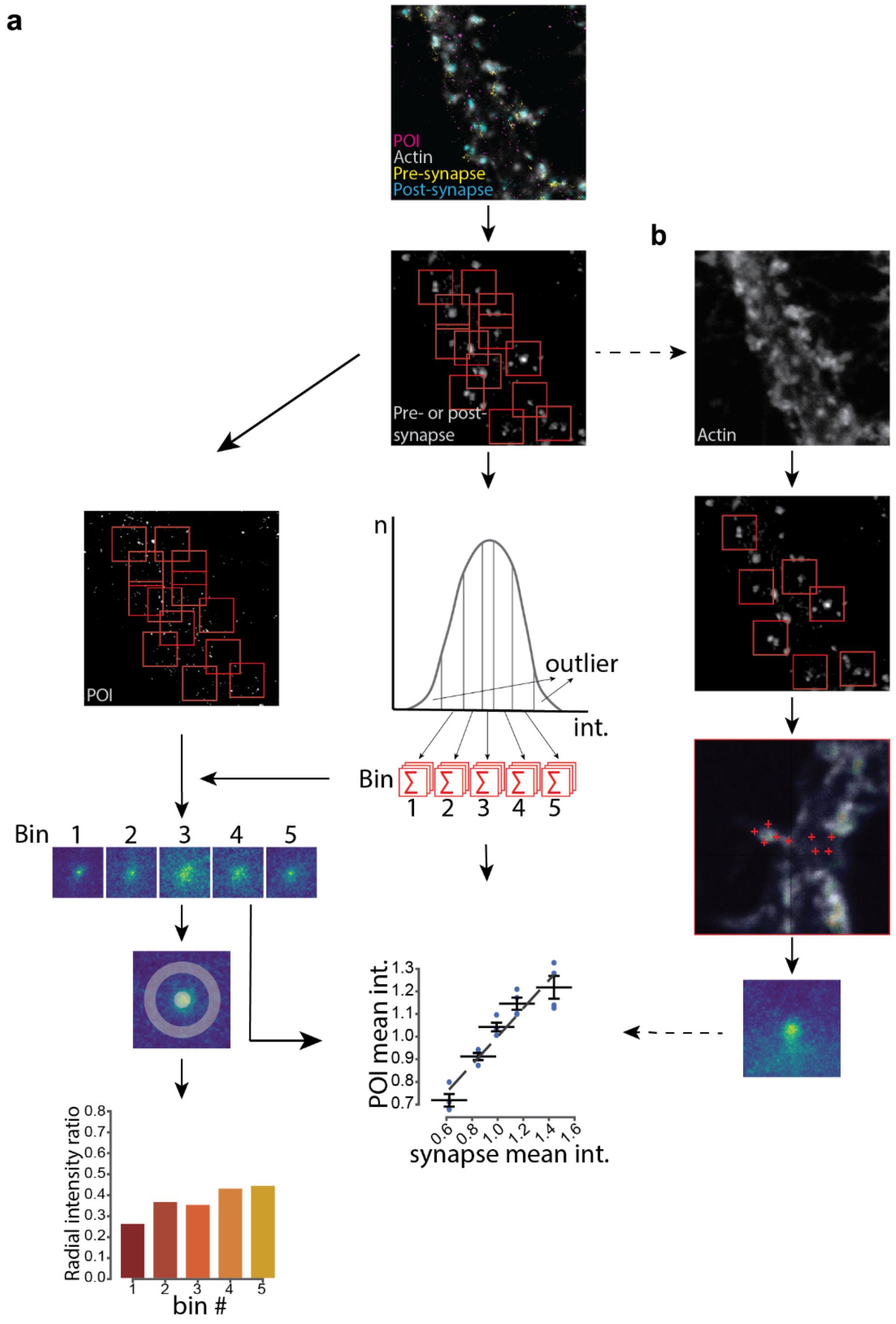

Supplementary Figure 4. Image analysis workflow

4-colour images were acquired of the protein of interest (magenta), actin (white) and pre- and post-synaptic markers (yellow and cyan respectively). (a) Automatic analysis: the pre-/post-synaptic markers were used to identify synaptic puncta in the images. 3 x 3 µm square regions were extracted for each synapse and pooled into five bins based on increasing fluorescence intensity of the synaptic markers. The POI images were averaged for each bin and correlated to the average intensity of the synaptic markers. Alternatively, a ratio was calculated between the outer rim and the central area of each average image to determine the tendency of the POI to localize to the synapse proximity. (b) Manual analysis: the post-synaptic marker was used to locate dendritic spines and extract 3 x 3 µm square regions as in (a). The actin channel of the images was then used to manually determine the borders of the spines in order to align them to a similar orientation before subsequent analysis.

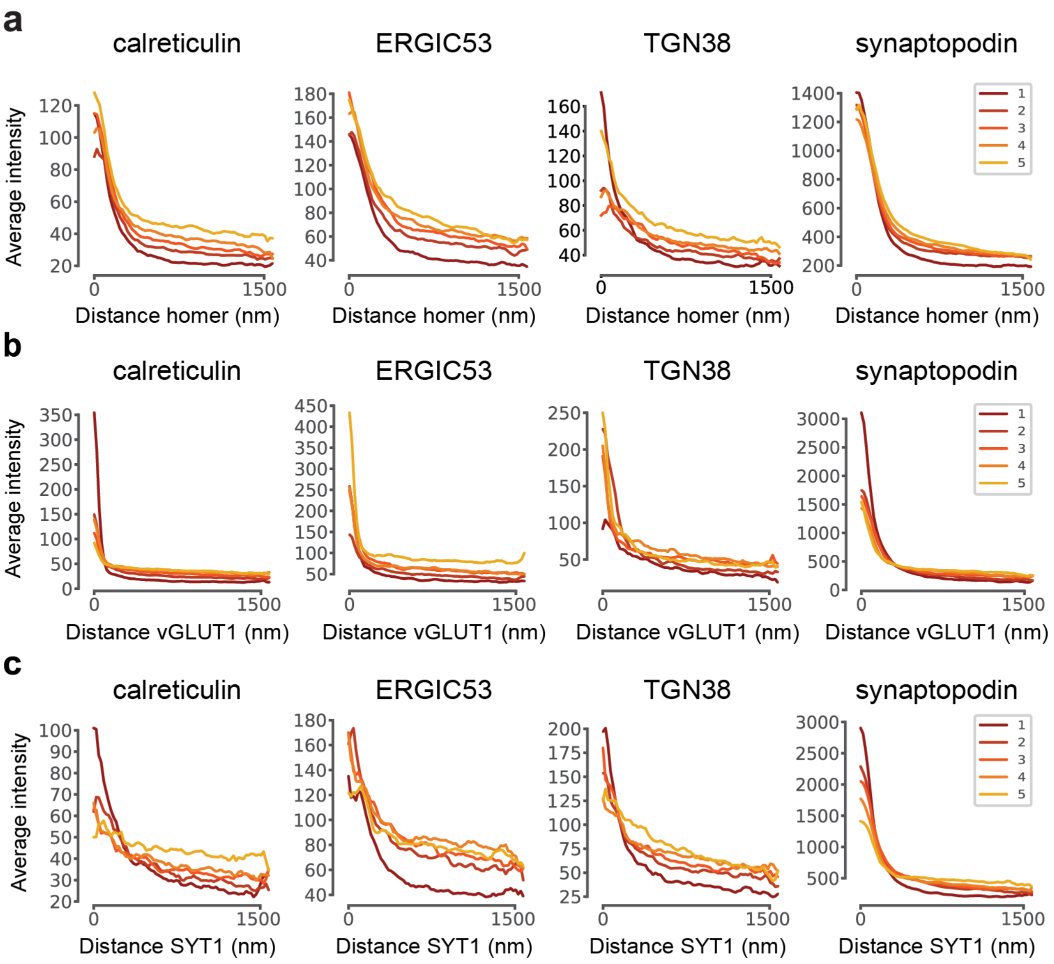

Supplementary Figure 5. Radial profile plots of the average intensity images

Radial profiles for bins of each POI: homer (**a**), vGLUT1 (**b**), and SYT1 (**c**). Bins 1-5 (dark red-yellow) were used for calculating the ratios depicted in Fig. 2b, 3b, and 4b, respectively.

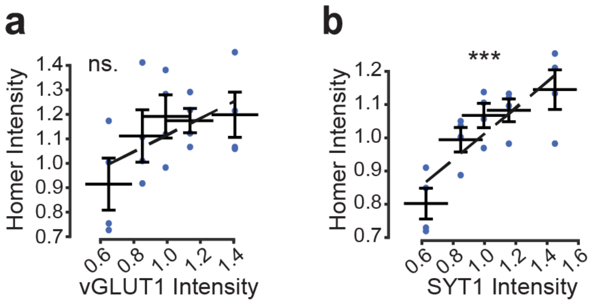

Supplementary Figure 6. Intensity correlations of pre-and post-synaptic markers

Correlation of homer intensities and the average intensities of vGLUT1 (**a**) and SYT1 (**b**). Dashed lines are the linear fits. All data was collected from four independent experiments. Where *=p<0.05, **=p<0.01, ***=p<0.001, ****=p<0.0001, and ns.=non-significant. Whiskers represent S.E.M. Numbers of synapses per each bin and Spearman's rho are listed in Supplementary Table 1.

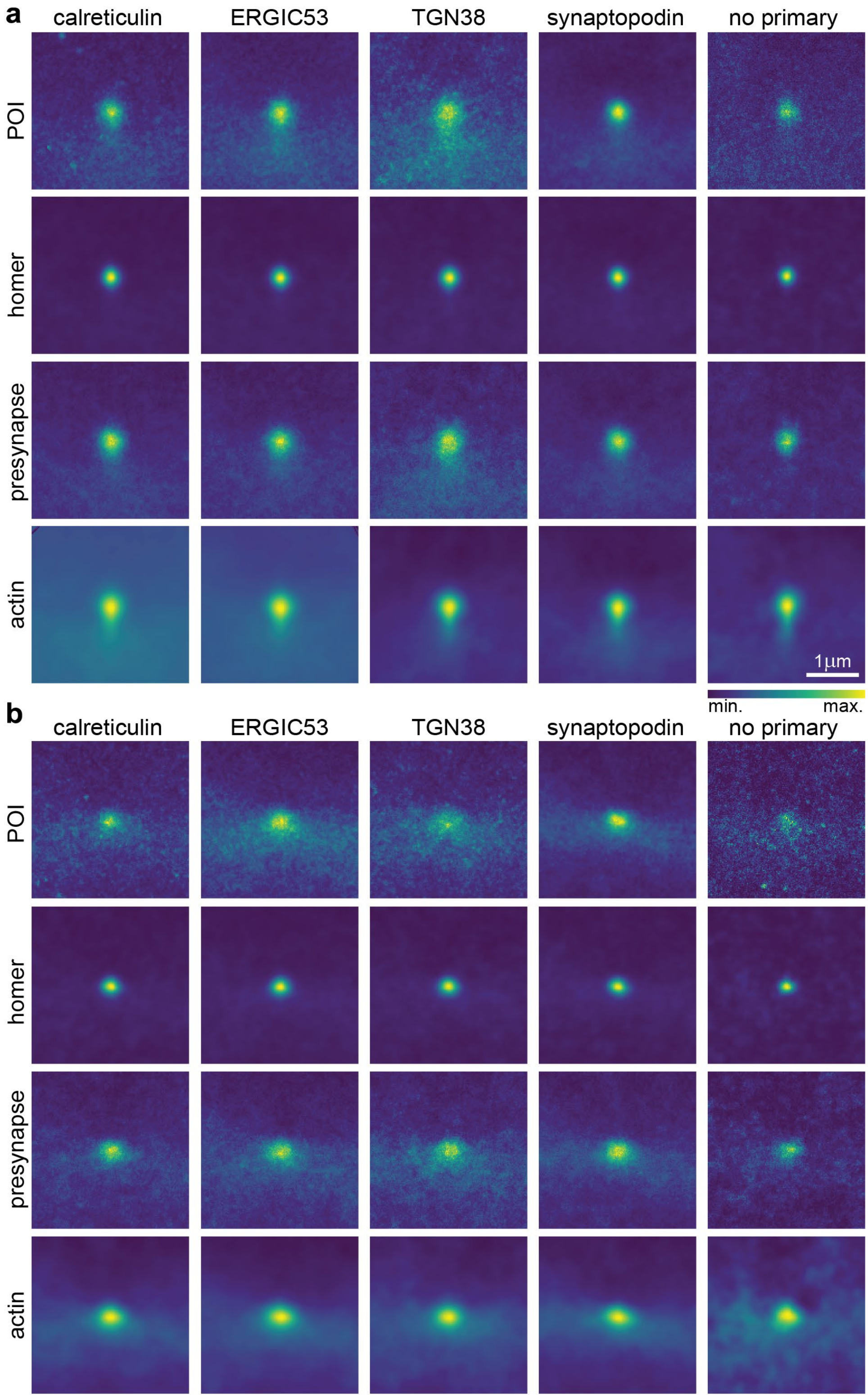

Supplementary Figure 7. Average images of spines after manual segmentation

Average images of mushroom **(a)** and stubby **(b)** spines of the POIs, homer, average pre-synaptic markers vGLUT1 and SYT1, and phalloidin. Intensities have been adjusted for each image. Average images of the POIs shown in panel (a) are the same average images depicted in Fig. 5a.

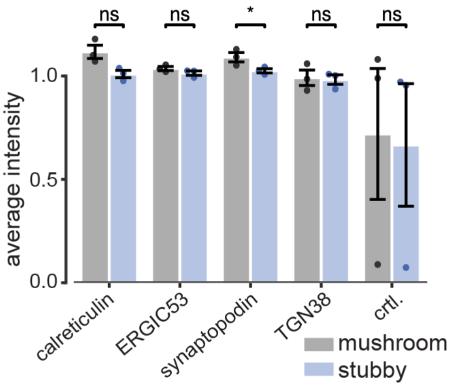

Supplementary Figure 8. Comparison of average intensities of mushroom and stubby spines
Average staining intensities of POI normalised to experimental means. Whiskers represent S.E.M.

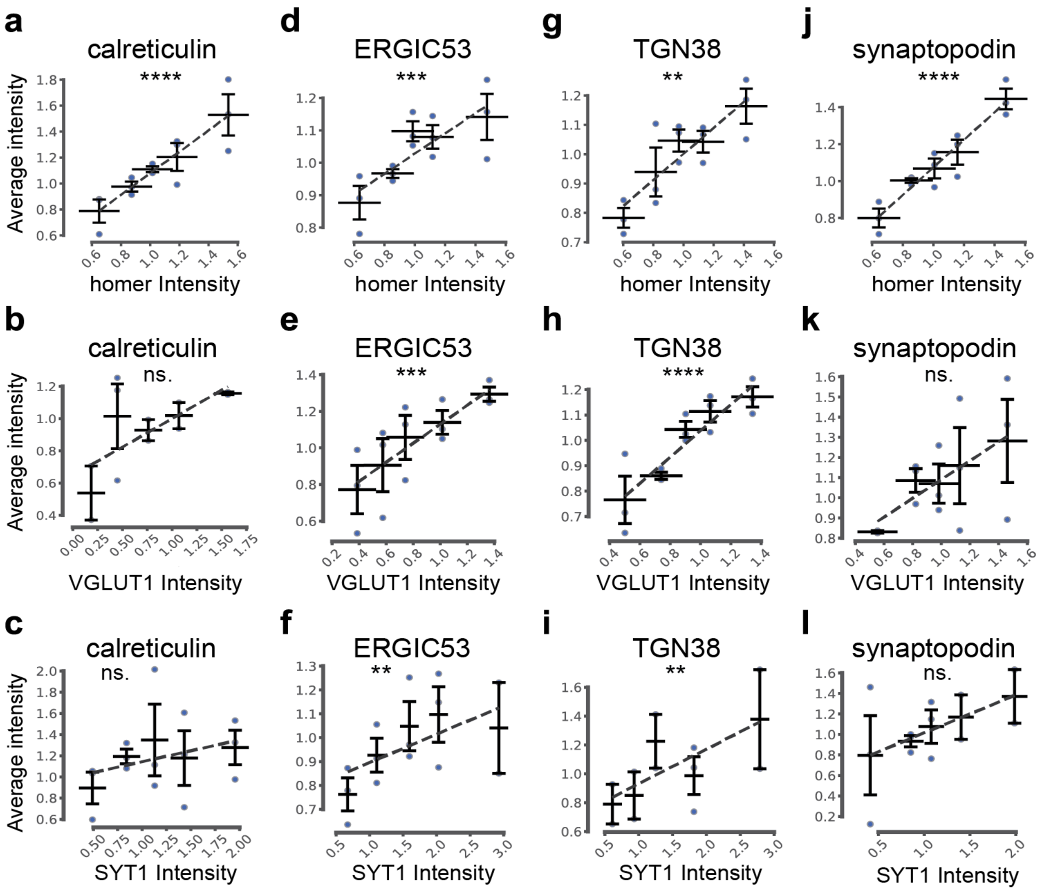

Supplementary Figure 9. Correlations of secretory elements at stubby spines
(a-l) Average intensity correlations after manual spine segmentation and classification of stubby type spines. Average intensities of calreticulin (a-c), ERGIC53 (d-f), TGN38 (g-i), and synaptopodin (j-l) correlated with average intensities of homer (a,d,g,j), vGLUT1 (d,e,h,k), and SYT1 (c,f,i,l). Dashed lines are linear fits. All data were collected from three independent experiments. Where *=p<0.05, **=p<0.01, ***=p<0.001, ****=p<0.0001, and ns.=non-significant. Whiskers represent S.E.M. Numbers of synapses per each bin and Spearman's rho are listed in Supplementary Table 1.

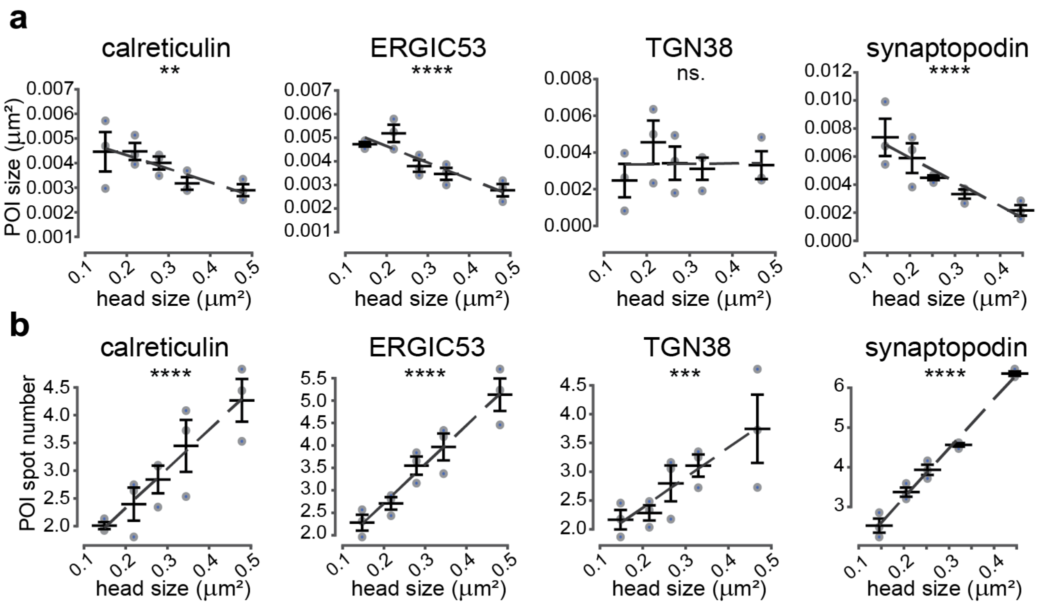

Supplementary Figure 10. Correlations of POI spot size and numbers and synaptic size in mushroom spines

(a) Correlation between average protein spot size of calreticulin, ERGIC53, TGN38, and synaptopodin inside the spine head and head size, as defined by manual segmentation. **(b)** Correlation between average spot numbers of calreticulin, ERGIC53, TGN38, and synaptopodin inside the spine head correlated to the head size as defined by manual segmentation. Dashed lines are linear fits. Where *=p<0.05, **=p<0.01, ***=p<0.001, and ****=p<0.0001. Whiskers represent S.E.M. Numbers of synapses per each bin and Spearman's rho are listed in Supplementary Table 1.

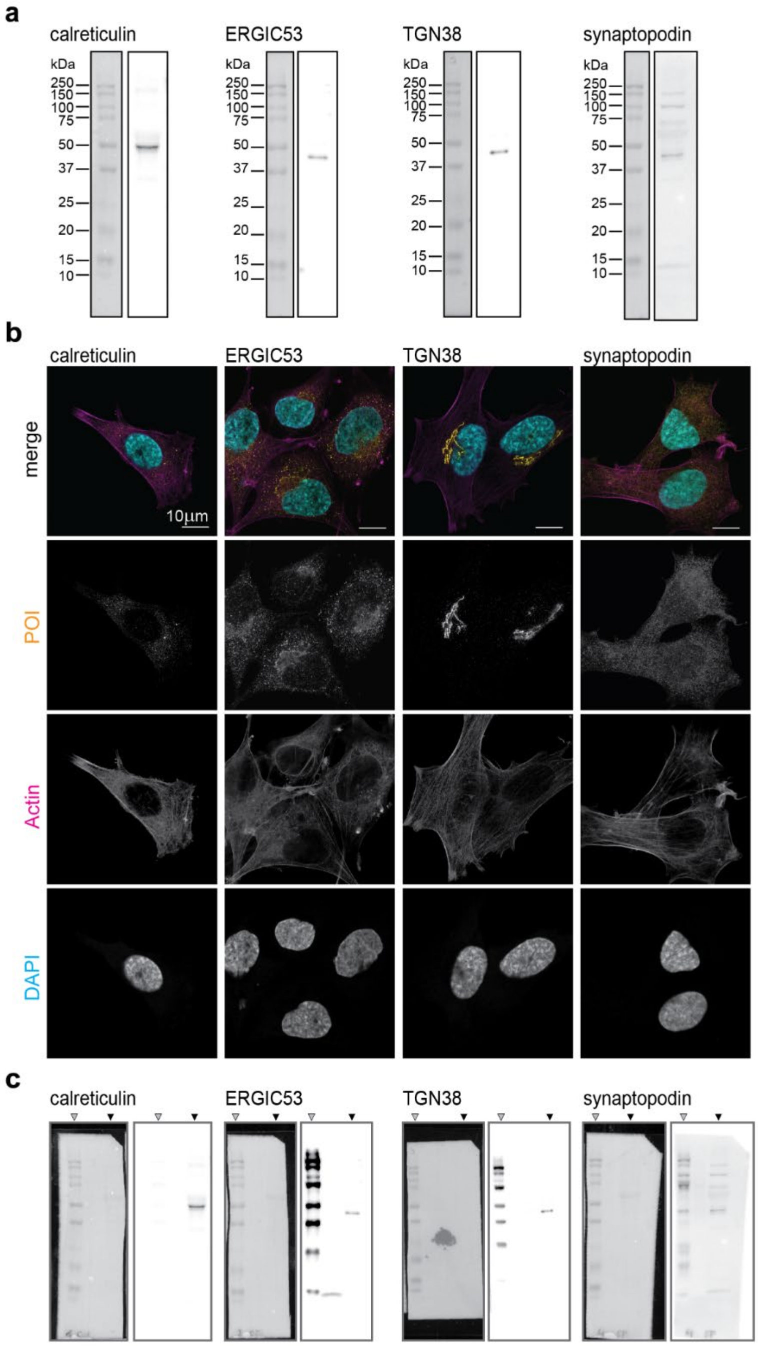

Supplementary Figure 11. Antibody validation

(a) Western blot validation of used POI antibodies in whole cell lysate of PC12 cells (calreticulin, ERGIC53 and synaptopodin) or rat cultured primary cortical neurons (TGN38). Displayed are colourimetric images of the protein ladder (left) and the respective antibody chemilumenescence signal (right) of each individual full-length membrane. Proteins have been blotted and analysed on separate membranes. Brightness and contrast have not been modified and are displayed as raw data. Full colourimetric and chemiluminescence images of the membranes are shown in panel (c). **(b)** Representative STED images of immunofluorescence in PC12 cells labelled with DAPI (confocal), phalloidin (actin), and the proteins of interest: calreticulin, ERGIC53, TGN38, and synaptopodin. Scale bars: 10 µm. **(c)** Full size membrane images used for panel (a). Left: colourimetric; right: chemilumenescence. Grey arrows indicate the position of the protein ladder; black arrows indicate the lane of the respective cell lysate, as shown in (a). The protein ladder shows aspecific chemilumenescence signal in the case of ERGIC53, TGN38 and synaptopodin. Brightness and contrast have not been modified.

Supplementary methods

Sample preparation and imaging of PC12 cells

PC12 adh cells (AddexBio, cat. C0032002) were cultured on glass coverslips and processed as described in the main text. Actin was labelled with phalloidin-Star635P (Abberior, cat. 2-0205-002-5; 1:100 dilution) and nucleus with DAPI (Biomol, cat. AG-CR1-3668-M005, 1:5000 dilution). Imaging was performed as previously described.

Western blot

Whole cell lysate from PC12 adh cells or cultured cortical primary neurons (18 days *in vitro*, prepared as hippocampal cultures), in Laemmli buffer (Bio-Rad, cat. 161-0747) were loaded in a 12% SDS gel (Bio-Rad, cat. 4561045) and subjected to electrophoresis at 50 V for 5 min, followed by 10 V for 80 min. Separated proteins were then transferred onto a PVDF membrane (Bio-Rad, cat. 162-0260) at 120 V for 50 min. The blotted membranes were blocked in Tris-buffered saline, 0.1% Tween (TBST), 3% BSA and incubated overnight with previously described primary antibodies (calreticulin 1:500, ERGIC53 1:1000, TGN38 1:500, synaptopodin 1:1000) in TBST, 1% BSA. Then the membranes were washed five times in TBST and incubated with secondary antibody dilution (Thermo Fisher, cat. 31466, 1:10000) in TBST 1% BSA for 1 hour at room temperature. Afterwards membranes were washed five times in TBST, incubated for 1 min with ECL western blotting substrate (Thermo Fisher, cat. 32109) and signal was detected in a Chemidoc System (Bio-Rad Laboratories GmbH, Germany).

Chapter 3 – Neurofilaments at the Postsynapse

Neurofilaments are linked to several psychiatric disorders but their function and regulation at synapses is just starting to emerge. This study aims at identifying a functional link between the presence of neurofilaments in the spines and the synaptic status. To this aim, I systematically quantify different neurofilament isoforms at the postsynapse by means of multi-colour STED and confocal microscopy. I focus on the differential distribution of individual isoforms and their connection to markers of synaptic strength and activity.

Within this study I performed all sample preparation, imaging experiments, and preliminary western blot experiments. I manually segmented postsynapses in STED images and contributed to the data processing. I prepared the figures and wrote the manuscript with the contribution of the other authors.

This manuscript was prepared for publication:

- First authorship
- Submission: July 2022

Presynaptic activity and postsynaptic strength differentially regulate neurofilaments in dendritic spines

Clara-Marie Gürth[1,2], Maria Augusta do Rego Barros Fernandes Lima[1], Victor Macarrón Palacios[1,2], Angel Rafael Cereceda Delgado[1,2], Jasmine Hubrich[1], Elisa D'Este[3]

[1] Department of Optical Nanoscopy, Max-Planck-Institute for Medical Research, Heidelberg, Germany

[2] Department of NanoBiophotonics, Max-Planck-Institute for Multidisciplinary Sciences, Göttingen, Germany

[3] Optical Microscopy Facility, Max-Planck-Institute for Medical Research, Heidelberg, Germany

Abstract

Neurofilaments are one of the main cytoskeletal components in neurons and they can be found in the form of oligomers at pre- and postsynapses. How their presence is regulated at the postsynapse remains widely unclear. Here we systematically quantified by immunolabeling the occurrence of the neurofilament isoform triplet neurofilament light (NFL), medium (NFM), and heavy (NFH) at the postsynapse with STED nanoscopy together with markers of synaptic strength and activity. Our data shows that neurofilament isoforms rarely colocalize with each other and that they are present to different extents within dendritic spines, with NFL being the most abundant isoform. The amount of the three isoforms correlated with markers of postsynaptic strength and presynaptic activity to varying degrees. While NFL showed moderate correlation to both synaptic traits suggesting its involvement in synaptic response, NFH and NFM were only correlated on a low level. By quantifying the presence of neurofilaments at the postsynapse within the context of the synaptic status, this work sheds new light on the regulation of synaptic neurofilaments and their possible contribution to psychiatric disorders.

Introduction

Neurofilaments (NFs) are among the main components of the cytoskeleton in neurons. They are heteropolymers of NF-light (NFL), NF-medium (NFM), and NF-heavy (NFH), and can further incorporate into their backbone either α-internexin or peripherin in the central or peripheral nervous system, respectively (Leermakers and Zhulina 2010). NFM and NFH have long tails enriched in phosphorylation sites that protrude into the periphery of the filament (for reviews see Yuan et al. 2012, 2017; Bomont 2021). Variability in the subunit stoichiometry and the dynamic phosphorylation landscape indicate NFs have a high potential for being finely regulated (Nixon 1993). Indeed, these features are differentially modulated based on the cell type, developmental stage, and subcellular compartment (for reviews see Yuan et al. 2012, 2017).

Although NFs are associated with several neurological disorders (Yuan and Nixon 2016; Yuan et al. 2017; Bomont 2021; Didonna and Opal 2019; Yuan and Nixon 2021), for long time, NFs have been considered as mere space-fillers in the axon. However, in the last years a link between NF function in synapses and psychiatric disorders started to emerge (Yuan and Nixon 2016; Kilinc 2018; Bucher et al. 2020). Indeed, NF were identified at pre- and postsynaptic sites of excitatory and inhibitory synapses where they have a different phosphorylation status compared to the overall NF population (Yuan et al. 2015b; Bragina and Conti 2018; Suzuki et al. 2018). Interestingly, all subunits appear more concentrated in the postsynaptic compartment than at the presynapse. Inhibition of NFH was shown to depress long-term potentiation (LTP) in the hippocampus without altering the spines morphology, which, on the other hand, is affected in NFL knockout animals (Yuan et al. 2015b; Yuan et al. 2018). Furthermore, NFM functionally interacts with dopamine D1-receptors, while both NFL and α-internexin regulate the localization of N-methyl-D-aspartate (NMDA) receptors subunits, providing direct evidence for the involvement of NF in the regulation of synaptic functions (Ehlers et al. 1998; Kim et al. 2002; Karpova et al. 2013; Yuan et al. 2015b; Yuan et al. 2018). However, whether and how the NF composition of a spine correlates with the synaptic status, and in particular the presynaptic activity and the postsynaptic strength, is unclear. Answering this question would reveal whether NF play a role in the short-term response to synaptic activity or rather in the structural rearrangements occurring during LTP.

To clarify the involvement of NFs in postsynaptic activities, we used quantitative multicolor super resolution stimulated emission depletion (STED) microscopy of the NF triplet NFL, NFM, or NFH in combination with proxies of either postsynaptic strength (homer) or of presynaptic activity synaptotagmin-1 (Syt1) live-cell uptake (Willig et al. 2006; Gürth et al. 2020) on cultured hippocampal neurons. We found that NFL is the most abundant isoform in dendritic spines. Overall the amounts of NF isoforms correlated with both homer and Syt1 signal to varying extent with NFL showing the highest and NFM the lowest correlation, suggesting that its occurrence is influenced by the postsynaptic strength and activity.

Methods

Preparation of neuronal cultures

All procedures were performed in accordance with the German Animal Welfare Act (Tierschutzgesetz der Bundesrepublik Deutschland, TierSchG) and the Animal Welfare Laboratory Animal Ordinate (Tierschutzversuchstierverordnung) and no specific authorization or notification was required. The sacrificing of P0–P2 rats was supervised by animal welfare officers of the Max Planck Institute for Medical Research (MPImF) and conducted and documented according to the guidelines of the TierSchG (permit number assigned by the MPImF: MPI/T-35/18).

Primary hippocampal or cortical neuronal cultures were prepared from dissociated tissue of P0-P2 postnatal wild-type Wistar rats of either sex (Janvier-Labs) as described previously in (Gürth et al. 2020). Briefly, dissected hippocampal tissue was digested with 0.25% trypsin for 20 minutes at 37°C and dissociated and maintained in Neurobasal supplemented with 2% B27, 1% GlutaMAX and 1% penicillin/streptomycin (all from Gibco, Thermo Fisher Scientific). Cells were seeded at a concentration of 110,000/well in 12-well plates on Ø 18mm glass coverslips coated with 0.1 mg/ml poly-ornithine (Sigma-Aldrich) and 1 μg/ml laminin (Corning). Medium was changed to fresh supplemented Neurobasal 1-2 hours after seeding and cultures were maintained in an incubator (37°C, 5%CO_2) until day *in vitro* (DIV) 15-25 without inhibition of glial cell growth by AraC.

Sample preparation and immunostaining

Cultured neurons were transduced at DIV 7 for volume labeling with AAV-hSyn-EGFP, which was a gift from Bryan Roth (Addgene #50465). The preparation of adeno-associated viral vectors was performed as previously described in (Masch et al. 2018) and purified as described in (Zolotukhin et al. 2002). Turnover of synaptic vesicles in mature cultures (DIV 15-25) was determined by live labeling with Atto647N-labeled mouse antibody against the luminal domain of synaptotagmin 1 (Synaptic Systems, cat. 105 311AT1, 1:500 in culture medium) for 1 hour. Samples were afterwards washed three times in prewarmed ACSF before fixing (126 mM NaCl, 2.5 mM KCl, 2.5 mM$CaCl_2$, 1.3 mM $MgCl_2$, with 30 mM Glucose, 27 mM HEPES).

Prior to immunolabeling mature (DIV15-25) cultures were fixed in 4% PFA in PBS, pH 7.4, quenched with quenching buffer (PBS, 100 mM glycine, 100 mM ammonium chloride), permeabilized for 5 min in 0.1% Triton X-100 in PBS and blocked with 1% BSA in PBS for 1 hour. Samples were then incubated for 1 hour at room temperature with primary antibodies, secondary antibodies and phalloidin in PBS, each followed by five washes in PBS.

Primary antibodies used were: homer1 guinea pig (Synaptic Systems, cat. 160 004, 1:500 dilution), neurofilament-L rabbit (Synaptic Systems, cat. 171 002, 1:200 dilution), neurofilament-L chicken (Synaptic Systems, cat.171 006, 1:200 dilution), neurofilament-M rabbit (Synaptic Systems, cat. 171 203, 1:200 dilution), neurofilament-M mouse (Synaptic Systems, cat. 171 211, 1:200 dilution), neurofilament-H rabbit (Synaptic Systems, cat. 171 102, 1:200 dilution), neurofilament-H mouse (Synaptic Systems, cat. 171 111, 1:200 dilution). Note that antibodies against the same neurofilament isoform were raised against the same epitope on the proteins. Secondary antibodies, nanobodies, and dyes used were: Star635P anti-guinea pig (Abberior, cat. 2-0112-007-1, 1:100 dilution) and Alexa Fluor 594 anti-rabbit (Thermo Fisher, cat. A-21207, 1:100 dilution), Alexa Fluor 488 anti-chicken (Thermo Fisher, cat. A-21467, 1:100 dilution), Star635P anti-mouse (IgG2) (NanoTag, cat. N2702-Ab635P-S, 1:200 dilution), Star580 anti-mouse (IgG1) (NanoTag, cat. N2002-Ab580-S, 1:200 dilution), Phalloidin Alexa Fluor 405 (Thermo Fisher, cat. A30104; 1:200 dilution). Samples were afterwards embedded in Mowiol® supplemented with DABCO and cured for at least 1 hour at room temperature before imaging.

Confocal and STED Imaging

Samples were imaged on an Abberior Expert Line Microscope (Abberior Instruments GmbH) on a motorized inverted microscope IX83 (Olympus) and equipped with pulsed STED lines at 775 nm and 595 nm, excitation lasers at 355 nm, 405 nm, 485 nm, 561 nm, and 640 nm, and spectral detection. Spectral detection was performed with avalanche photodiodes (APD) and detection windows were set to 650-725 nm, 600-630 nm, 505-540 nm, and 420-475 nm to detect Atto647N/Star635P, Alexa Fluor 594/Star580, Alexa Fluor 488/EGFP and Alexa Fluor 405, respectively. Images were acquired either with a 20x/0.4 NA oil immersion lens with pixel size of 100 nm or with a 100x/1.4 NA oil immersion lens, 30 nm pixel size, and pinhole to 100 µm (1 A.U.). Laser powers and dwell times were kept consistent during the entire experiments.

Image processing and analysis

Images shown in figures were visualized and processed with Imspector (Abberior Instruments GmbH), FIJI (*https://fiji.sc* version 1.53f51, (Schindelin et al. 2012) and MATLAB 2021b (MathWorks). Images are shown as smoothed data with a low pass Gaussian filter and 1-5% background subtraction. Brightness was adjusted uniformly throughout the images. Manual segmentation of spines was performed in FIJI, based on either the EGFP volume labeling (for single NF analyses) or on phalloidin labeling (for colocalization analysis). In addition to the spine segmentation, a second mask was generated for each raw image by applying an automatic Otsu’s threshold to STED images of synaptic markers or a 4-counts background threshold for STED images of NFs.

Each image was then masked with the intersection between the defined spine regions and its respective second mask. Afterwards, for each region of interest (ROI), the area and the intensity of the enclosing pixels were computed. The amount was defined as the area times the mean intensity.

For comparing amounts of NF and synaptic markers, we used the standardized data sorted by experimental round. The standardization was computed as $z = \frac{x-\mu}{\sigma}$, where x is the input data point, μ is the group mean and σ the group standard deviation. The Spearman's correlation coefficient was then calculated for each NF isoform versus the synaptic marker, after grouping all the corresponding standardized experimental rounds. Spearman's correlation coefficients were interpreted as suggested in Mukaka 2012.

Colocalization was performed using a custom code written in MATLAB. For analysis on the cellular level, NF signal of entire field of view was segmented from the background with a binary mask. The mask was generated after saturating 90% of the original confocal image, followed by an 8-pixel median filtering, to remove noisy pixels, and by a global Otsu's threshold. On the spine level, we used the masks generated from the manual segmentation of STED images described above. Thereafter, the respective masks were applied to the original images and the Pearson's correlation coefficient for non-zero pixels was computed for each pair of NF isoforms, to characterize their degree of colocalization.

Results

NF isoforms poorly co-localize at the post synapse

NFs are known to be a major structural component in the axon but have been shown to be present also in the dendritic shaft and at the synapse. Therefore, we first characterized the cellular distribution of the NF isoforms NFL, NFM, and NFH within hippocampal neurons using confocal microscopy. All three NF isoforms strongly labeled primary hippocampal cultured neurons (**Fig. 1A and S1**).

Signals of all NF isoforms were more prominent in axons then in dendrites. Interestingly, strong differences in the signal intensity of each of the different isoforms were observed. NFL signal was more strongly dispersed throughout dendritic regions and showed less characteristic filamentous organization within dendrites than the other isoforms (**Fig. S1B**). Colocalization analyses showed that signals from the three different NF isoforms only correlated approximately 20-30% compared with the control experiments, in which the same isoform (NFM) was labeled with multiple fluorophores to compensate for chromatic artefacts (**Fig. 1B and S1D**). Together with our western blot analysis (**Fig. S2**), this data confirms that the chosen antibodies are capable of detecting different isoforms and protein distribution, and suggests that different neuronal regions possess different NF expression patterns.

Next, we focused on dendritic spines, to assess the role of NF isoforms at the postsynapse. To this aim, we performed dual-color STED imaging in neuronal cultures together with phalloidin, to visualize the spine morphology. Distinct, non-colocalizing puncta were observed in the spines when co-labeling NFM and NFL or NFH and NFM (**Fig. 1D**). We further quantified this evidence by performing a colocalization analysis specifically at manually segmented dendritic spines in dual-color STED images (**Fig. 1C**). We observed only a low degree (20-30%) of colocalization at the postsynapse for both NFL-NFM and NFM-NFH compared to the control (75 %) with only one isoform (NFM) labeled with both fluorophores. This shows the sensitivity and specificity of our model system and that, although signal of all NF isoforms is present at most postsynapses, this signal rarely colocalizes.

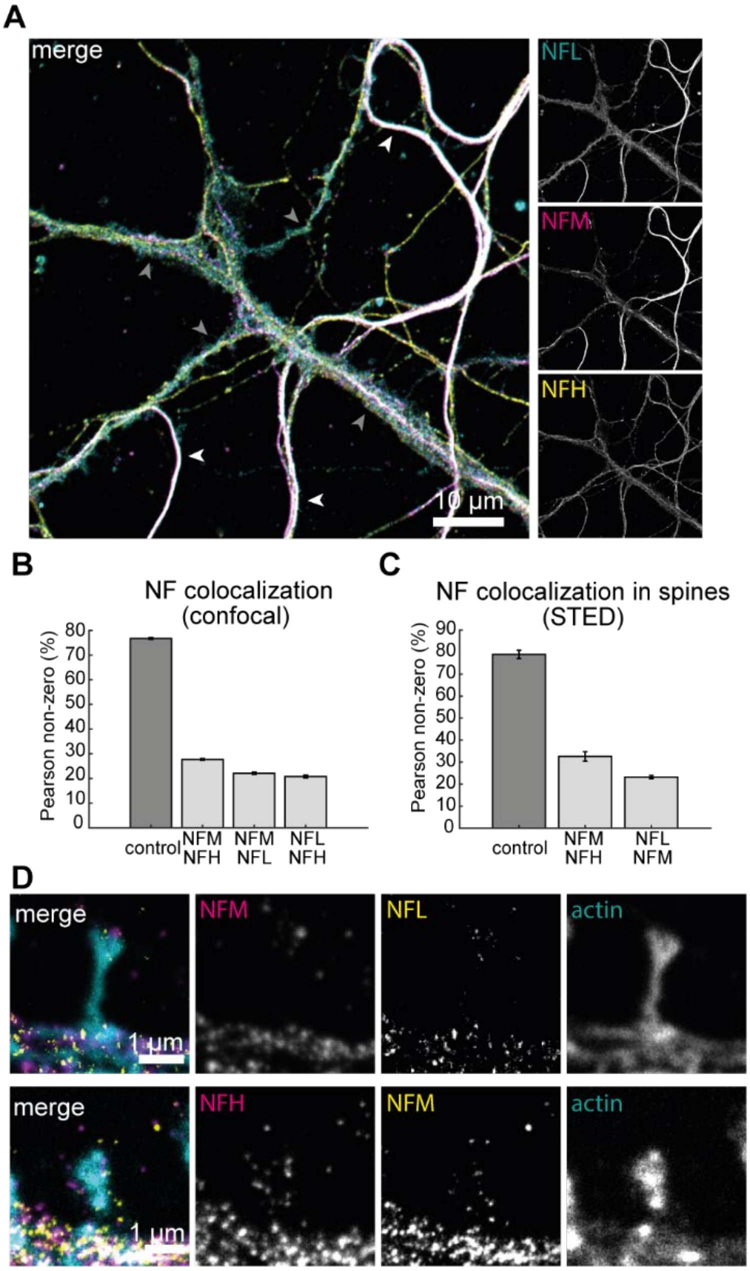

Figure 1. NF isoforms in hippocampal neurons

(A) Confocal images of the different NF isoforms NFL (cyan), NFM (magenta) and NFH (yellow) in primary hippocampal neurons. White arrowheads indicate axonal NF signal and grey arrowheads indicate dendritic NF signal. Scale bar is 10 µm. (B) colocalization analysis of NFL, NFM, and NFH on cellular level in confocal images as shown in (A) compared to control images with same isoform (NFM) labeled in all fluorescent channels. Shown is the mean values of Pearson's correlation coefficient of all pixels with non-zero intensities. Error bars show the standard deviation of the mean (SEM). Data calculated from 21 different field of views. (C) Colocalization analysis of NFL, NFM, and NFH on the synaptic level in STED images as shown in (D) compared to control images with same isoform (NFM) labeled in both STED channels. Shown is the mean of the Pearson's correlation coefficient of all pixels with non-zero intensities. Error bars shows its respective SEM. Data calculated from a total of 534 manually segmented spines from 3-5 different cells per condition. (D) Representative images of dendritic spines labeled with two NF isoforms (magenta/yellow) and actin (cyan). Scale bar is 1 µm.

NFL is the most represented isoform in dendritic spines

To further characterize the presence of NFs at the postsynapse, we next performed comparative STED imaging of either NFL, NFH or NFM. To minimize the variability of the experiments, we chose primary antibodies raised in rabbit for all isoforms, so that the same secondary antibody could be used for all experiments. The epitopes recognized by these antibodies, which were validated by western blot (**Fig. S2**), are the same as the antibodies used for the colocalization experiments shown in **Fig. 1**. Both sets of reagents displayed similar labeling patterns of filamentous structures in the axons and puncta in dendritic spines (**Fig. 2A**). Thereby the overall signal intensity was comparable between the different isoforms and higher than control signal obtained by the omission of the primary antibody (**Fig. S3**). The granule-like NF signals in spines were geometrically distinct from the filamentous signals obtained from axonal NFs.

Next the presence of NFs inside dendritic spines was quantified. For this the intensity and area of NF signal inside the manually segmented spines, as identified by GFP volume labeling was analyzed. We observed NF signal of all three isoforms in the majority of spines albeit to varying extents (**Fig. 2B**). The cumulative distribution of NF area within individual spines showed that the area covered by NFL signal is larger than the area covered by NFM and NFL. Control images with only secondary antibody labeling showed an overall very low background signal compared to NF signal. Based on the cumulative distribution we tested the presence of NF signal area with a threshold of $0.1\mu m^2$. We observed that around 70% of spines contained more than $0.1\mu m^2$ NFL signal per spine whereas for the same area was displayed in only 55% of spines for NFM and only around 30% for NFH (**Fig. 2C**). This demonstrates that NF isoforms are present at the postsynapse to varying extents and suggests a distinct role of NFL and NFM or NFH within dendritic spines.

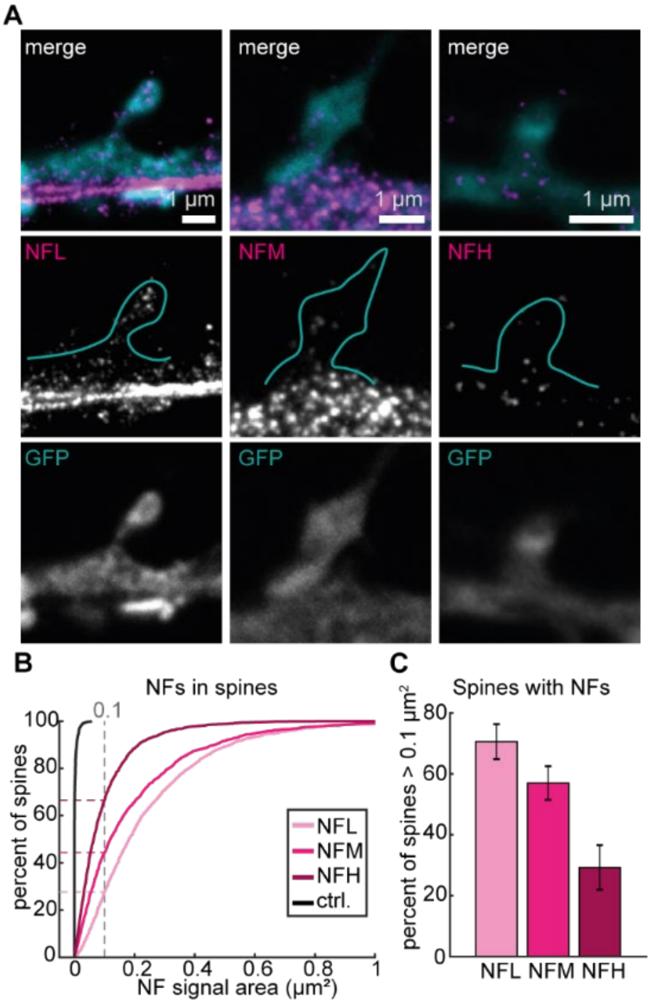

Figure 2. NF isoforms can be found at the postsynapse
(A) Representative STED images of dendritic spines with NFs (magenta) and volume labeling (confocal, cyan) with NFL (left), NFM (middle), or NFH (right). Spine shape as seen in volume labeling is represented in blue outline. Scale bars are 1 µm. (B) Cumulative distribution of spines containing NFs compared to control without primary antibody labeling. Dashed lines indicate individual values at a 0.1 μm^2 threshold. (C) Percentage of spines containing more than 0.1 μm^2 of NF signal. Data calculated from total 7660 spines (NFL=2360, NFM=1775, NFH=2768, ctrl=757) manually segmented from 9 independent experiments.

NF isoforms in spines correlate to different extents with postsynaptic strength marker homer

After having quantified the NF content at the postsynapse we questioned whether the presence of NFs is in dependence of different synaptic traits. Firstly, we tested the connection with postsynaptic strength as also described previously (Gürth et al. 2020). We therefore additionally quantified the STED signal of the postsynaptic marker homer together with the STED signal of either NFL, NFM or NFH in manually segmented spines (**Fig. 3A**). The amount of NF and the amount of homer were determined based on the area and mean intensity of the respective STED signal.

The correlation between these two relative protein amounts exhibited moderate correlation between postsynaptic size and amount of NFL ($\rho = 0.515$) and only low correlation for NFM ($\rho = 0.380$) and NFH ($\rho = 0.448$) (**Fig. 3B**). The presence of NFs is therefore differentially depending on postsynaptic strength as characterized by homer labeling with NFL having the strongest and NFM having the lowest correlation.

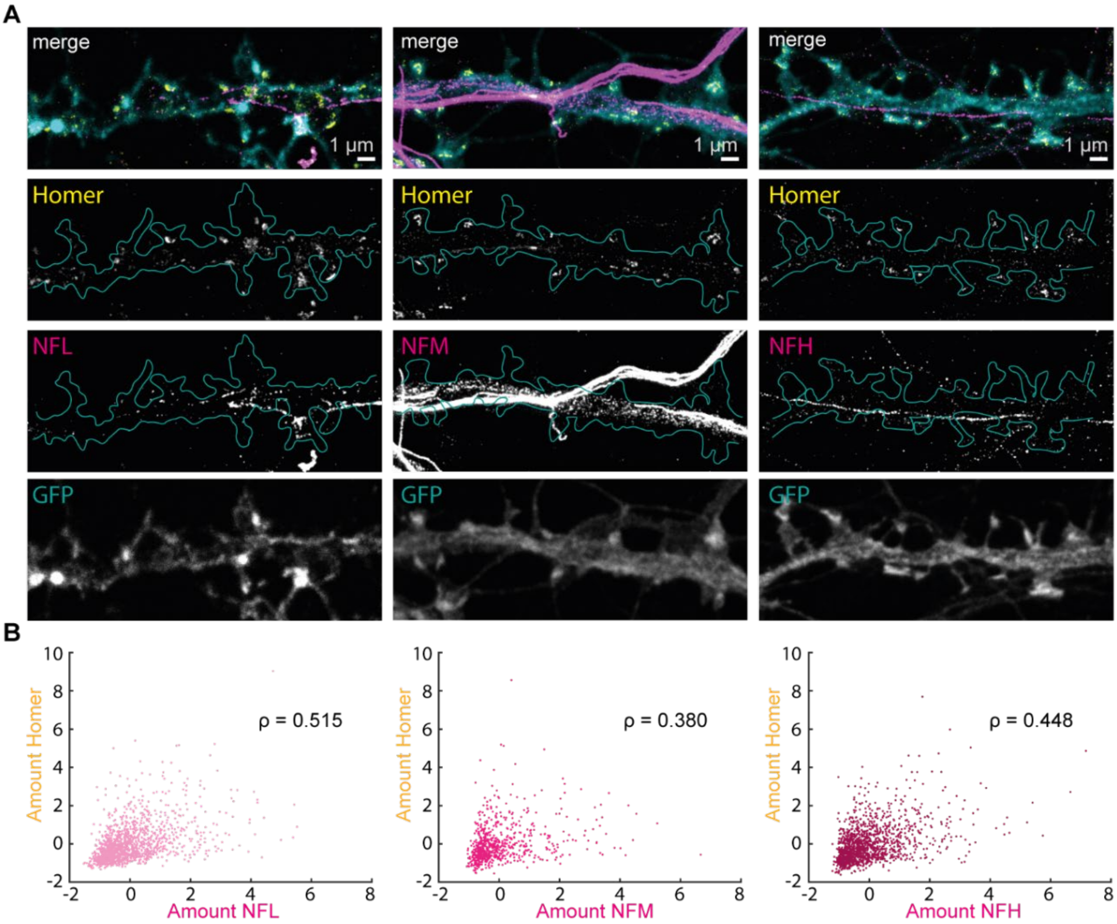

Figure 3. NFs at the postsynapse are present independently of postsynaptic strength

(A) Representative dual-color STED images of dendrites with homer (yellow), NFs (magenta), and volume labeling (confocal, cyan) with NFL (left), NFM (middle), or NFH (right). White outline represents spine shapes on the dendrite as determined by volume labeling. Scale bars are 1 µm. (B) Scatterplot of NF versus homer protein amount ($area \times mean\ intensity$). ρ indicates Spearmen's correlation coefficient with p values for NFL: $1.48e^{-101}$; NFM: $2.16e^{-27}$ and NFH: $2.93e^{-69}$. Data was obtained from 4637 manually segmented spines from 6 independent experiments, standardized to the mean of each experiment.

The amount of NFL at the post synapse correlates with presynaptic vesicle recycling

Since the presence of NFs appeared to be influenced by postsynaptic strength to a differing degree depending on the isoform, we next questioned whether the presence of NFs is further regulated by presynaptic activity. We therefore performed activity dependent live-labeling of Syt1, a proxy of synaptic activity, as previously described (Willig et al. 2006; Gürth et al. 2020). Specifically, immunolabeling of Syt1 was combined with immunolabeling of the three different NF isoforms as in previous experiments (**Fig. 4A**). The majority of spines showed distinct labeling of actively recycled synaptic vesicles as well as labeling of NFs in the case of all three isoforms. We then again correlated the amount of NFL, NFM or NFH with the number of actively recycled synaptic vesicles at individual synapses. We could observe a moderate direct correlation between synaptic activity and the presence of NFL ($\rho = 0.641$), showing that more active synapses have larger amounts of NFL at their postsynaptic side (**Fig. 4B**). Interestingly this correlation was lower for NFM and NFH amounts ($\rho = 0.305$ and 0.319, respectively). Hence NFL, the NF isoform that is most abundant at the postsynapse, shows a dependence not only to synaptic strength but also with synaptic activity.

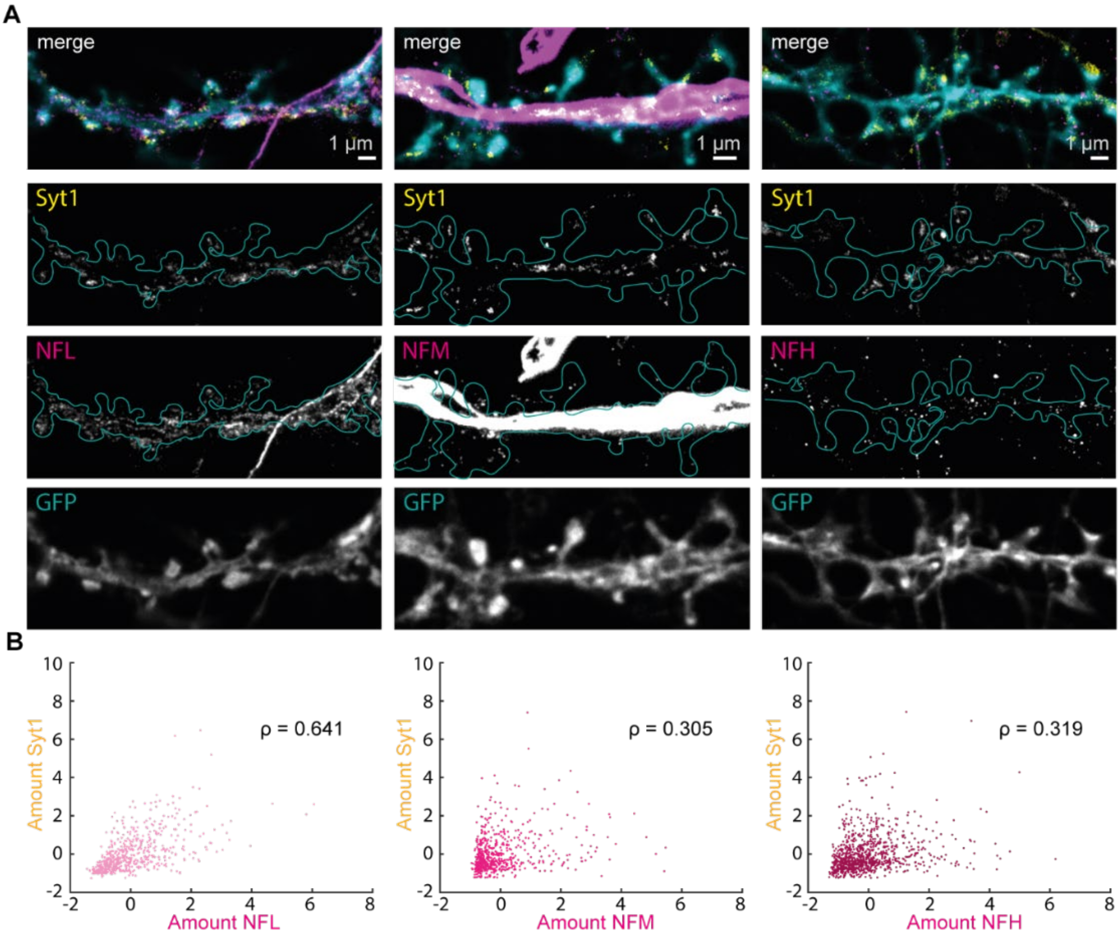

Figure 4. NFL at the postsynapse correlates with synaptic activity

(A) Representative dual-color STED images of dendrites with Syt1 (yellow), NFs (magenta), and volume labeling (confocal, cyan) with NFL (left), NFM (middle), or NFH (right). White outline represents spine shapes on the dendrite as determined by volume labeling. Scale bars are 1 µm. (B) Correlation scatterplot of NF protein amount and amount of labeled Syt1 ($area \times mean\ intensity$). ρ indicates Spearmen's correlation coefficient with p values for NFL: $2.55e^{-75}$; NFM: $2.23e^{-15}$, and NFH: $1.26e^{-23}$. Data was obtained from 2657 manually segmented spines from 3 independent experiments, standardized to the mean of each experiment.

Discussion

NFs belong to the most abundant proteins in neurons and are found in both axonal and dendritic regions. Although several studies suggest other NF functions beyond axonal structural support and connections with psychiatric disorders are known, their role at the synapse is only starting to emerge (Yuan and Nixon 2016; Kilinc 2018; Bucher et al. 2020). In the last decade, the presence of NF oligomers has been reported at postsynaptic sites, where they influence receptor function, LTP induction, and spine morphology (Yuan et al. 2017; Yuan and Nixon 2016). In this work, we used quantitative multicolor nanoscopy of the NF triplet to characterize its distribution, and identify correlations between its presence and synaptic traits. In particular, we analyzed the correlation between NFL, NFM, and NFH with either a marker of postsynaptic strength (homer) or a marker of presynaptic activity (Syt1, Willig et al. 2006; Gürth et al. 2020).

The use of STED nanoscopy in combination with volume labeling enabled us to differentiate with high lateral resolution the postsynaptic sites from dendritic or axonal shafts. However, the possibility exists that signal coming from overlapping pre-axonal terminals is detected within the same focal volume, deteriorating the specificity of the results. Importantly, the abundance of NF is clearly higher at the postsynapse than at the presynapse (Yuan et al. 2017). Furthermore, spines overlapping with obvious bright axonal signal were excluded from the analysis. Therefore, the impact of this technical limitation is minimized in this study.

Our study is based on antibody labeling and hence the results are strongly dependent on the specificity and ability to bind to the target structure of the used reagents. This aspect is relevant in the case of NFs, since they can be highly phosphorylated and the phosphorylation status of NF at synapses is distinctive compared to the rest of neurons (Yuan et al. 2015a; Yuan and Nixon 2016). Hence, the sensitivity of antibody labeling might differ based on the post-translational modification and the possibility exists that not all NF molecules are being detected. While this might have an impact on absolute quantification of synaptic NFs this should only minorly affect the comparative correlation analyses as applied here. Lastly the reagents did not exhibit co-localization at cellular and nanoscale level, indicating isoform-specificity.

Analysis of postsynaptic compartments revealed NF signal in the vast majority of dendritic spines. In these compartments, the area occupied by the fluorescent signal is bigger for NFL than NFM and NFH. This difference cannot be ascribed to different optical resolutions, since the same fluorophores and imaging conditions were utilized, and therefore represent a broader distribution of the antibody labeling. The higher abundance of NFL in dendritic spines supports the evidence that this isoform is essential for maintaining spine structure and function (Yuan et al. 2017). Furthermore, at postsynaptic sites we observed a poor co-localization of the NF isoforms, suggesting that they do not exclusively assemble in hetero-filaments. Together with the demonstration of isoform-specific interaction with receptors at synapses (e.g. NFL and NMDA receptors, NFM and D1 dopamine receptors, Kilinc 2018;

Karpova et al. 2013), this data point at isoform-specific functions of NFs within the context of the postsynapses.

To follow up on the hypothesis that different NF isoforms have different functions at the postsynapse, we investigated whether their presence depends on synaptic traits such as synaptic strength or activity. These analyses showed that the postsynaptically less abundant isoforms NFM and NFH also show lower correlation with synaptic strength and activity. The former has been shown to interact with dopaminergic receptors. Since in primary hippocampal cultures the majority of the population is represented by glutamatergic and not dopaminergic neurons (Björklund et al. 2010), the especially low level of correlation for NFM is unsurprising, and further confirms the evidence that NFM-null mice exhibit normal neurotransmission and LTP induction (Yuan et al. 2017). In NFH-null mice, however, LTP is impaired via yet unknown mechanisms. The lower level of correlation between NFH amount, and presynaptic activity and postsynaptic strength could therefore suggest its additional involvement in either activity independent synaptic processes or in more long-term synaptic plasticity mechanisms. Notably, the epitope recognized by the NFH antibody (AA998-1097 of mouse NFH, PhosphoSite.org) presents only a single phosphorylation site and therefore it is unlikely that the reduced correlation is due to different posttranslational modifications.

NFL showed a slightly different behavior than NFM or NFH, and did moderately correlate with both, synaptic activity and strength. This indicates that more active synapses had higher amounts of NFL present at the post synapse, suggesting a contribution of NFL to short-term plasticity and immediate response to activity changes as well as an involvement in long-term structural responses that would eventually result in an increased synaptic strength. Since NFL is known to interact with NMDA receptors via the GluN1 subunits the correlation between synaptic activity and NFL amount could also demonstrate its direct involvement in the modulation of synaptic signaling (Yuan et al. 2018). As a cytoskeletal component the involvement of NFL might include NMDA receptor positioning or more indirect changes mediated by the actin cytoskeleton.

Concluding, in this study we systematically quantified the presence of NFs at the postsynapse within the context of the synaptic status. Further work will be needed to clarify the behavior of internexin, the mechanisms through which NFL responds to synaptic activity, and how the presence of NFM and NFH at the postsynapse is regulated.

Conflict of interest

J.H is additionally affiliated with Abberior instruments GmbH

Contributions

E. D. conceived, designed and supervised the study, C-M. G. designed and performed experiments, V. M. P. performed experiments, J. H. developed and provided reagents, M. A. R. B. F. L. and A. R. C. D., contributed data and analysis tools, C-M. G and M. A. R. B. F. L. analyzed data, C-M. G, M. A. R. B. F. L. and E. D. wrote the manuscript. All authors contributed to manuscript revision, read, and approved the submitted version.

Acknowledgements

This work has been supported by the Deutsche Forschungsgemeinschaft (DFG, SFB1286/A07 to E.D.) and the Max-Planck-School Matter to Life (to C-M.G.). We thank Annette Herold, Magnus-Carsten Huppertz and Birgit Koch for support with neuronal cultures and virus production. We thank Jade Cottam-Jones for critical reading of the manuscript.

References

Björklund, Ulrika; Persson, Mikael; Rönnbäck, Lars; Hansson, Elisabeth (2010): Primary cultures from cerebral cortex and hippocampus enriched in glutamatergic and GABAergic neurons. In *Neurochemical research* 35 (11), pp. 1733–1742. DOI: 10.1007/s11064-010-0236-x.

Bomont, Pascale (2021): The dazzling rise of neurofilaments: Physiological functions and roles as biomarkers. In *Current opinion in cell biology* 68, pp. 181–191. DOI: 10.1016/j.ceb.2020.10.011.

Bragina, Luca; Conti, Fiorenzo (2018): Expression of Neurofilament Subunits at Neocortical Glutamatergic and GABAergic Synapses. In *Frontiers in neuroanatomy* 12, p. 74. DOI: 10.3389/fnana.2018.00074.

Bucher, Michael; Fanutza, Tomas; Mikhaylova, Marina (2020): Cytoskeletal makeup of the synapse: Shaft versus spine. In *Cytoskeleton (Hoboken, N.J.)* 77 (3-4), pp. 55–64. DOI: 10.1002/cm.21583.

Didonna, Alessandro; Opal, Puneet (2019): The role of neurofilament aggregation in neurodegeneration: lessons from rare inherited neurological disorders. In *Molecular neurodegeneration* 14 (1), p. 19. DOI: 10.1186/s13024-019-0318-4.

Ehlers, Michael D.; Fung, Eric T.; O'Brien, Richard J.; Huganir, Richard L. (1998): Splice Variant-Specific Interaction of the NMDA Receptor Subunit NR1 with Neuronal Intermediate Filaments. In *J. Neurosci.* 18 (2), pp. 720–730. DOI: 10.1523/JNEUROSCI.18-02-00720.1998.

Gürth, Clara-Marie; Dankovich, Tal M.; Rizzoli, Silvio O.; D'Este, Elisa (2020): Synaptic activity and strength are reflected by changes in the post-synaptic secretory pathway. In *Scientific reports* 10 (1), p. 20576. DOI: 10.1038/s41598-020-77260-2.

Karpova, Anna; Mikhaylova, Marina; Bera, Sujoy; Bär, Julia; Reddy, Pasham Parameshwar; Behnisch, Thomas et al. (2013): Encoding and transducing the synaptic or extrasynaptic origin of NMDA receptor signals to the nucleus. In *Cell* 152 (5), pp. 1119–1133. DOI: 10.1016/j.cell.2013.02.002.

Kilinc, Devrim (2018): The Emerging Role of Mechanics in Synapse Formation and Plasticity. In *Frontiers in cellular neuroscience* 12, p. 483. DOI: 10.3389/fncel.2018.00483.

Kim, Ok-Jin; Ariano, Marjorie A.; Lazzarini, Robert A.; Levine, Michael S.; Sibley, David R. (2002): Neurofilament-M interacts with the D1 dopamine receptor to regulate cell surface expression and desensitization. In *J. Neurosci.* 22 (14), pp. 5920–5930.

Leermakers, F. A. M.; Zhulina, E. B. (2010): How the projection domains of NF-L and alpha-internexin determine the conformations of NF-M and NF-H in neurofilaments. In *Eur Biophys J* 39 (9), pp. 1323–1334. DOI: 10.1007/s00249-010-0585-z.

Masch, Jennifer-Magdalena; Steffens, Heinz; Fischer, Joachim; Engelhardt, Johann; Hubrich, Jasmine; Keller-Findeisen, Jan et al. (2018): Robust nanoscopy of a synaptic protein in living mice by organic-fluorophore labeling. In *Proceedings of the National Academy of Sciences of the United States of America* 115 (34), E8047-E8056. DOI: 10.1073/pnas.1807104115.

Mukaka, M. M. (2012): Statistics corner: A guide to appropriate use of correlation coefficient in medical research. In *Malawi Medical Journal : The Journal of Medical Association of Malawi* 24 (3), pp. 69–71.

Nixon, R. A. (1993): The regulation of neurofilament protein dynamics by phosphorylation: clues to neurofibrillary pathobiology. In *Brain pathology (Zurich, Switzerland)* 3 (1), pp. 29–38. DOI: 10.1111/j.1750-3639.1993.tb00723.x.

PhosphoSite.org: PhosphoSite.org (PhosphoSite.org). Available online at https://www.phosphosite.org/proteinAction.action?id=7720&showAllSites=true.

Schindelin, Johannes; Arganda-Carreras, Ignacio; Frise, Erwin; Kaynig, Verena; Longair, Mark; Pietzsch, Tobias et al. (2012): Fiji: an open-source platform for biological-image analysis. In *Nature methods* 9 (7), pp. 676–682. DOI: 10.1038/nmeth.2019.

Suzuki, Tatsuo; Kametani, Kiyokazu; Guo, Weiheng; Li, Weidong (2018): Protein components of post-synaptic density lattice, a backbone structure for type I excitatory synapses. In *Journal of neurochemistry* 144 (4), pp. 390–407. DOI: 10.1111/jnc.14254.

Willig, Katrin I.; Rizzoli, Silvio O.; Westphal, Volker; Jahn, Reinhard; Hell, Stefan W. (2006): STED microscopy reveals that synaptotagmin remains clustered after synaptic vesicle exocytosis. In *Nature* 440 (7086), pp. 935–939. DOI: 10.1038/nature04592.

Yuan, A.; Sershen, H.; Veeranna; Basavarajappa, B. S.; Kumar, A.; Hashim, A. et al. (2015a): Functions of neurofilaments in synapses. In *Mol Psychiatry* 20 (8), p. 915. DOI: 10.1038/mp.2015.99.

Yuan, A.; Sershen, H.; Veeranna; Basavarajappa, B. S.; Kumar, A.; Hashim, A. et al. (2015b): Neurofilament subunits are integral components of synapses and modulate neurotransmission and behavior in vivo. In *Molecular psychiatry* 20 (8), pp. 986–994. DOI: 10.1038/mp.2015.45.

Yuan, Aidong; Nixon, Ralph A. (2016): Specialized roles of neurofilament proteins in synapses: Relevance to neuropsychiatric disorders. In *Brain research bulletin* 126 (Pt 3), pp. 334–346. DOI: 10.1016/j.brainresbull.2016.09.002.

Yuan, Aidong; Nixon, Ralph A. (2021): Neurofilament Proteins as Biomarkers to Monitor Neurological Diseases and the Efficacy of Therapies. In *Frontiers in neuroscience* 15, p. 689938. DOI: 10.3389/fnins.2021.689938.

Yuan, Aidong; Rao, Mala V.; Veeranna; Nixon, Ralph A. (2012): Neurofilaments at a glance. In *Journal of cell science* 125 (Pt 14), pp. 3257–3263. DOI: 10.1242/jcs.104729.

Yuan, Aidong; Rao, Mala V.; Veeranna; Nixon, Ralph A. (2017): Neurofilaments and Neurofilament Proteins in Health and Disease. In *Cold Spring Harbor perspectives in biology* 9 (4). DOI: 10.1101/cshperspect.a018309.

Yuan, Aidong; Veeranna; Sershen, Henry; Basavarajappa, Balapal S.; Smiley, John F.; Hashim, Audrey et al. (2018): Neurofilament light interaction with GluN1 modulates neurotransmission and schizophrenia-associated behaviors. In *Translational psychiatry* 8 (1), p. 167. DOI: 10.1038/s41398-018-0194-7.

Zolotukhin, Sergei; Potter, Mark; Zolotukhin, Irene; Sakai, Yoshihisa; Loiler, Scott; Fraites, Thomas J. et al. (2002): Production and purification of serotype 1, 2, and 5 recombinant adeno-associated viral vectors. In *Methods (San Diego, Calif.)* 28 (2), pp. 158–167. DOI: 10.1016/s1046-2023(02)00220-7.

Supplementary information

Supplementary Method -Western Blot

Whole mouse brain lysate or cultured hippocampal primary neurons (DIV18) lysed in Laemmli buffer (Bio-Rad, cat. 161-0747) were loaded in a 4-15% gradient SDS gel (Bio-Rad, cat. 4561086), together with a protein standard (Bio-Rad, cat.161-0394) and subjected to electrophoresis at 50 V for 5 min, followed by 100 V for 90 min. Separated proteins were then transferred onto a PVDF membrane (Bio-Rad, cat. 162-0260) at 120 V for 60 min. The blotted membranes were blocked in Tris-buffered saline, 0.1% Tween (TBST), 3% BSA and incubated overnight with previously described NF primary antibodies and for 1 hour at RT with α-tubulin mouse (Sigma, cat. T9026) or GAPDH rabbit (Cell Signaling, cat. 2118) at 1:500-1:1000 dilution in TBST, 1% BSA. Then the membranes were washed five times in TBST and incubated with secondary antibodies (Alexa Fluor 488 anti-mouse, Thermo Fisher, cat. A32723, Alexa Fluor 488 anti-chicken, Thermo Fisher, cat. A-21467, Alexa Fluor 647 anti-rabbit, Thermo Fisher, cat. A-21245) at 1:1000 dilution in TBST 1% BSA for 1 hour at room temperature. Afterwards membranes were washed five times in TBST and fluorescent signal was detected in a ChemStudio (Jena Analytik GmbH).

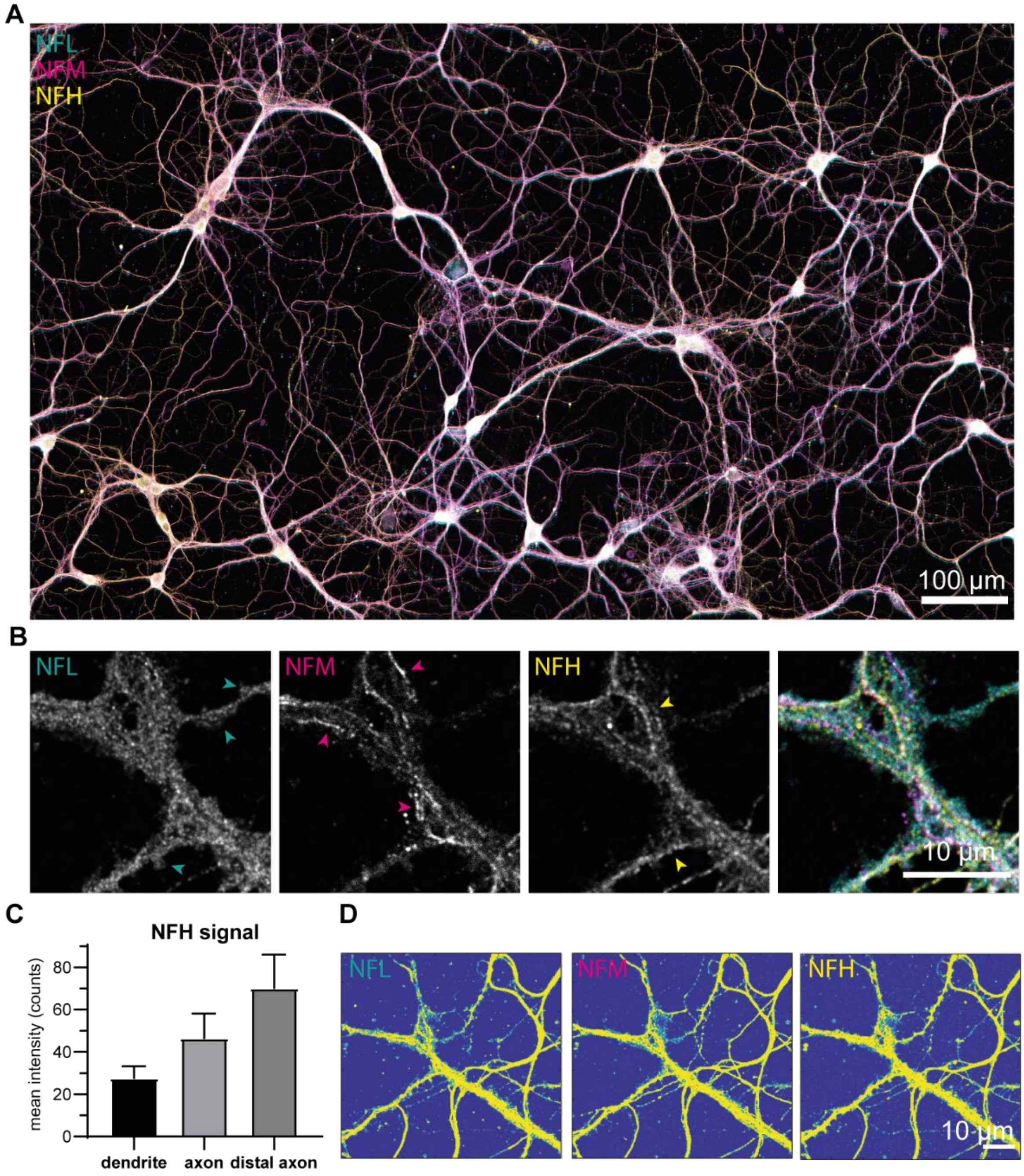

Figure S 1. Immunofluorescent labeling of NFs in primary hippocampal cultures

(A) Stitched confocal overview image of the different NF isoforms NFL (cyan), NFM (magenta) and NFH (yellow) in primary cultured neurons. Scale bar is 100 µm. (B) Enlarged area of Fig. 1A. Arrows in single channel images indicate characteristic granular or filamentous NF structure. (C) Signal mean intensity of NFH in dendrites and axons. Error bars represent SEM, data from 9 different cells in 3 different field of views. (D) Representative segmentation by thresholding of individual confocal fluorescent channels for colocalization analysis. Images correspond to the field of view shown in Fig. 1A.

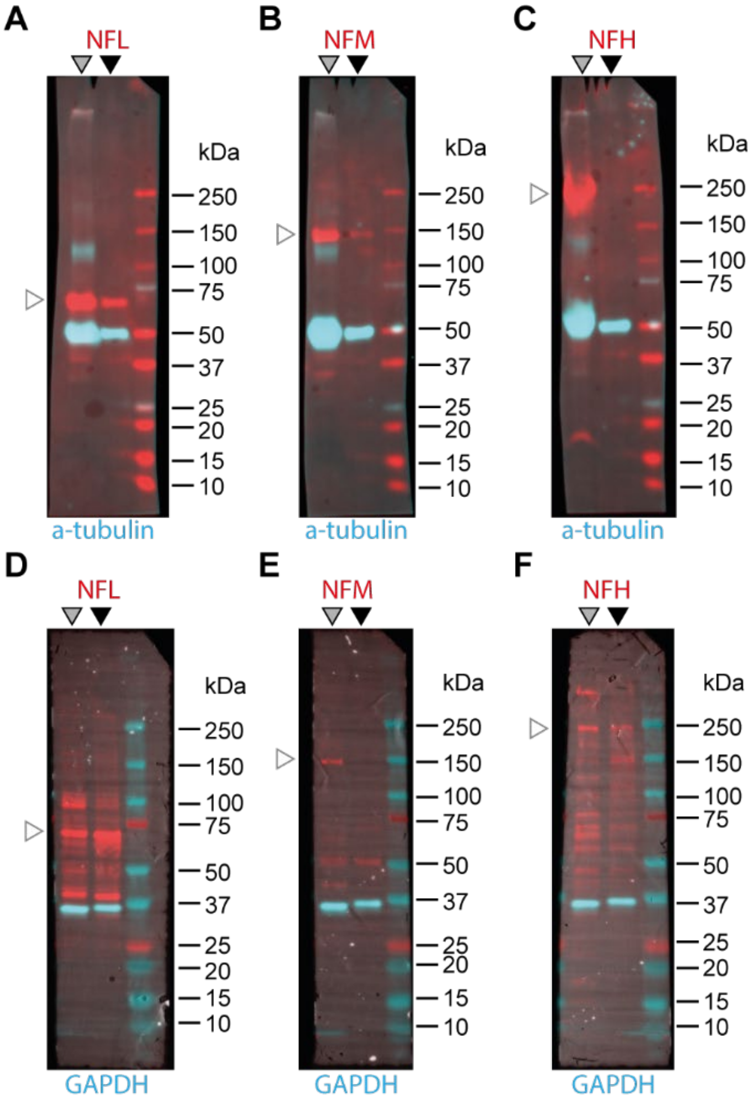

Figure S 2. NF antibody validation in western blot

Dual color fluorescent western blot on whole brain lysate of a P18 mouse (left lane, gray arrow) or lysate of rat hippocampal cultures as used for STED experiments (middle lane, black arrow), compared to a protein standard ladder (right lane). Top row: NFL (A) NFM (B) or NFH (C) rabbit primary antibody in red. Alpha-tubulin mouse primary antibody in cyan. Bottom row: NFL chicken (D), NFM mouse (E) or NFH mouse (F) primary antibody in red. GAPDH rabbit primary antibody in cyan. White arrows show expected heights of NF isoforms.

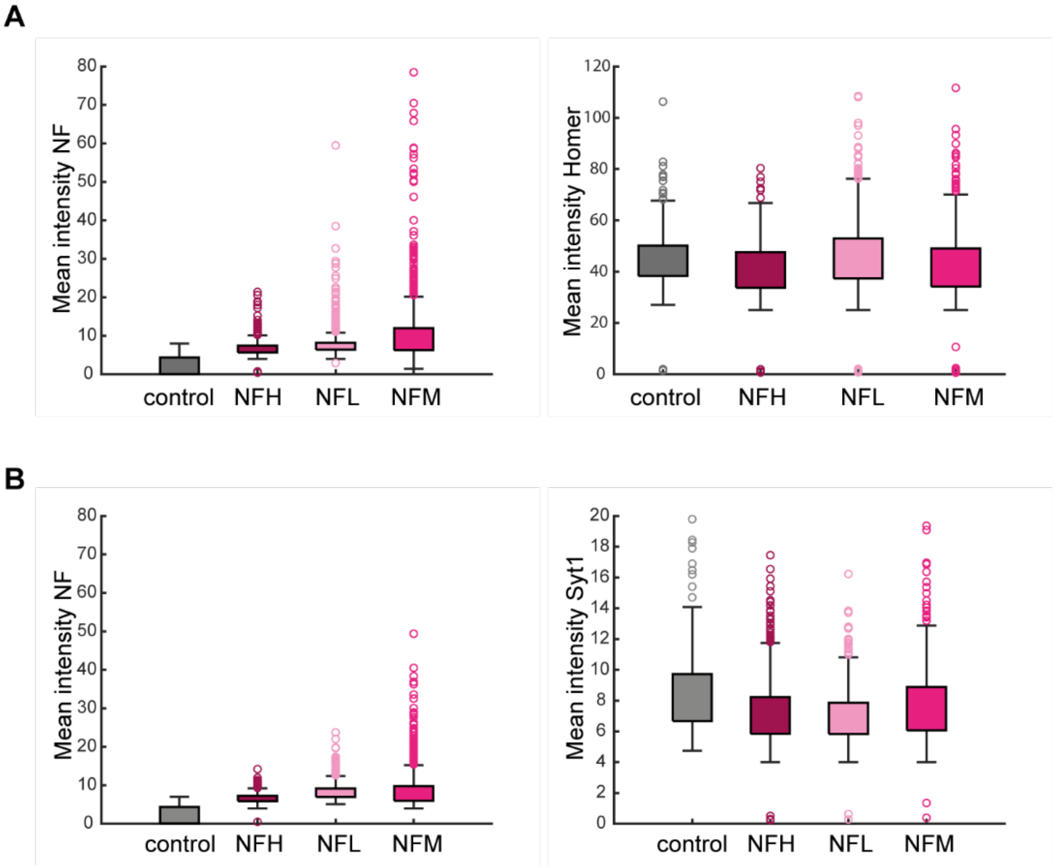

Figure S 3. Intensity quantification of NF and synaptic labeling at manually segmented postsynapses in dual color STED images

(A) Mean intensity of NF (left) and homer (right) in manually segmented spines from 6 independent experiments. (B) Mean intensity of NF (left) and Syt1 (right) in manually segmented spines from 3 independent experiments. Controls are samples labeled without primary NF antibodies. Values represent mean of raw photon counts.

Chapter 4 – PSD-95 Turnover and Nano-dynamics

PSD-95 supports synaptic plasticity by regulating its abundance and organization and thereby influencing the positioning of neurotransmitter receptors. This study combines endogenous gene editing, STED and MINFLUX nanoscopy to investigate how neuronal activity impacts the PSD-95 new protein integration and nanoscale organization at individual synapses.

Within this study I performed all sample preparation, all STED imaging experiments, and most MINFLUX experiments with blinking dyes. I processed and segmented STED images and contributed to data processing of STED and MINFLUX experiments. I contributed to the preparation of most figures and the final manuscript.

This manuscript was prepared for submission:

- Shared first authorship
- Anticipated submission: July 2022

Multicolor STED and MINFLUX Nanoscopy reveal activity dependent PSD-95 nanodynamics

Clara-Marie Gürth*[1,2] & Maria Augusta do Rego Barros Fernandes Lima*[1], Jasmine Hubrich[1], Angel Rafael Cereceda Delgado[1,2], Victor Macarrón Palacios[1,2], Felipe Opazo[4,5], Nikolaos Mougios[4,5], Stefan W Hell[2] and Elisa D'Este[3]

[1] Department of Optical Nanoscopy, Max-Planck-Institute for Medical Research, Heidelberg, Germany

[2] Department of NanoBiophotonics, Max-Planck-Institute for Multidisciplinary Sciences, Göttingen, Germany

[3] Optical Microscopy Facility, Max-Planck-Institute for Medical Research, Heidelberg, Germany

[4] Institute of Neuro- and Sensory Physiology, University Medical Center Göttingen, Germany

[5] Center for Biostructural Imaging of Neurodegeneration (BIN), University Medical Center Göttingen, Germany

* Contributed equally to this study

Abstract

The postsynaptic density component PSD-95 undergoes activity-dependent plasticity mechanisms, which rely on protein synthesis and structural remodeling. How synaptic activity can influence these dynamics on a single synapse level is yet unclear. Here we combine genome-editing, pulse-chase experiments, STED and 3D MINFLUX nanoscopy on hippocampal neuronal cultures to investigate the integration of new PSD-95 molecules at postsynaptic sites and their rearrangements within individual clusters at molecular resolution. We show that the amount of new PSD-95 recruited to individual synapses scales with synaptic size, and modulates in a bidirectional manner, resulting in less new protein upon excitatory and more new protein upon inhibitory stimulation. Furthermore, we demonstrate monodirectional activity-dependent structural rearrangements of PSD-95 clusters. Indeed, the distance between PSD-95 molecules decreases, leading to a density increase for both, excitatory and inhibitory stimulation, resulting in more compact clusters. Altogether, this work sheds new light into the mechanisms underlying plasticity at the individual synapse level adding previously inaccessible information.

Introduction

Synaptic scaling is a homeostatic mechanism induced at the level of synaptic sites – the smallest functional units in memory formation – by long-lasting changes in activity. It is supported by sub-cellular protein synthesis and mediated through changes in postsynaptic AMPA receptor accumulation (Turrigiano and Nelson 2004; Lee and Kirkwood 2019; Galanis and Vlachos 2020).

Post Synaptic Density 95 (PSD-95) is a key component of the excitatory postsynaptic compartment controlling the position of AMPA and NMDA receptors (Coley and Gao 2018; Iasevoli et al. 2013; Fukata et al. 2021). PSD-95 facilitates synaptic scaling by (i) adapting the scaffolding surface for AMPA receptors docking and (ii) by changing the PSD geometry. Indeed, protein degradation and synthesis bidirectionally modulate PSD-95 protein levels during synaptic scaling (Butko et al. 2012; Ehlers 2003; Donlin-Asp et al. 2021), as proved by biochemical methods at the whole-culture level (Ehlers 2003; Bingol and Schuman 2004). Newly synthetized PSD-95 molecules are incorporated at the postsynapse, and electron microscopy data on a small number of synapses suggest that these molecules do not only replace the old ones but also exhibit a distinct localization and possibly function (Butko et al. 2012). However, this hypothesis has so far not been verified. An extensive, comparative analysis of the accumulation and localization of newly synthesized PSD-95 proteins *in situ* at the single synapse level within the context of synaptic scaling is lacking.

PSD-95 geometry is highly dynamic and finely regulated as it influences the alignment of postsynaptic receptors with presynaptic release sites and thereby the efficiency of neuronal transmission (Broadhead et al. 2016; Masch et al. 2018; Wegner et al. 2018; Broadhead et al. 2020; Sun et al. 2021). At the nanoscale, PSD-95 clusters in 80-180 nm-sized nanodomains, which can be considered as PSD basic structural units or building blocks (MacGillavry et al. 2013; Nair et al. 2013; Broadhead et al. 2016). The majority of the synaptic sites exhibits only a single nanodomain (MacGillavry et al. 2013; Broadhead et al. 2016). However, the number of these structures is finely regulated and influenced by synaptic scaling induced by a persistent inhibitory (but not excitatory) stimulation (Broadhead et al. 2016; MacGillavry et al. 2013). Recently, 3D MINFLUX imaging of the PSD-95 organization in cultured hippocampal neurons, revealed the presence of tens of sub-nanodomain PSD-95 structures per synaptic site with a size of 4-10 nm and distanced ~40 nm, therefore below or at the limit of the resolution capabilities of previous studies (Gwosch et al. 2020, see **Fig. 1**). Whether and how these newly identified structures re-arrange in response to synaptic scaling mechanisms is not known.

Here, we dissect the two mechanisms through which PSD-95 reacts to inhibitory and excitatory synaptic scaling at sub-synaptic level: (i) we perform pulse-chase experiments on endogenously HaloTag-tagged PSD-95 in cultured neurons followed by quantitative multicolor STED nanoscopy to analyze the amount and distribution of newly synthetized proteins; (ii) we used nanobodies to analyze the anatomy and organization of PSD-95 units by 3D MINFLUX.

Methods

Preparation of neuronal cultures

All procedures were performed in accordance with the Animal Welfare Act of the Federal Republic of Germany (Tierschutzgesetz der Bundesrepublik Deutschland, TierSchG) and the Animal Welfare Laboratory Animal Regulations (Tierschutzversuchstierverordnung) and no specific authorization or notification was required. The procedure for sacrificing P0–P2 rats performed was supervised by animal welfare officers of the Max Planck Institute for Medical Research (MPImF) and conducted and documented according to the guidelines of the TierSchG (permit number assigned by the MPImF: MPI/T-35/18).

Primary hippocampal cultures were prepared from dissociated tissue of P0-P1 postnatal wild-type Wistar rats of either sex (Janvier-Labs) as described previously in D'Este et al. 2015; Gürth et al. 2020. Briefly, dissected hippocampal tissue was digested with 0.25% trypsin for 20 minutes at 37°C, mechanically dissociated by pipetting, and maintained in Neurobasal supplemented with 2% B27, 1% GlutaMAX and 1% penicillin/streptomycin (all from Gibco, Thermo Fisher Scientific). Cells were seeded at a concentration of 110,000/well in 12-well plates on Ø 18mm glass coverslips coated with 0.1 mg/ml poly-ornithine (Sigma) and 1 µg/ml laminin (Corning). Medium was changed to fresh supplemented Neurobasal 1-2 hours after seeding and cultures were maintained in an incubator (37°C, 5%CO_2) until DIV21-25 in presence of residual glial cells.

Plasmid generation and viral vector production

Plasmids pAAV-hSyn-PSD-95-Halo for overexpression controls was constructed as described in (Masch et al. 2018), pAAV-EFS-SpCas9 (Addgene #104588) was a gift from Ryohei Yasuda (Nishiyama et al. 2017), and pAAV ORANGE Dlg4-HaloTag KI (Addgene #139656) was a gift from Harold MacGillavry (Willems et al. 2020). The preparation of adeno-associated viral vectors was performed as previously described in Masch et al. 2018 and purified as described in Zolotukhin et al. 2002.

Pulse-chase labelling of PSD-95-Halo

Cultured neurons were infected at DIV7 with AAV-ORANGE-Dlg4-Halo (PSD-95) and AAV1/2-EFS-SpCas9 or rAAV1/2-hSyn-PSD-95-Halo. Mature cultures (DIV15-20) were labeled with either 580CP-Halo or SiR-Halo, 1 µM in preconditioned Neurobasal for 2 hours at 37°C to achieve complete labeling of tagged structures. Afterwards cultures were washed in warm ACSF (126 mM NaCl, 2.5 mM KCl, 2.5 mM $CaCl_2$, 1.3 mM $MgCl_2$, 30 mM Glucose, 27 mM HEPES) and brought back in culture in their own preconditioned Neurobasal.

After further 48 hours in culture the labeled samples were relabeled with the respective other dye at 0.5 µM and at the same time stimulated with 1.5 µM Tetrodotoxin (TTX, Tocris, cat. 1078) or 10 µM Gabazine (GZ, SR 95531 hydrobromide, Tocris, cat. 1262) for 24h at 37°C in preconditioned Neurobasal.

Prior to immunolabelling cultures were fixed in 4% PFA in PBS, pH 7.4, quenched with quenching buffer (PBS, 100 mM glycine, 100 mM ammonium chloride), permeabilized for 5 min in 0.1% Triton X-100 and blocked with 1% BSA for 1 hour. Samples were then incubated for 1-2 hours at room temperature each with primary antibodies, secondary antibodies and dyes, each followed by five washes in PBS. Antibodies and dyes used were anti-Halo-Tag (Promega, cat. G928A, 1:200 dilution), FluoTag-X2-anti-PSD95-Sulfo-Cy5 (NanoTag Biotechnologies GmbH, cat. N3702-SC5-L, 1:200 dilution), FluoTag-X2-anti-PSD95-580 (NanoTag Biotechnologies GmbH, cat. N3702-AbStar580-L, 1:200 dilution), Alexa Fluor 405 anti-rabbit (Thermo Fisher, cat. A31556, 1:100 dilution), Phalloidin Alexa Fluor 405 (Thermo Fisher, cat. A30104; 1:200 dilution), and Phalloidin StarGREEN (Abberior GmbH, cat. STGREEN-0100-20ug, 1:100 dilution). Samples for confocal and STED imaging were afterwards embedded in Mowiol® supplemented with DABCO and cured for at least 1 hour at RT before imaging. Samples for MINFLUX imaging were mounted with gold nanorods (Nanopartz, cat. A12-40-980-CTAB-DIH-1-25) in blinking buffer (cysteamine concentration 10 mM) as described in Schmidt et al. 2021.

Confocal, STED and MINFLUX imaging

Samples were imaged on an Abberior Expert Line Microscope (Abberior Instruments GmbH) on a motorized inverted microscope IX83 (Olympus) and equipped with pulsed STED lines at 775 nm and 595 nm, excitation lasers at 355 nm, 405 nm, 485 nm, 580 nm, and 640 nm, and spectral detection. Spectral detection was performed with avalanche photodiodes (APD) and detection windows were set to 650-725 nm, 600-630 nm, 505-540 nm, and 420-475 nm to detect Atto647N/Star635P, Alexa Fluor 594/Star580, Alexa Fluor 488/StarGREEN and Alexa Fluor 405, respectively. Images were acquired either with a 20x/0.4 NA oil immersion lens with pixel size at 100 nm or with a 100x/1.4 NA oil immersion lens, 30 nm pixel size, and pinhole to 100 µm (1 AU). Laser powers and dwell times were kept consistent during the entire experiments.

MINFLUX Imaging was performed on an Abberior 3D MINFLUX (Abberior Instruments GmbH) built on a motorized inverted microscope IX83 (Olympus) and equipped with 640 nm, 561 nm, 485 nm, and 405 nm laser lines. Detection was performed with 2 APDs in the spectral windows 650-685 nm and 685-720 nm. Images were acquired using the default 3D imaging sequence, with an L in the last iteration step of 40 nm, and photon limit of 100 and 50 photons for the lateral and axial localization, respectively.

Image processing and analysis

Images shown in figures were visualized and processed with Imspector (Abberior Instruments GmbH) and FIJI (Schindelin et al. 2012). STED images are shown as raw data. Brightness was adjusted uniformly throughout the images. MINFLUX data was analyzed in Matlab (version 2021b, MathWorks) and Python (Python Software Foundation).

To quantify the relative amount PSD-95-Halo in STED images, PSD-ROIs were determined based on the confocal 488 nm channel, in which the anti-HaloTag antibody was imaged. Therefore, a "moments" threshold was applied and background signal (below 0.2 µm²) was eliminated with the analyze particles function. These ROIs were then used to determine signal area and intensity in the 640 and 580 nm STED channels by applying "moments" or "isodata" thresholding, respectively and then measuring area and intensity within this thresholded area for each individual PSD site separately. Amount was calculated by multiplying the signal area by the mean signal intensity and normalized with respect to the control. For images displaying imaging artefacts that influenced the overall maximum intensity (reflections or dye accumulations resulting in bright non-specific puncta) a maximum intensity was individually set and exceeding extreme values were cropped to the default maximum using Matlab. The mean amounts of old and new proteins in treated samples were normalized for each respective experimental round to the mean of DMSO treated samples (**Fig. 2b**). Within each treatment condition, the amounts for each experimental round were binned into 5 equally spaced intervals and the respective mean values for each bin were fitted with a linear regression (**Fig. 2d-f**), similarly of what performed in (Gürth et al. 2020; Dankovich et al. 2021).

For co-localization analysis, PSD-95 signal was segmented from the background using a binary mask. The mask was generated by saturating 99% of the original image, followed by an 8 pixels median filtering and an automatic Otsu's global threshold. ROIs smaller than 200 pixels or greater than 25000 pixels were excluded from the binary mask, in order to exclude background noise or dye accumulation. The binary mask was then applied to each respective image, and the Pearson's correlation coefficient and the Mender's coefficients were computed. The analysis was made using a custom MATLAB code.

PSD-95 size based on sdAB-PSD-95 STED images was measured by applying a customized threshold (4-70 counts). ROIs of structures bigger than 0.02 µm² were created and the size of the PSD-95 of neurons treated under different conditions were analyzed.

MINFLUX data analysis

Four filters were applied in the post-processing step to avoid false single molecule emission events. To exclude detections originated from transient background, we set two maximum thresholds of 0.7 for the center frequency ratio (CFR) test and 200 kHz for the detected fluorescence rate (Gwosch et al. 2020).

Localizations from the same emission trace, i.e. with same trace identification (TID), farther than three standard deviations with respect to the mean trace position were considered outliers and excluded from the trace. Only the traces containing at least 5 localizations were considered. The experimental localization precision was estimated by co-aligning the mean values of all localizations obtained from individual emission traces fitted with a Gaussian function to estimate the overall standard deviation (Pape et al. 2020).

Spatial analysis

The point pattern spatial analysis was done considering the TID centroid position as a point in a 3D Euclidian space. A density-based spatial clustering of applications with noise (DBSCAN) algorithm was applied to define the 3D PSD Clusters. The MATLAB built in function *dbscan* was used with a minimum number of neighbors *(minPoints)* equal to 25 and a search radius (*eps*) varying from 200 nm to 300 nm depending on the PSD size. For the PSD units clustering, another DBSCAN was performed with *minPoints* = 1 and *eps* = 15 nm. For each PSD cluster, the 3D alpha shape was retrieved using the MATLAB *alphashape* function with the default critical alpha radius. The PSD volume, surface area and x-y projected area were derived from each cluster alpha shape.

To test for complete spatial randomness (CSR) of TID distribution within the PSD clusters, the Diggle-Cressie-Loosmore-Ford (DCLF) test was implemented using Monte Carlo simulations. The G-function was used as the spatial descriptor for the DCLF test. Each synthetic PSD cluster consisted of randomly distributed points, conditioned by the number of TIDs, the volume and the full range of nearest neighbor distances for the observed PSD cluster. For each observed cluster, 500 synthetic clusters under CSR were generated. The observed G function (G_{OBS}) was then, compared with the expected G function under CSR (G_{CSR}) and its Monte Carlo confidence envelopes. The largest and smaller nearest neighbor distance for which the G_{OBS} was respectively greater or smaller than G_{CSR} were used as indicators of spatial interaction.

Results

HaloTag pulse-chase to visualize PSD-95 protein turnover *in situ*

We set out to examine PSD-95 de *novo protein* synthesis at individual synaptic sites. To this aim, we firstly established a labelling strategy based on the self-labelling enzyme HaloTag (Los et al. 2008) providing molecular specificity while preserving spatial information. We performed a pulse-chase experiment using spectrally separated, live-cell compatible HaloTag substrates applied to neuronal cultures at different timepoints. This system was implemented on CRISPR/Cas9 endogenously tagged neurons to guarantee the expression of the PSD-95-HaloTag from its native promoter (Willems et al. 2020). Rat hippocampal neuronal cultures were transduced at 7 DIV with two AAVs encoding for SpCas9, or PSD-95-gRNA and HaloTag, respectively. At 21 DIV labelling of PSD-95-Halo protein present in the cells was saturated with the first fluorescent Halo substrate (580CP-Halo, 1 µM for 2 h). Cultures were then incubated for two days prior to the adding of a second Halo substrate labelling newly synthetized protein (SiR-Halo, 0.5 µM for 24 h, **Fig. 1a, b**). The completeness of both labelling steps was tested by applying a second label in a control experiment without any intermediate incubation step (**Fig. S1**). For both 580CP-Halo and SiR-Halo labelling conditions, no detectable fluorescence from the second fluorophore was present, demonstrating that all available HaloTags were indeed successfully labeled.

Next, we tested the sensitivity of pulse-chase to new protein synthesis. To this aim, we overexpressed PSD-95-Halo and applied the Halo substrates sequentially as previously described. Both 580CP and SiR signals could clearly be detected at synaptic sites, indicating that both pre-existing and newly synthesized proteins could indeed be visualized. Importantly, the new protein was reduced by ~50 % after treatment with the protein synthesis inhibitor cycloheximide (**Fig. S1**). Concluding, these experiments demonstrate the measurability of different levels of protein synthesis *in situ* by combining HaloTag and CRISPR/Cas9.

Newly synthetized PSD-95 does not homogeneously mix with the old PSD-95 protein

We next evaluated the new protein synthesis of PSD-95 in multi-color STED images of pulse-chase labelled mature neuronal cultures. STED images show signal of both, old and new PSD-95-Halo in the majority of synaptic sites and an overlap of both channels although some intensity peaks in either the old or new protein channel are visible (**Fig. 1b, c**). To test the relative distribution of the different protein pools at individual synapses, we performed a colocalization analysis, which did not reveal a clear co-segregation of the proteins (**Fig. 1d**). Co-occurrence measurements show an overlap between both channels of approximately 50%, indicating that the channel of the new protein (SiR) occupied half of the area of the channel of the old protein (580CP, **Fig. S1c**). However, this might be ascribed to the fact that 580CP delivers a lower resolved STED image than SiR due to the smaller cross-section with the STED beam, with consequently larger PSD area in the 580CP channel. To test this influence, we generated control images in which the SiR channel was artificially deteriorated with a 3-pixel gaussian filter to compare the same signal at different resolutions (control images). We then compared the correlation coefficients of pixels which have a non-zero value in both channels of real images and observed a correlation of only around 50%, against 75% in generated control images (**Fig. 1e**). Thus, signal of old and new protein pool did not fully colocalize suggesting that although new synthesized protein is present in the entire PSD, it is not homogenously mixed with the old PSD-95.

Newly synthetized PSD-95 scales with synaptic site size

We questioned whether new PSD-95 protein insertion occurs at constant rates over the entire synapse population. To this aim, we used an antibody against HaloTag to identify all synaptic sites of genome-edited cells and applied a high throughput image analysis workflow to compare the relative amounts of pre-existing and newly synthetized PSD-95-Halo in more than 2000 synapses. Using different fluorophores prevents an absolute comparison of signal intensities and therefore we evaluated relative protein amounts, measured as signal areas times mean pixel intensity (amount = area x mean_{int}). Interestingly, the relative amounts of old and new PSD-95 strongly correlated in all synaptic sites, regardless of their size (**Fig. 1f**). Since in our data there is a strong correlation between protein amount and PSD area (**Fig. S2c**), this correlation shows that bigger synaptic sites also incorporate larger quantities of newly synthetized PSD-95 and smaller PSD sites possess lower levels of new protein. Hence, newly synthesized protein is not equally distributed between synaptic sites but rather depends on and scales up with the size of the postsynapse.

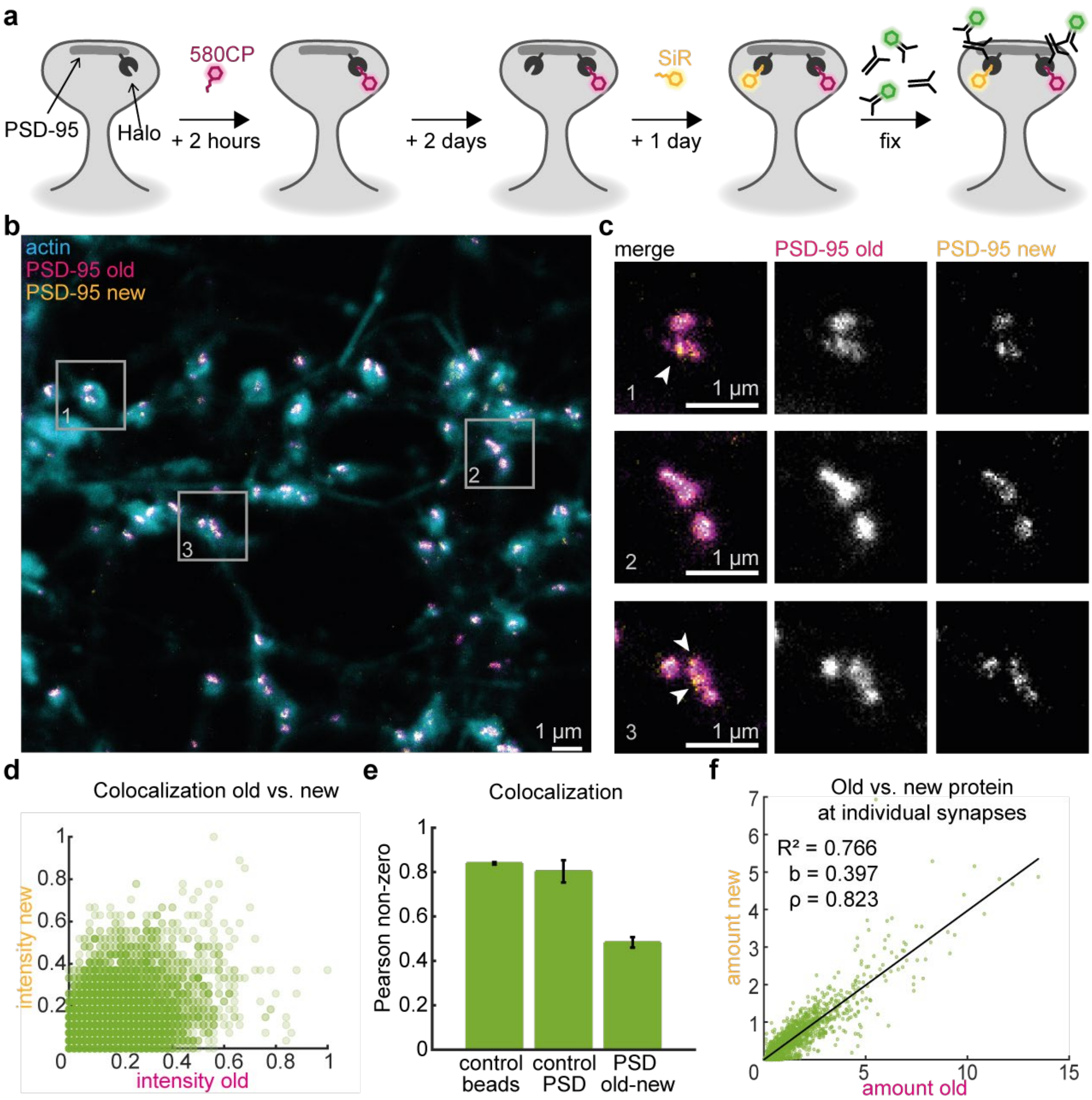

Figure 1. Pulse-chase labelling of endogenous PSD-95 turnover

(a) Experimental workflow of pulse-chase labelling of Halo tagged PSD-95 in neuronal cultures. Mature neuron cultures, endogenously expressing PSD-95-HaloTag were labelled with live cell Halo dye (magenta, 580CP), then washed and kept in culture for 2 more days. Newly synthesized PSD-95-Halo protein was then labelled with a second live cell Halo dye (yellow, SiR) for 24 hours followed by fixation and immunolabelling with antibody against HaloTag (green) before STED imaging. (b) Representative overview of dual color STED image of protein turnover. Grey boxes represent synapse shown in (c) numbered from top to bottom. Scale bar is 1µm. (d) Colocalization of old and new protein in dual color STED images in normalized pixel intensity correlation (calculated for image shown in b) and (e) Pearson non-zero coefficient of old and new protein compared to a control image in which the resolution of the SiR channel has been blurred to achieve comparable resolution. Mean and SEM values of 0.8030 ± 0.05 and 0.4832 ± 0.0238 for control (N = 4) and PSD old-.new (N= 15), respectively. (f) Correlation of old versus new protein amounts at individual synaptic sites (n=2148, N=5). Amount was calculated as product of pixel area and mean intensity of each individual PSD site. Black line is a linear fit with slope (b), coefficient of determination (R^2), and Spearman's correlation coefficient (ρ).

Accumulation of new PSD-95 at synaptic sites depends on neuronal activity

The size of synapses is thought to relate to their activity and we observed that larger synapses exhibit a higher amount of newly synthetized protein. Therefore, we questioned whether insertion of new PSD-95 at the PSD is influenced by activity. To test this hypothesis, we silenced or enhanced neuronal activity by treating cultures for 24 hours after the first pulse-chase with tetrodotoxin (TTX) or gabazine (GZ), respectively (**Fig. 2a, c**). We then compared the relative amounts of old and new labelled PSD-95-Halo in the different conditions (**Fig. 2b**). Although the levels of old protein remained constant in-between treatments, there was a significant increase of new protein at synaptic sites in TTX treated cultures and a decrease of new protein in GZ treated cultures compared to cultures treated with the vehicle DMSO. This resulted in an overall smaller PSD area and lower PSD-95 amount in GZ treated cultures (**Fig. S2**), while no statistically significant difference was observed for TTX treated cells.

Next, we tested whether the correlation between old and new PSD-95 shifts in treated cultures. We observed strong correlations between the amount of old PSD-95 and new PSD-95 in all conditions (**Fig. 2d-f, Fig. S3, Supplementary Table S1**). To better quantify and compare the different dataset, we grouped the data into 5 bins with the same number of elements (Gürth et al. 2020; Dankovich et al. 2021). Binned data confirm the strong correlation highlighted different tendencies towards old or new protein, as reflected by the steepness of the linear fit. Indeed, while for TTX the steepness of the fit was increased compared to the control (b=0.453 and b=0.339, respectively), it was reduced for GZ treatment (b=0.190, **Fig. 2d-f**). The ratios between new and old protein therefore was higher in TTX treated samples and lower in GZ treated samples. This indicates an overall higher incorporation of new protein upon synaptic scaling induced by prolonged TTX treatment, and a reduced incorporation of new protein upon prolonged GZ stimulation at the single synapse level, with an effect linearly depending on the size of the PSD.

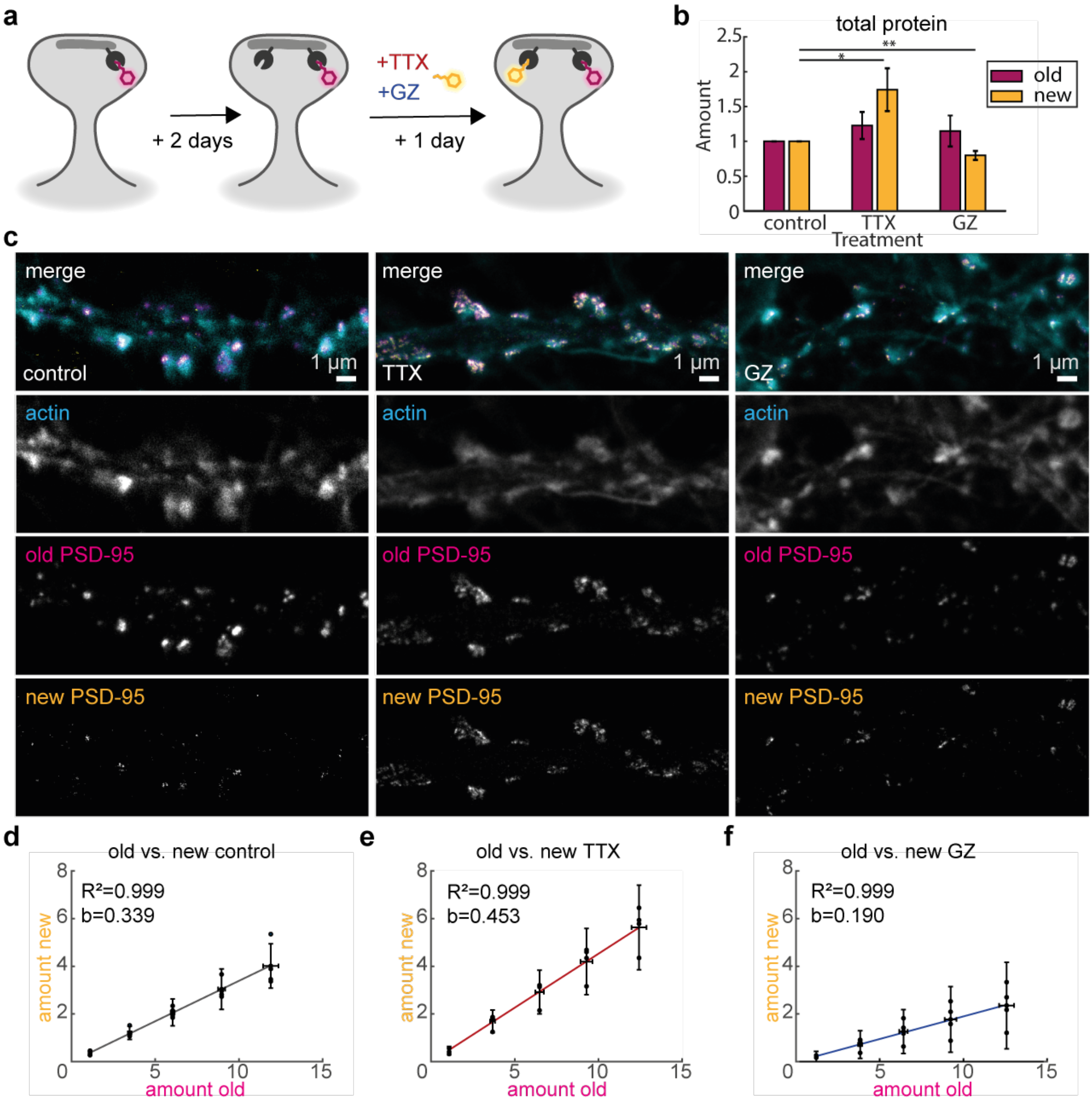

Figure 2. Activity dependent changes in PSD-95 turnover

(a) Workflow of pulse-chase labelling with stimulation or silencing of neuronal activity. Mature cultures were labelled with the first live cell Halo substrate (magenta, 580CP-Halo), then washed and kept in culture for 2 more days. Newly synthesized PSD-95-Halo protein was then consecutively labelled with a second live cell Halo-substrate dye (SiR-Halo, yellow) for 24 hours and, at the same time, cultures were treated with either tetrodotoxin (TTX) or gabazine (GZ). (b) Quantification of relative overall protein turnover. Relative change of old (magenta) or new (yellow) PSD-95 protein amount (product of pixel area and mean intensity) are plotted as mean of 4 independent experiments, compared to control (DMSO only). Error bars represent SE, * = $p < 0.05$, ** = $p < 0.01$. (c) Representative multi-color STED and endogenously PSD-95-Halo expressing dendrites in treated cultures and corresponding actin signal (confocal). Samples were live labeled with 580CP-Halo (old, magenta), SiR-Halo (new, yellow) and post fixation labelled with phalloidin (actin, confocal). Scale bar is 1µm. (d, e, f) Correlation of the amount of old PSD-95-Halo protein and new PSD-95-Halo protein binned in 5 bins of equal size for control- (d, n=1858) TTX- (e, n=1183) and GZ- (f, n= 790) treated cultures from 4 independent experiments. Amount was calculated as product of pixel area and mean intensity of each individual PSD site. Black line is linear fit with slope b and coefficient of determination R^2. Vertical and lateral error bars indicate SE.

MINFLUX shows PSD-95 clustering below nanodomain organization

Synaptic scaling does not impact only protein turnover but also the overall architecture of PSD-95 (Noritake et al. 2009; Iasevoli et al. 2013). Therefore, we set out to investigate the nanoscale organization of PSD-95 as a function of activity. To this aim, we performed 3D MINFLUX nanoscopy in fixed hippocampal cultures labeled with a single domain antibody (sdAB) against PSD-95 (**Fig. 3**) decorated with two SulfoCy5 molecules. While in confocal imaging PSD-95 appeared as nearly micron-sized domains, in 3D MINFLUX synaptic sites are revealed by localization clusters spaced by 20-40 nm (**Fig. 3a, b**). Indeed, MINFLUX enabled the visualization of PSD-95 with a localization precision of σ_x= 5.5 ± 0.8 nm, σ_y= 5.6 ± 0.8 nm, and σ_z= 2.9 ± 1.2 nm (**Fig. S4**) by using 100 and 50 photons for xy and z, respectively. The obtained resolution was significantly higher than what obtained in previous studies analyzing changes in PSD geometry in 2 dimensions (MacGillavry et al. 2013; Nair et al. 2013).

By 3D MINFLUX imaging using PSD-95 sdAb we obtain a median value of 133 TIDs (trace ID or localizations stemming from an individual blinking event) per synaptic site (**Fig. 3f**). Frequently, closely located TIDs were visualized. These clusters could correspond to multiple localizations of the same fluorophore, to the presence of 2 fluorophores bound to each sdAb, or to the presence of very closely packed PSD-95 molecules. Since we could not discriminate between these options, all TIDs distancing up to 8.5 nm from each other were grouped and assigned to what we defined as an individual PSD "unit" (**Fig. 3c**). This value corresponds to the Euclidian distance between two points in a 3D space, separated by ~2σ in each dimension, i.e. $\sqrt{2\sigma_x + 2\sigma_y + 2\sigma_z}$. The majority (~90%) of the units was formed by a single TID and the median number of units per cluster was 101. The median nearest neighborhood distance (NN) between units was ~35 nm (**Fig. 3f**). Importantly, labeling of the sdAb with DNA-PAINT instead of a blinking dye led to statistically undistinguishable values, suggesting that the imaging procedure is effectively detecting the majority of molecules (**Fig. S5**).

Previous data reported clustering of PSD-95 (Broadhead et al. 2016; MacGillavry et al. 2013; Nair et al. 2013), and hence we analyzed whether this behavior can be observed also at the higher resolutions achieved by MINFLUX. To this aim, we applied the Diggle-Cressie-Loosmore-Ford (DCLF) test (Baddeley et al. 2014), using the G function as a spatial descriptor, to test for complete spatial randomness for the TIDs distribution within the confined PSD volume (**Fig. S5**). The test was based on 500 Monte Carlo simulations of randomly distributed points, conditioned by the observed pattern size (number of TIDs), the observed volume, and the full range of observed nearest neighbor distances for each PSD cluster. The results showed with a confidence level $\alpha = 0.002$ that in 87% of the PSDs the TIDs were not randomly distributed. Furthermore, an analysis based on the G function confidence envelopes from Monte Carlo simulations revealed an attractive trend for nearest neighbor distances smaller than 61 nm and a dispersive trend for distances greater than 100 nm (**Fig. 3d, e**). This clustering behavior on a low nanoscale suggests a spatial interaction of the molecules within the PSD cluster, endorsing the presence of nanodomains (**Fig. 3c**). Notably, the appearance of nanodomains as previously reported becomes evident from the 2D project of the 3D data (**Fig. 3e**).

Having access to 3D information, enabled us to precisely analyze the volume (median ~0.3 µm^3) and shape of the PSD-95 clusters (**Fig. 3f**), with a median compactness, measured as the cubic sphericity (i.e. $\pi \; x \; 36 \; x \; V^2/S^2$ where V is the volume and S the superficial area) of ~0.3, indicating a mainly flat geometry. The density of units in the PSD-95 volume was nearly ~4700 U/µm^3.

Next, we correlated these measured parameters within the synapse population to identify trends regulating PSD-95 morphology (**Fig. 3g**). The correlation matrix shows high (blue squares) and low (red squares) correlation coefficients among 35 synaptic sites. While there was a strong correlation between the number of units and the volume of the PSD cluster, showing that higher numbers of PSD-95 units led to larger PSD clusters and fewer units resulted in smaller PSD clusters, the compactness did not correlate with both, number of units and cluster volume. The density of the cluster (volume unit density, 3Dd) was more sensible to changes in the cluster volume than to the number of units, indicating that larger clusters have also less dense molecules. The nearest neighbor distances between units showed no correlation to the cluster volume and, as expected, a strong negative correlation to the cluster density. Notably, values based on the 2D projection of the 3D MINFLUX data failed in revealing some of the significant correlations/anticorrelations (**Fig. 3g**). All in all, these data indicate that bigger PSD-95 clusters have more, but more separated units, while smaller clusters are denser. Importantly, they also reveal the larger amount of information which can be uniquely obtained by 3D MINFLUX imaging compared to previous 2D STORM, PALM and STED data (Nair et al. 2013; MacGillavry et al. 2013; Broadhead et al. 2016; Perez-Alvarez et al. 2020; Perez de Arce et al. 2015).

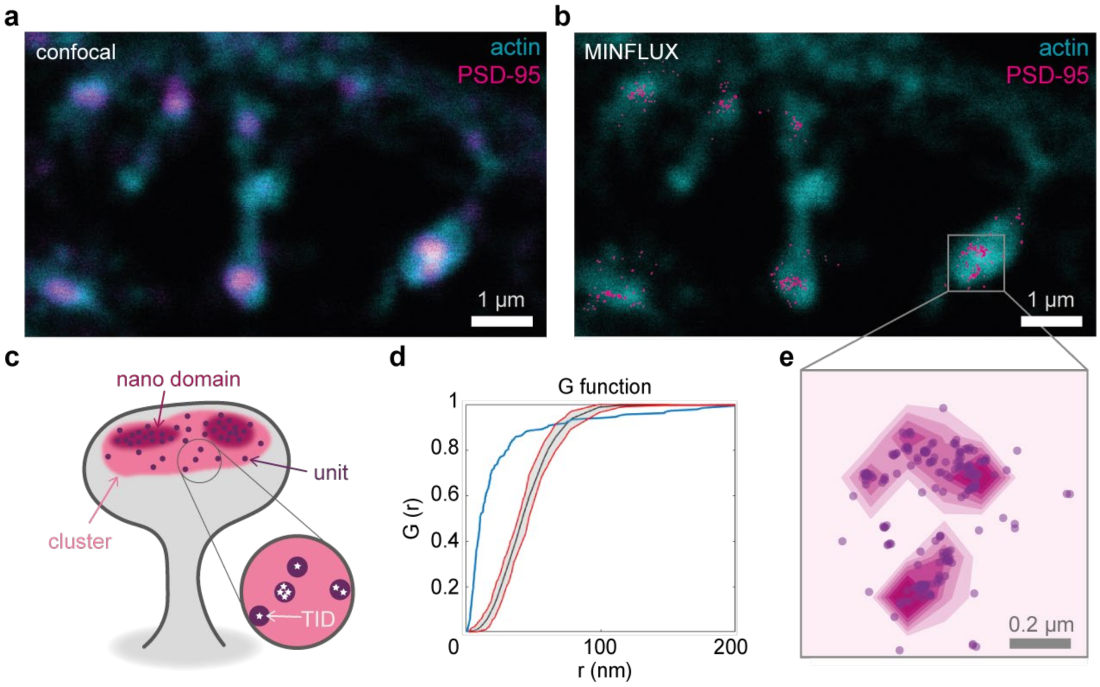

f

Parameter	Median	Iqr
TIDs per cluster	133	225.5
Units per cluster (No)	101	149.5
Cluster volume (CV)	0.0298 µm³	0.0434 µm³
Cluster projected area	0.237 µm²	0.240 µm²
Compactness (Com)	0.324	0.231
3D unit density (3Dd)	4691 U/µm³	7381 U/µm³
2D unit density (2Dd)	121.2 U/µm²	182.4 U/µm²
Nearest neighbor distance (NN)	35.0 nm	19.4 nm

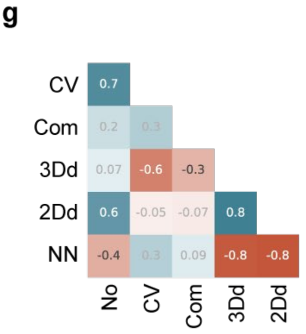

	No	CV	Com	3Dd	2Dd
CV	0.7				
Com	0.2	0.3			
3Dd	0.07	-0.6	-0.3		
2Dd	0.6	-0.05	-0.07	0.8	
NN	-0.4	0.3	0.09	-0.8	-0.8

Figure 3. MINFLUX nanoscopy of PSD-95 organization in neuronal cultures

(a) Representative confocal image of a mature dendrite labelled with phalloidin (cyan) and sdABs against PSD-95 (magenta). Scale bar is 1µm. (b) 3D MINFLUX measurement of PSD-95 in the same area with TIDs rendered at 20 nm spot size. Grey square indicates region shown and analyzed in (d-e). (c) Scheme of organization levels of PSD-95 at the synapse. One PSD cluster (entire pool of PSD-95 at the postsynapse) can be organized in nanodomains (high level clustering) and PSD units (low level clustering). Each PSD-95 unit can be composed by a single or multiple TIDs within 15 nm. (d) Clustering analysis of PSD-95 localizations (blue line) compared to randomly distributed particles as established from Monte Carlo simulations (red-grey). This G function refers to the PSD-95 cluster shown in (e). (e) 3D representation of MINFLUX TIDs in one representative PSD-95 cluster. Magenta gradient shows level of clustering. Scale bar is 200 nm. (f) Table of quantified parameters of 35 PSD-95 clusters in 3D MINFLUX measurements from 6 cells and 3 independent experimental rounds. (g) Correlation matrix of measured parameters using Spearman correlation. Parameters: No – number of TIDs, CV – cluster volume, Com – compactness, 3Dd – unit density in 3D (units/µm^3), 2Dd – unit density in 2D projected clusters (units/µm^2), NN- unit nearest neighbor distance. Blue to red square color gradient indicates a positive to negative correlation, as indicated by the number. White squares indicate that the correlation is not significant (corresponding p-values in table S1).

PSD-95 3D organization changes in an activity-dependent manner

Having characterized the nanoscale architecture of PSD-95 clusters in basal conditions, we wanted to investigate whether their arrangement is as well influenced by synaptic activity. Therefore, we performed 3D MINFLUX measurements on cultures that were treated with DMSO (control), TTX or GZ for 24 hours (**Fig. 4a, b**). While all conditions had comparable median numbers of units in each PSD cluster, the overall cluster volume was reduced by GZ treatment (**Fig. 4c**). This reduction is size of the PSD-95 cluster was similar as in results from 2D STED images (**Fig. S2**). The change in volume consequently led to an increased 3D density of units within the PSD cluster in GZ treated cultures, but also in TTX treated cultures, which was further reflected in the significant reduction of nearest neighbor distances between units from a median of ~50 nm in control clusters to ~40 nm in TTX and GZ treated PSD-95 clusters. Similar – but not statistically significant – tendencies were observed in a TID based density comparison (**Fig. S6**), although we could observe a slightly increased number of TIDs per cluster for TTX treated samples. The number of TIDs per unit also exhibited limited changes (**Fig. S6**).

When analyzing the correlation between the different parameters at individual PSD-95 cluster level, we observed that both TTX and GZ treatments induced a stronger correlation between number of units and cluster volume compared to the control (**Fig. 4d**). This suggests that TTX treatment causes a larger reduction in unit density in larger synapses, whiles smaller synapses are less affected. In control and TTX-treated samples we could observe that the PSD volume slightly correlated with the nearest neighbor distance. This dependence was not present in GZ treated cultures. Similarly, the negative correlation between 3D density and PSD compactness in control and TTX treatment was reduced by GZ treatment. This indicates that in GZ treated cultures the distance between units is more constant regardless of the PSD cluster, which are however on average smaller and denser. Altogether, these data show a unidirectional behavior in the nanoscale organization of TTX and GZ treated cultures, and show a change in the proximity and density of molecules, and 3D geometry of the whole PSD-95 cluster.

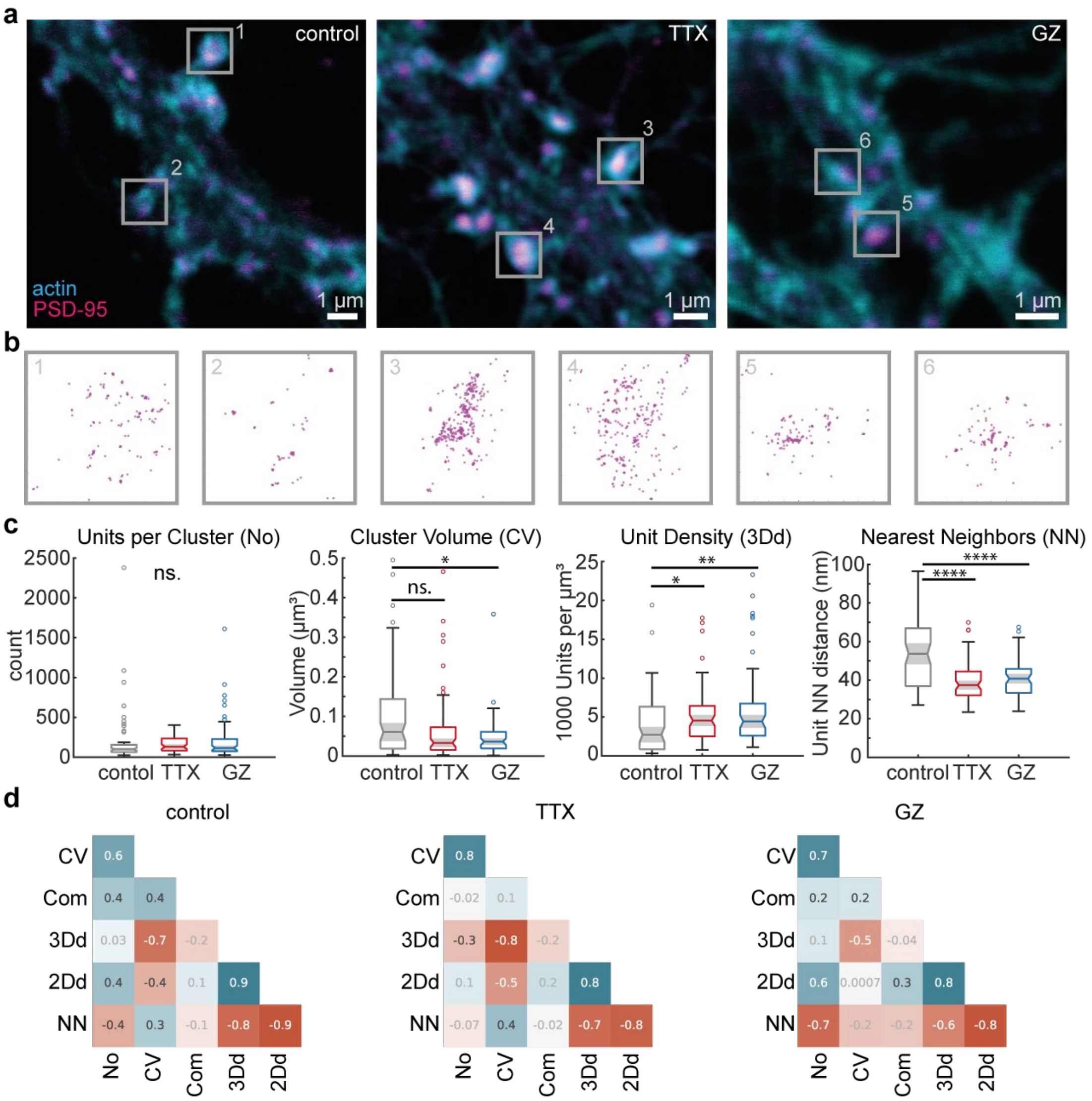

Figure 4. MINFLUX nanoscopy of activity dependent PSD-95 organization

(a) Representative confocal images of mature dendrites labelled with phalloidin (cyan) and sdABs against PSD-95 (magenta) and stimulated with DMSO (control), TTX or GZ for 24 hours prior fixation. Scale bar is 1µm. Grey squares indicate 1 x 1 μm^2 regions of 3D MINFLUX measurements (b) 2D representation of TIDs from 3D MINFLUX measurements of individual PSD clusters. Grey squares are 1 x 1 μm^2. Rendered are TIDs with an approximate radius of 15 nm. (c) Quantification of units per cluster, cluster volume, unit density and nearest neighbor distances of PSD-95 clusters in 3D MINFLUX measurements depending on treatment (numbers of analyzed PSD clusters: control=74, TTX=74, GZ=61 of 8-9 cells from 5 independent experimental rounds) Error bars represent SE, asterisks indicate: * = $p < 0.05$, ** = $p < 0.01$, *** = $p < 0.001$, **** = $p < 0.0001$, ns. = not significant. (d) Correlation matrix of measured parameters depending on treatment. Parameters: No – number of Units, CV – cluster volume, com – compactness (sphericity), 3Dd – unit density per μm^3, 2Dd – unit density per μm^2 projected area, NN- unit nearest neighbor distance. White/black numbers indicate significant/non-significant correlations. Blue to red square color gradient indicates a positive to negative correlation, as indicated by the number. White squares indicate that the correlation is not significant (corresponding p-values in table S1).

Discussion

Understanding synaptic homeostatic processes such as scaling or plasticity requires knowledge of the complex underlying molecular mechanisms at individual synapses. Here, we focus on the scaffolding protein PSD-95, which plays a key role in regulating the positioning of receptors at the postsynapse (Ehrlich and Malinow 2004). We investigate how neuronal activity impacts PSD-95 synthesis, incorporation, and organization at the single-synapses level by leveraging on different labeling strategies combined with optical nanoscopy techniques.

A thorough interpretation of the presented results requires a deep understanding of the caveats of the advanced experimental approach used. Therefore, we will firstly discuss relevant technical aspects of our work.

To investigate whether and where newly synthetized PSD-95 protein is incorporated at the synapse we combined pulse-chase labeling with the ORANGE gene editing system to tag endogenous PSD-95 with a HaloTag (Willems et al. 2020), allowing to study PSD-95 expression at physiological levels in mature neurons. With this approach, we were able to detect newly synthetized PSD-95 together with a pre-existing pool of PSD-95 over the course of 3 days. Within this timeframe we expected measurable fractions of both, old and new protein, since the protein lifetime of PSD-95 has been reported to be around 3.5 days (Alvarez-Castelao and Schuman 2015; Cohen et al. 2013; Blanpied et al. 2002; Ehlers 2003; Cohen et al. 2013; Bulovaite 2022).

However, it is possible that we did not visualize all PSD-95 molecules completely. Although we could clearly identify successfully genome-edited cells, we could not verify the grade of genomic integration. Our measurements might contain next to homozygous also few heterozygous PSD-95-Halo knock-in cells, even if signal intensities did not show different populations due to the intrinsically high dynamic range of the synaptic signal. Therefore, we cannot exclude the possible presence of untagged PSD-95 at analyzed synapses, however we assume a similar behavior of both, untagged and tagged proteins and hence no alteration to the overall protein dynamics.

Furthermore, the possibility exists that not all HaloTag molecules are successfully labelled with the fluorescent substrate. Incorporation of the HaloTag substrate is generally a highly efficient process (Erdmann et al. 2019; Lepore et al. 2019). However, different fluorophores exhibit different kinetics (Wilhelm et al. 2021). To minimize these issues, we incubated the cells at comparably high substrate concentrations for long times (1 µM for 2 h, = 5 x higher and 8 x longer than in Willems et al. 2020) and could demonstrate that virtually all accessible molecules were labelled (**Fig. S1a**).

Lastly, our study provides relative values instead of absolute quantification of fluorophore signals. Relative measures account for variations in labeling efficiency and changes in protein dynamics related to the fluorophore, allowing an unbiased comparison between samples. Pulse-chase experiments were analyzed with STED nanoscopy, a technique which enables a relatively high throughput in a multicolor setting and with limited cross-talk between channels.

A drawback of our approach is that imaging has been performed enhancing exclusively the lateral and not the axial resolution. Hence, the observed fluorescence signal corresponds to a two-dimensional projection of the labelled structures. Notably, this limitation impacts the co-localization of the protein species, but has minimal relevance when analyzing protein amounts, intended as area x mean fluorescence intensity. Indeed, axially overlapping structures will have a smaller apparent area but higher fluorescent intensities.

We investigated the geometrical arrangement of PSD-95 using single-color 3D MINFLUX nanoscopy of PSD-95 labeled with sdABs. Compared to conventional immunolabeling protocols sdABs minimize the displacement between the fluorophore and the protein of interest from up to 30 nm to under 3 nm (Pleiner et al. 2015; Ries et al. 2012). The monovalent nature of sdABs moreover abolishes the risk of protein clustering as caused by conventional antibodies and ensures a higher degree of labeling of the structures of interest (Sograte-Idrissi et al. 2020). Whether all PSD-95 molecules are successfully targeted by a sdAB and whether the signal of the conjugated fluorophores is detected while imaging cannot be reliably tested, since of synaptic sites lack a predictable geometry as in reference structures like nuclear pore complexes (Thevathasan et al. 2019). When comparing our median number of PSD-95 molecules per synapse (133) with proteomic data on PSD-95 copy numbers (300-500, Cohen et al. 2013; Helm et al. 2021) we assume a detection of around one quarter of the present PSD-95 molecules. This only partial visualization might be due to either lack of sdAB binding to PSD-95, or lack of fluorophore detection due to bleaching, fluorophore interaction, or influences of the microenvironment. DNA-PAINT experiments using a similar sdAB labeling approach led to comparable results and therefore rule out the influence of the first two possibilities. Hence, we can assume that all PSD-95 molecules accessible to the nanobody have been localized by the image acquisition. Since labeling and imaging conditions were kept constant throughout all experiments with limited effects on comparative measurements.

Our analysis is primarily based on “PSD units”, which groups all neighboring molecules within a 8.5 nm distance from each other in accordance with our approximate biological resolution in 3D MINFLUX data. This measure is therefore not affected by interactions between closely located molecules, re-localization of the same molecules, or the presence of two fluorophores per PSD-95 molecule. Additionally, a tight clustering of PSD-95 with the consequent inaccessibility of the nanobody binding domain will also not have an impact on the number and distribution of the PSD-95 units.

To quantify the deposition of newly synthetized PSD-95 in a large number of synapses, we applied an automated image analysis workflow. We could observe that there is a bigger integration of new PSD-95 protein at larger synapses compared to small synapses, however the ratio between old and new PSD-95 remained constant throughout the entire synaptic population. Our findings indicate that larger amounts of new protein are being deposited at bigger postsynaptic sites. Therefore, the process of new protein incorporation is regulated on a single synapse level rather than on a cellular level. This could be due to targeted transport to individual synapses based on synaptic tagging or to the availability of more protein production machinery around larger synaptic sites (Gürth et al. 2020; Frey and Morris 1997; Hanus et al. 2014; Barco et al. 2002; Fonseca et al. 2004). A similar correlation in which larger synaptic sites have a higher protein turnover has been observed at the single synapse level for the presynapse (Jähne et al. 2021). Our results demonstrate a comparable pattern for the postsynaptic compartment. A connection between new protein formation and the presence of protein production machinery or directly local transcription could further help to understand where protein transcription is regulated at individual synaptic sites.

The exact analysis of the distribution of new and old PSD-95 protein in STED nanoscopy suffers from the different resolutions achieved in the two imaging channels. Nonetheless, we did not observe a complete segregation but rather a partial but incomplete co-localization of the two protein pools. This data shows that the new pools is intermixed with the old pool but suggests that it might also have distinct functions (Butko et al. 2012).

At even higher molecular resolution, we did observe a clustering behavior of TIDs at a distance of around 40 nm in the majority of synapses. This clustering might be an effect of either direct PSD-95 interactions or of several PSD-95 molecules that reside within the same limit of our localization precision (< 7 nm), however we cannot determine the exact number of PSD-95 molecules with our approach.

When treating our cultures with TTX or GZ to induce plasticity we observed a bidirectional modulation of new and pre-existing PSD-95 protein pools: For neuronal silencing with TTX we observed a higher ratio of newly synthetized PSD-95. On the other hand, for GZ enhanced neuronal activity, we observed a lower ratio of newly synthetized PSD-95. Levels of the old protein pool remained thereby constant. This increased incorporation of new protein affects all synapses, linearly depending on their size. Interestingly our MINFLUX measurements showed a reduced volume of GZ treated PSD clusters.

Both, TTX and GZ treated cultures showed a denser packing of PSD-95 units at a smaller overall volume of the PSD cluster while the average numbers of PSD units per synapse remained constant. This is most significantly reflected in the reduced nearest neighbor distances in drug treated cultures.

Contrary to MINFLUX measurements we did not observe this reduced volume of PSD clusters in STED experiments. STED experiments were performed as 2D measurements and therefore did not allow the determination of PSD cluster volumes. In comparison projected 2D areas of PSD clusters showed no significant reduction in area (**Fig. S1**). The resolution in STED images however did not allow to characterize PSD areas at the same level as PSD cluster volumes in MINFLUX data. Cluster analysis compartmentalized the postsynapse in sometimes multiple PSD clusters that might be summed up to one continuous PSD ROI in STED measurements. Therefore, even the projected PSD area from 3D MINFLUX data cannot be directly compared to 2D STED measurements.

The elevated deposition of new PSD-95 that we observed could be a contributing factor to synaptic scaling, which has been already observed upon enduring TTX treatment in other studies (Sun and Turrigiano 2011; Kim et al. 2007; Noritake et al. 2009). As expected stimulation of neuronal activity with GZ had opposite effects: while also here amounts of old PSD-95 remained similar we could observe a reduced amount of newly synthetized PSD-95 in GZ treated cultures. An increased neuronal activity stalled the synthesis of new PSD-95 and therefore shifted the ratio of PSD-95 protein pools towards more old protein. Although the relative amount of old protein seemed to be unaffected by treatment we cannot estimate the contribution of protein degradation in this analysis. Labelled PSD-95-Halo that is being degraded during our 3-day timeframe is not visible anymore at our end point imaging. Hence, the higher ratio of old PSD-95 in GZ treated cultures might as well be affected by a reduced protein degradation at more active synapses but this contribution remains to be quantified. However, overall changes in new protein amount suggest a strong contribution of de novo protein synthesis to the ratio of old and new pools of PSD-95.

This raises the question how newly synthetized PSD-95 contributes to the overall PSD architecture and how it is involved in the increased cluster density we see in treated cultures. To answer this, we need robust live cell compatible MINFLUX Halo substrates that could allow for dual color 3D MINFLUX nanoscopy of PSD-95 pulse-chase experiments. However, the current lack of membrane-permeable HaloTag substrates compatible with multicolor MINFLUX does not enable the visualization of the old and new protein at molecular level.

In conclusion we combined different imaging methods to quantify PSD-95 at the post synapse in dependence of neuronal activity at nanoscale and molecular resolution. STED analysis of large numbers of synapses showed that neuronal activity affects the rate of protein synthesis at the postsynapse. MINFLUX nanoscopy allowed to quantitatively analyze PSD-95 organization at unprecedented resolution and to quantify how this organization is determined by its function. Here we show that PSD-95 scaffolds are not randomly distributed but organized at several levels: at synaptic level in PSD clusters, at nanoscale level in nanodomains, and at molecular level in PSD units that show a clustering behavior. Altogether we show that neuronal activity influences both the turnover and the molecular organization of the postsynapse, reveling new mechanisms acting at individual synapses which could be altered under pathological conditions (**Fig. 5**).

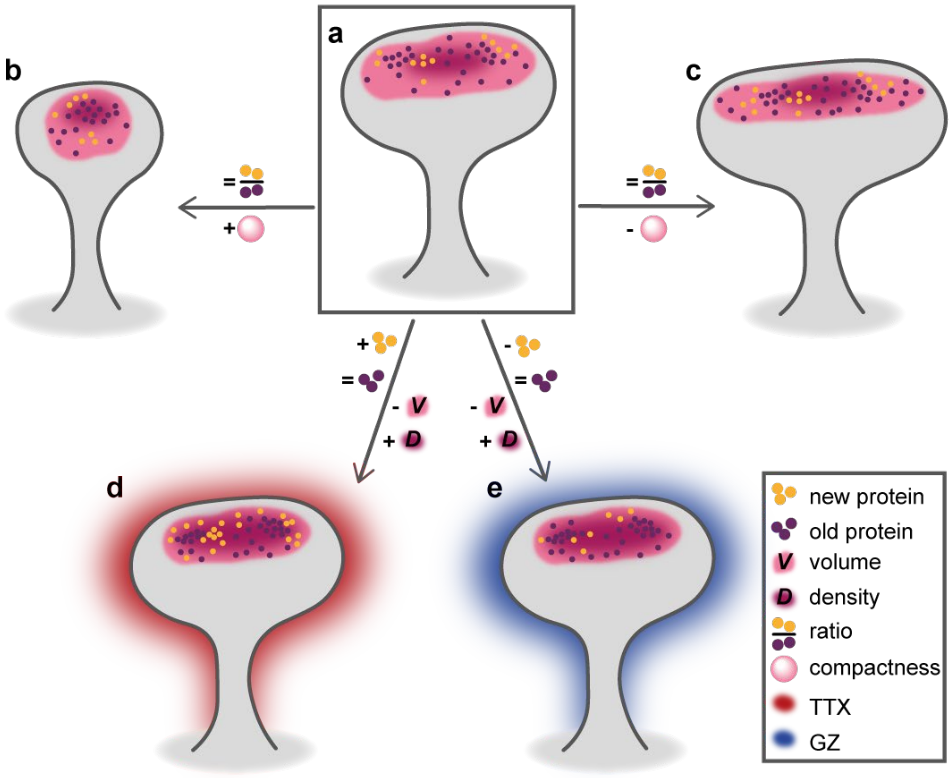

Figure 5. Model of PSD-95 nanodynamics
Summarizing all experimental findings show changes of a postsynapse (a) compared to smaller (b) and bigger (c) synaptic sites or compared to cultures silenced with TTX (d) or stimulated with GZ (e) as observed in MINFLUX (below arrow) and STED (above arrow) experiments.

Conflict of interest

S.W.H is a shareholder of Abberior Instruments GmbH, J.H is additionally affiliated with Abberior instruments GmbH, F.O. is a shareholder of NanoTag Biotechnologies GmbH

Contributions

E.D and S.W.H conceived and designed the study, C-M. G, A. R. C. D. and E.D. performed experiments J.H. established CRISPR protocol, J. H., F. O. and N. M. provided reagents, M. A. R. B. F. L. designed MF data analysis A. R. C. D. contributed data analysis tools C-M. G, M. A. R. B. F. L. and V. M. P. analyzed data, C-M. G., M. A. R. B. F. L. and E.D. wrote manuscript. All authors contributed to manuscript revision, read, and approved the submitted version.

Acknowledgements

This work has been supported by the Deutsche Forschungsgemeinschaft (DFG, SFB1286/A07 to E.D. and S.W.H) and the Max-Planck-School Matter to Life (to C-M.G.). We thank the MPI-NAT chemistry facility for the synthesis of Halo probes. We thank Eugenio F. Fornasiero and Birgit Koch for support with gene editing tools. We thank Annette Herold, Magnus-Carsten Huppertz and Birgit Koch for support with neuronal cultures and virus production.

References

Alvarez-Castelao, Beatriz; Schuman, Erin M. (2015): The Regulation of Synaptic Protein Turnover. In *The Journal of biological chemistry* 290 (48), pp. 28623–28630. DOI: 10.1074/jbc.R115.657130.

Barco, Angel; Alarcon, Juan M.; Kandel, Eric R. (2002): Expression of Constitutively Active CREB Protein Facilitates the Late Phase of Long-Term Potentiation by Enhancing Synaptic Capture. In *Cell* 108 (5), pp. 689–703. DOI: 10.1016/s0092-8674(02)00657-8.

Bingol, Baris; Schuman, Erin M. (2004): A proteasome-sensitive connection between PSD-95 and GluR1 endocytosis. In *Neuropharmacology* 47 (5), pp. 755–763. DOI: 10.1016/j.neuropharm.2004.07.028.

Blanpied, Thomas A.; Scott, Derek B.; Ehlers, Michael D. (2002): Dynamics and regulation of clathrin coats at specialized endocytic zones of dendrites and spines. In *Neuron* 36 (3), pp. 435–449.

Broadhead, Matthew J.; Bonthron, Calum; Arcinas, Lauren; Bez, Sumi; Zhu, Fei; Goff, Frances et al. (2020): Nanostructural Diversity of Synapses in the Mammalian Spinal Cord. In *Scientific reports* 10 (1), p. 8189. DOI: 10.1038/s41598-020-64874-9.

Broadhead, Matthew J.; Horrocks, Mathew H.; Zhu, Fei; Muresan, Leila; Benavides-Piccione, Ruth; DeFelipe, Javier et al. (2016): PSD95 nanoclusters are postsynaptic building blocks in hippocampus circuits. In *Scientific reports* 6, p. 24626. DOI: 10.1038/srep24626.

Bulovaite, Edita (2022): Mapping the lifetime of PSD95 at single-synapse resolution across the mouse brain in health and disease. With assistance of University of Edinburgh, Seth Grant, Noboru Komiyama.

Butko, Margaret T.; Yang, Jin; Geng, Yang; Kim, Hyung Joon; Jeon, Noo Li; Shu, Xiaokun et al. (2012): Fluorescent and photo-oxidizing TimeSTAMP tags track protein fates in light and electron microscopy. In *Nature neuroscience* 15 (12), pp. 1742–1751. DOI: 10.1038/nn.3246.

Cohen, Laurie D.; Zuchman, Rina; Sorokina, Oksana; Müller, Anke; Dieterich, Daniela C.; Armstrong, J. Douglas et al. (2013): Metabolic turnover of synaptic proteins: kinetics, interdependencies and implications for synaptic maintenance. In *PloS one* 8 (5), e63191. DOI: 10.1371/journal.pone.0063191.

Coley, Austin A.; Gao, Wen-Jun (2018): PSD95: A synaptic protein implicated in schizophrenia or autism? In *Progress in neuro-psychopharmacology & biological psychiatry* 82, pp. 187–194. DOI: 10.1016/j.pnpbp.2017.11.016.

Dankovich, Tal M.; Kaushik, Rahul; Olsthoorn, Linda H. M.; Petersen, Gabriel Cassinelli; Giro, Philipp Emanuel; Kluever, Verena et al. (2021): Extracellular matrix remodeling through endocytosis and resurfacing of Tenascin-R. In *Nature communications* 12 (1), p. 7129. DOI: 10.1038/s41467-021-27462-7.

D'Este, Elisa; Kamin, Dirk; Göttfert, Fabian; El-Hady, Ahmed; Hell, Stefan W. (2015): STED nanoscopy reveals the ubiquity of subcortical cytoskeleton periodicity in living neurons. In *Cell reports* 10 (8), pp. 1246–1251. DOI: 10.1016/j.celrep.2015.02.007.

Donlin-Asp, Paul G.; Polisseni, Claudio; Klimek, Robin; Heckel, Alexander; Schuman, Erin M. (2021): Differential regulation of local mRNA dynamics and translation following long-term potentiation and depression. In *Proceedings of the National Academy of Sciences of the United States of America* 118 (13). DOI: 10.1073/pnas.2017578118.

Ehlers, Michael D. (2003): Activity level controls postsynaptic composition and signaling via the ubiquitin-proteasome system. In *Nature neuroscience* 6 (3), pp. 231–242. DOI: 10.1038/nn1013.

Ehrlich, Ingrid; Malinow, Roberto (2004): Postsynaptic density 95 controls AMPA receptor incorporation during long-term potentiation and experience-driven synaptic plasticity. In *The Journal of neuroscience : the official journal of the Society for Neuroscience* 24 (4), pp. 916–927. DOI: 10.1523/JNEUROSCI.4733-03.2004.

Erdmann, Roman S.; Baguley, Stephanie Wood; Richens, Jennifer H.; Wissner, Rebecca F.; Xi, Zhiqun; Allgeyer, Edward S. et al. (2019): Labeling Strategies Matter for Super-Resolution Microscopy: A Comparison between HaloTags and SNAP-tags. In *Cell chemical biology* 26 (4), 584-592.e6. DOI: 10.1016/j.chembiol.2019.01.003.

Fonseca, Rosalina; Nägerl, U. Valentin; Morris, Richard G. M.; Bonhoeffer, Tobias (2004): Competing for memory: hippocampal LTP under regimes of reduced protein synthesis. In *Neuron* 44 (6), pp. 1011–1020. DOI: 10.1016/j.neuron.2004.10.033.

Frey, U.; Morris, R. G. (1997): Synaptic tagging and long-term potentiation. In *Nature* 385 (6616), pp. 533–536. DOI: 10.1038/385533a0.

Fukata, Yuko; Hirano, Yoko; Miyazaki, Yuri; Yokoi, Norihiko; Fukata, Masaki (2021): Trans-synaptic LGI1-ADAM22-MAGUK in AMPA and NMDA receptor regulation. In *Neuropharmacology* 194, p. 108628. DOI: 10.1016/j.neuropharm.2021.108628.

Galanis, Christos; Vlachos, Andreas (2020): Hebbian and Homeostatic Synaptic Plasticity-Do Alterations of One Reflect Enhancement of the Other? In *Frontiers in cellular neuroscience* 14, p. 50. DOI: 10.3389/fncel.2020.00050.

Gürth, Clara-Marie; Dankovich, Tal M.; Rizzoli, Silvio O.; D'Este, Elisa (2020): Synaptic activity and strength are reflected by changes in the post-synaptic secretory pathway. In *Scientific reports* 10 (1), p. 20576. DOI: 10.1038/s41598-020-77260-2.

Gwosch, Klaus C.; Pape, Jasmin K.; Balzarotti, Francisco; Hoess, Philipp; Ellenberg, Jan; Ries, Jonas; Hell, Stefan W. (2020): MINFLUX nanoscopy delivers 3D multicolor nanometer resolution in cells. In *Nature methods* 17 (2), pp. 217–224. DOI: 10.1038/s41592-019-0688-0.

Hanus, Cyril; Kochen, Lisa; Tom Dieck, Susanne; Racine, Victor; Sibarita, Jean-Baptiste; Schuman, Erin M.; Ehlers, Michael D. (2014): Synaptic control of secretory trafficking in dendrites. In *Cell reports* 7 (6), pp. 1771–1778. DOI: 10.1016/j.celrep.2014.05.028.

Helm, Martin S.; Dankovich, Tal M.; Mandad, Sunit; Rammner, Burkhard; Jähne, Sebastian; Salimi, Vanessa et al. (2021): A large-scale nanoscopy and biochemistry analysis of postsynaptic dendritic spines. In *Nature neuroscience* 24 (8), pp. 1151–1162. DOI: 10.1038/s41593-021-00874-w.

Iasevoli, Felice; Tomasetti, Carmine; Bartolomeis, Andrea de (2013): Scaffolding proteins of the post-synaptic density contribute to synaptic plasticity by regulating receptor localization and distribution: relevance for neuropsychiatric diseases. In *Neurochemical research* 38 (1), pp. 1–22. DOI: 10.1007/s11064-012-0886-y.

Jähne, Sebastian; Mikulasch, Fabian; Heuer, Helge G. H.; Truckenbrodt, Sven; Agüi-Gonzalez, Paola; Grewe, Katharina et al. (2021): Presynaptic activity and protein turnover are correlated at the single-synapse level. In *Cell reports* 34 (11), p. 108841. DOI: 10.1016/j.celrep.2021.108841.

Kim, Myung Jong; Futai, Kensuke; Jo, Jihoon; Hayashi, Yasunori; Cho, Kwangwook; Sheng, Morgan (2007): Synaptic accumulation of PSD-95 and synaptic function regulated by phosphorylation of serine-295 of PSD-95. In *Neuron* 56 (3), pp. 488–502. DOI: 10.1016/j.neuron.2007.09.007.

Lee, Hey-Kyoung; Kirkwood, Alfredo (2019): Mechanisms of Homeostatic Synaptic Plasticity in vivo. In *Frontiers in cellular neuroscience* 13, p. 520. DOI: 10.3389/fncel.2019.00520.

Lepore, Alessia; Taylor, Hannah; Landgraf, Dirk; Okumus, Burak; Jaramillo-Riveri, Sebastián; McLaren, Lorna et al. (2019): Quantification of very low-abundant proteins in bacteria using the HaloTag and epi-fluorescence microscopy. In *Scientific reports* 9 (1), p. 7902. DOI: 10.1038/s41598-019-44278-0.

Los, Georgyi V.; Encell, Lance P.; McDougall, Mark G.; Hartzell, Danette D.; Karassina, Natasha; Zimprich, Chad et al. (2008): HaloTag: a novel protein labeling technology for cell imaging and protein analysis. In *ACS chemical biology* 3 (6), pp. 373–382. DOI: 10.1021/cb800025k.

MacGillavry, Harold D.; Song, Yu; Raghavachari, Sridhar; Blanpied, Thomas A. (2013): Nanoscale scaffolding domains within the postsynaptic density concentrate synaptic AMPA receptors. In *Neuron* 78 (4), pp. 615–622. DOI: 10.1016/j.neuron.2013.03.009.

Masch, Jennifer-Magdalena; Steffens, Heinz; Fischer, Joachim; Engelhardt, Johann; Hubrich, Jasmine; Keller-Findeisen, Jan et al. (2018): Robust nanoscopy of a synaptic protein in living mice by organic-fluorophore labeling. In *Proceedings of the National Academy of Sciences of the United States of America*. DOI: 10.1073/pnas.1807104115.

Nair, Deepak; Hosy, Eric; Petersen, Jennifer D.; Constals, Audrey; Giannone, Gregory; Choquet, Daniel; Sibarita, Jean-Baptiste (2013): Super-resolution imaging reveals that AMPA receptors inside synapses are dynamically organized in nanodomains regulated by PSD95. In *The Journal of* *neuroscience : the official journal of the Society for Neuroscience* 33 (32), pp. 13204–13224. DOI: 10.1523/JNEUROSCI.2381-12.2013.

Nishiyama, Jun; Mikuni, Takayasu; Yasuda, Ryohei (2017): Virus-Mediated Genome Editing via Homology-Directed Repair in Mitotic and Postmitotic Cells in Mammalian Brain. In *Neuron* 96 (4), 755-768.e5. DOI: 10.1016/j.neuron.2017.10.004.

Noritake, Jun; Fukata, Yuko; Iwanaga, Tsuyoshi; Hosomi, Naoki; Tsutsumi, Ryouhei; Matsuda, Naoto et al. (2009): Mobile DHHC palmitoylating enzyme mediates activity-sensitive synaptic targeting of PSD-95. In *The Journal of cell biology* 186 (1), pp. 147–160. DOI: 10.1083/jcb.200903101.

Pape, Jasmin K.; Stephan, Till; Balzarotti, Francisco; Büchner, Rebecca; Lange, Felix; Riedel, Dietmar et al. (2020): Multicolor 3D MINFLUX nanoscopy of mitochondrial MICOS proteins. In *Proceedings of the National Academy of Sciences of the United States of America* 117 (34), pp. 20607–20614. DOI: 10.1073/pnas.2009364117.

Perez de Arce, Karen; Schrod, Nikolas; Metzbower, Sarah W. R.; Allgeyer, Edward; Kong, Geoffrey K-W; Tang, Ai-Hui et al. (2015): Topographic Mapping of the Synaptic Cleft into Adhesive Nanodomains. In *Neuron* 88 (6), pp. 1165–1172. DOI: 10.1016/j.neuron.2015.11.011.

Perez-Alvarez, Alberto; Yin, Shuting; Schulze, Christian; Hammer, John A.; Wagner, Wolfgang; Oertner, Thomas G. (2020): Endoplasmic reticulum visits highly active spines and prevents runaway potentiation of synapses. In *Nature communications* 11 (1), p. 5083. DOI: 10.1038/s41467-020-18889-5.

Pleiner, Tino; Bates, Mark; Trakhanov, Sergei; Lee, Chung-Tien; Schliep, Jan Erik; Chug, Hema et al. (2015): Nanobodies: site-specific labeling for super-resolution imaging, rapid epitope-mapping and native protein complex isolation. In *eLife* 4, e11349. DOI: 10.7554/eLife.11349.

Ries, Jonas; Kaplan, Charlotte; Platonova, Evgenia; Eghlidi, Hadi; Ewers, Helge (2012): A simple, versatile method for GFP-based super-resolution microscopy via nanobodies. In *Nature methods* 9 (6), pp. 582–584. DOI: 10.1038/nmeth.1991.

Schindelin, Johannes; Arganda-Carreras, Ignacio; Frise, Erwin; Kaynig, Verena; Longair, Mark; Pietzsch, Tobias et al. (2012): Fiji: an open-source platform for biological-image analysis. In *Nature methods* 9 (7), pp. 676–682. DOI: 10.1038/nmeth.2019.

Schmidt, Roman; Weihs, Tobias; Wurm, Christian A.; Jansen, Isabelle; Rehman, Jasmin; Sahl, Steffen J.; Hell, Stefan W. (2021): MINFLUX nanometer-scale 3D imaging and microsecond-range tracking on a common fluorescence microscope. In *Nature communications* 12 (1), p. 1478. DOI: 10.1038/s41467-021-21652-z.

Sograte-Idrissi, Shama; Schlichthaerle, Thomas; Duque-Afonso, Carlos J.; Alevra, Mihai; Strauss, Sebastian; Moser, Tobias et al. (2020): Circumvention of common labelling artefacts using secondary nanobodies. In *Nanoscale*. DOI: 10.1039/d0nr00227e.

Sun, Qian; Turrigiano, Gina G. (2011): PSD-95 and PSD-93 play critical but distinct roles in synaptic scaling up and down. In *J. Neurosci.* 31 (18), pp. 6800–6808. DOI: 10.1523/JNEUROSCI.5616-10.2011.

Sun, Ye; Smirnov, Michael; Kamasawa, Naomi; Yasuda, Ryohei (2021): Rapid Ultrastructural Changes in the PSD and Surrounding Membrane after Induction of Structural LTP in Single Dendritic Spines. In *The Journal of neuroscience : the official journal of the Society for Neuroscience* 41 (33), pp. 7003–7014. DOI: 10.1523/JNEUROSCI.1964-20.2021.

Thevathasan, Jervis Vermal; Kahnwald, Maurice; Cieśliński, Konstanty; Hoess, Philipp; Peneti, Sudheer Kumar; Reitberger, Manuel et al. (2019): Nuclear pores as versatile reference standards for quantitative superresolution microscopy. In *Nature methods* 16 (10), pp. 1045–1053. DOI: 10.1038/s41592-019-0574-9.

Turrigiano, Gina G.; Nelson, Sacha B. (2004): Homeostatic plasticity in the developing nervous system. In *Nature reviews. Neuroscience* 5 (2), pp. 97–107. DOI: 10.1038/nrn1327.

Wegner, Waja; Mott, Alexander C.; Grant, Seth G. N.; Steffens, Heinz; Willig, Katrin I. (2018): In vivo STED microscopy visualizes PSD95 sub-structures and morphological changes over several hours in the mouse visual cortex. In *Sci Rep* 8 (1), p. 219. DOI: 10.1038/s41598-017-18640-z.

Wilhelm, Jonas; Kühn, Stefanie; Tarnawski, Miroslaw; Gotthard, Guillaume; Tünnermann, Jana; Tänzer, Timo et al. (2021): Kinetic and Structural Characterization of the Self-Labeling Protein Tags HaloTag7, SNAP-tag, and CLIP-tag. In *Biochemistry* 60 (33), pp. 2560–2575. DOI: 10.1021/acs.biochem.1c00258.

Willems, Jelmer; Jong, Arthur P. H. de; Scheefhals, Nicky; Mertens, Eline; Catsburg, Lisa A. E.; Poorthuis, Rogier B. et al. (2020): ORANGE: A CRISPR/Cas9-based genome editing toolbox for epitope tagging of endogenous proteins in neurons. In *PLoS Biol* 18 (4), e3000665. DOI: 10.1371/journal.pbio.3000665.

Zolotukhin, Sergei; Potter, Mark; Zolotukhin, Irene; Sakai, Yoshihisa; Loiler, Scott; Fraites, Thomas J. et al. (2002): Production and purification of serotype 1, 2, and 5 recombinant adeno-associated viral vectors. In *Methods (San Diego, Calif.)* 28 (2), pp. 158–167. DOI: 10.1016/s1046-2023(02)00220-7.

Supplementary information

Preparation of HPN overexpressing PSD-95-Halo

HPN14DIV were transduced with AAVs for PSD-95-Halo overexpression and then treated at 21-30 DIV with 71 µM (20 µg/ml) Cycloheximide (Sigma, cat. C7698) 30 minutes prior and during the first labeling step. Labeling was performed identically to pulse-chase experiments (1st dye: 1 µM for 2 hours, 2nd dye: 500 nm for 24 hours) with a shortened intermediate incubation of 1 day.

Preparation of PAINT reagents and imaging

For site specific coupling of nanobodies we modified the procedure from Schlichthaerle et al. Briefly, anti-PSD-95 nanobodies (NanoTag Biotechnologies GmbH) were coupled to P5 (5'-TTTCAATGTAT-3') docking DNA-strands (Biomers GmbH, Ulm, Germany) through a DBCO-Maleimide crosslinker (Sigma-Aldrich, cat. 760668). The unconjugated nanobodies carried an ectopic cysteine on their C-terminus that allowed chemical coupling with the maleimide group of the crosslinker. For that, cysteine residues were reduced with 5 mM TCEP for 30 minutes at 4°C. Excess of TCEP was removed using 10 kDa centrifugal filters (Merck, cat. UFC501096) and 20x molar excess of DBCO-Maleimide crosslinker was added for 4 hours at 4°C under gentle shacking. Uncoupled crosslinker was removed using 10 kDa centrifugal filters and 5x molar excess of DNA strands were added for 1 hour at room temperature. The DNA strands, taken from Schnitzbauer et al., were functionalized on their 5'-end with an azide group that binds covalently to the DBCO group of the linker via a copper-free click reaction. The final product (PSD-95-P5) was purified using size exclusion chromatography on a GE Aekta pure 25 system equipped with a Superdex 75 Increase 10/300 GL column (Cytiva, cat. 29148721). For imaging, the complementary P5 imager strand was conjugated to Atto655 (Biomers GmbH, Ulm) and used at 333 pM concentration in imaging buffer (Massive Photonics GmbH).

References

Schlichthaerle, T.; Eklund, A.; Schueder, M., F.and Strauss; Tiede, C.; Curd, A.; Ries, J.; Peckham, M.; Tomlinson, D.; Jungmann, R. Site-Specific Labeling of Affimers for DNA-PAINT Microscopy. Angew. Chem. Int. Ed. 2018, 57, 11060–11063.

Schnitzbauer J, Strauss MT, Schlichthaerle T, Schueder F, Jungmann R. Super-resolution microscopy with DNA-PAINT. Nat Protoc. 2017 Jun;12(6):1198–228.

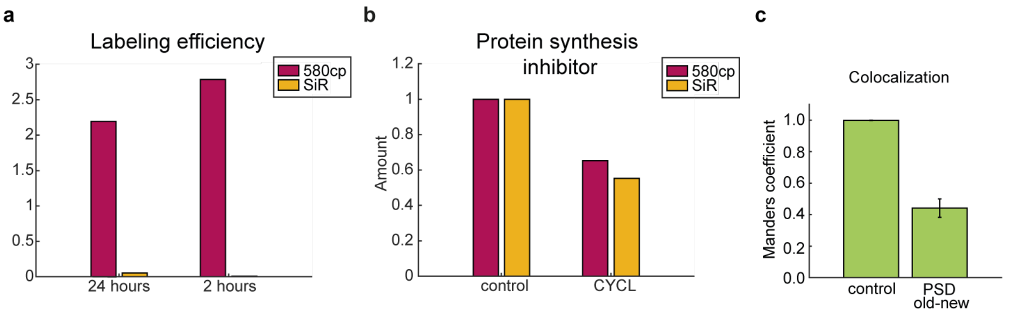

Figure S 1. Labelling controls and efficiency PSD-95-Halo

Quantification of relative overall protein turnover. Relative change of old (magenta) or new (yellow) PSD-95 protein amount (product of pixel area and mean intensity). (a) Pulse-chase labelling of endogenous PSD-95-Halo in mature neurons without incubation time and treatments after the first dye labelling. Values represent mean of 288 and 644 synaptic sites for 24 hours and 2 hours incubation of the first dye respectively from each different 3 field of views. (b) Pulse-chase labelling of PSD-95-Halo overexpression in mature neurons with the protein synthesis inhibitor cycloheximide (CYCL, 71 µM) and control (DMSO). Treatment was performed 30 minutes before and during labeling with the first dye. Values represent mean normalized to mean of controls. n=251-411 synaptic sites from 3-4 images, N= 2 independent experiments. (c) Manders co-occurrence coefficient of old and new protein in dual color STED images compared to control (same image at different resolutions). Mean and SEM values of 0.9986 ± 0.0014 and 0.4419 ± 0.0584 for control (N = 4) and PSD old new (N= 15), respectively.

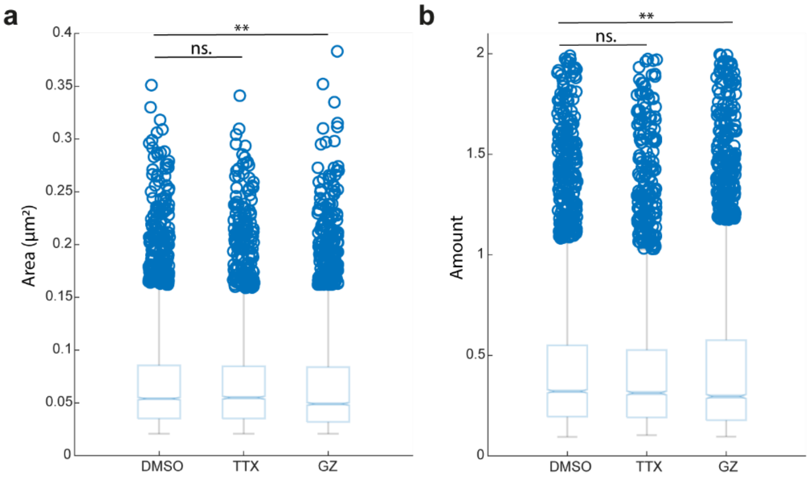

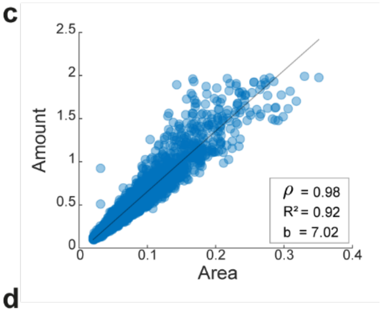

d

Treatment	ρ	b	R^2
NT	0.98	7.62	0.91
DMSO	0.98	7.02	0.92
TTX	0.98	6.91	0.93
GZ	0.97	7.39	0.88

Figure S 2. Changes in PSD-95 size and amount upon treatment

(a) Measured area and (b) amount (area * intensity) in single color STED images of mature neurons treated for 24 hours with DMSO (control), tetrodotoxin (TTX) and gabazine (GZ), labelled with sdAB against PSD-95. (Numbers of analyzed PSD clusters: control=3762, TTX=2727, GZ=3328, from 3 independent experiments). Box plots include the 25 % - 75% percentile, median is highlighted. Whiskers indicate SD and outliers are represented as individual circles. Asterisks indicate: * = $p < 0.05$, ** = $p < 0.01$, *** = $p < 0.001$, **** = $p < 0.0001$, ns= not significant. (c) Linear dependence of amount with respect to area exemplified by control experiments. Black line is a linear fit with slope (b) and coefficient of determination (R^2). P is the Spearman's correlation coefficient. (d) Linear fits and correlation coefficients for different treatments.

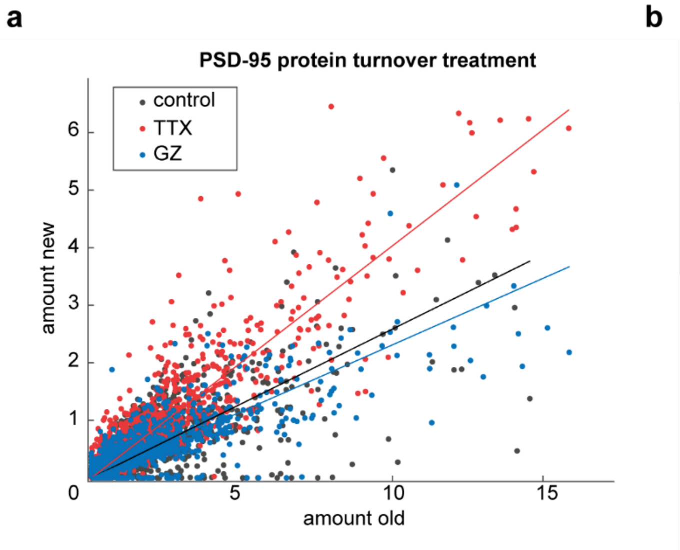

b

Treatment	b	R^2	ρ
DMSO	0.259	0.478	0.781
TTX	0.403	0.782	0.882
GZ	0.231	0.611	0.777

Figure S 3. PSD-95 turnover

(a) Relationship of the amount old PSD-95-Halo protein and new PSD-95-Halo protein. for DMSO (n=1858), TTX (n=1183) and GZ (n= 790) treated cultures from 4 independent experiments. The dependence of old and new protein amounts is described by the spearman's correlation coefficient (ρ) and linear fits. The characterization parameters are reported in table S1. (b) Characterization parameters for PSD-95 pulse-chase experiments for each treatment. Data was fit with a first order polynomial curve with slope *b*. The goodness of the fit (R^2) describes the linear dependence of amount of old vs new protein, while the correlation was assessed by Spearman's correlation coefficient (ρ). Coefficients shown for not-binned data.

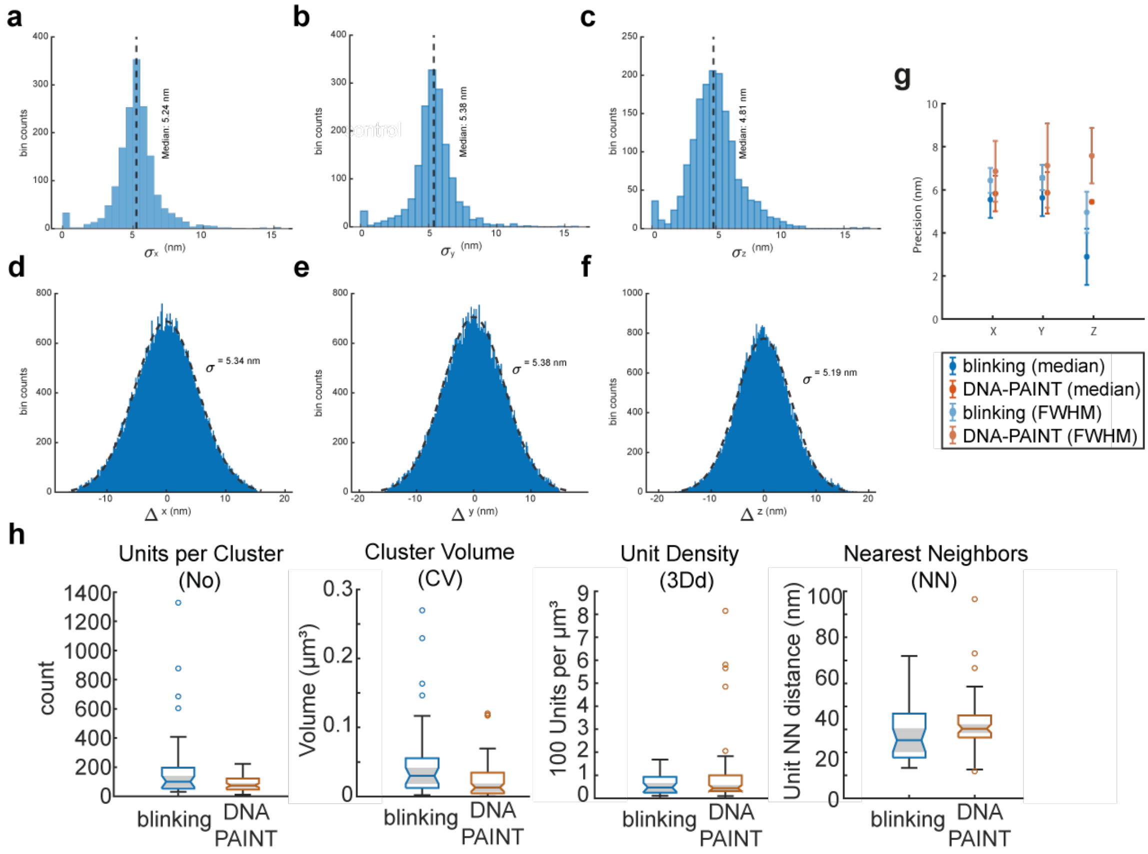

Figure S 4. MINFLUX performances

(a-f) Localization precision of one representative measurement, which is also shown in figure 3 in the main text. Precision was determined either by the median (a-c, light blue) or Gaussian fit (d-f, dark blue). (g) Quantification of localization precision in all blinking measurements (blue) compared to DNA-PAINT measurements (orange). (h) Comparison of spatial analyses of blinking and DNA-PAINT measurements.

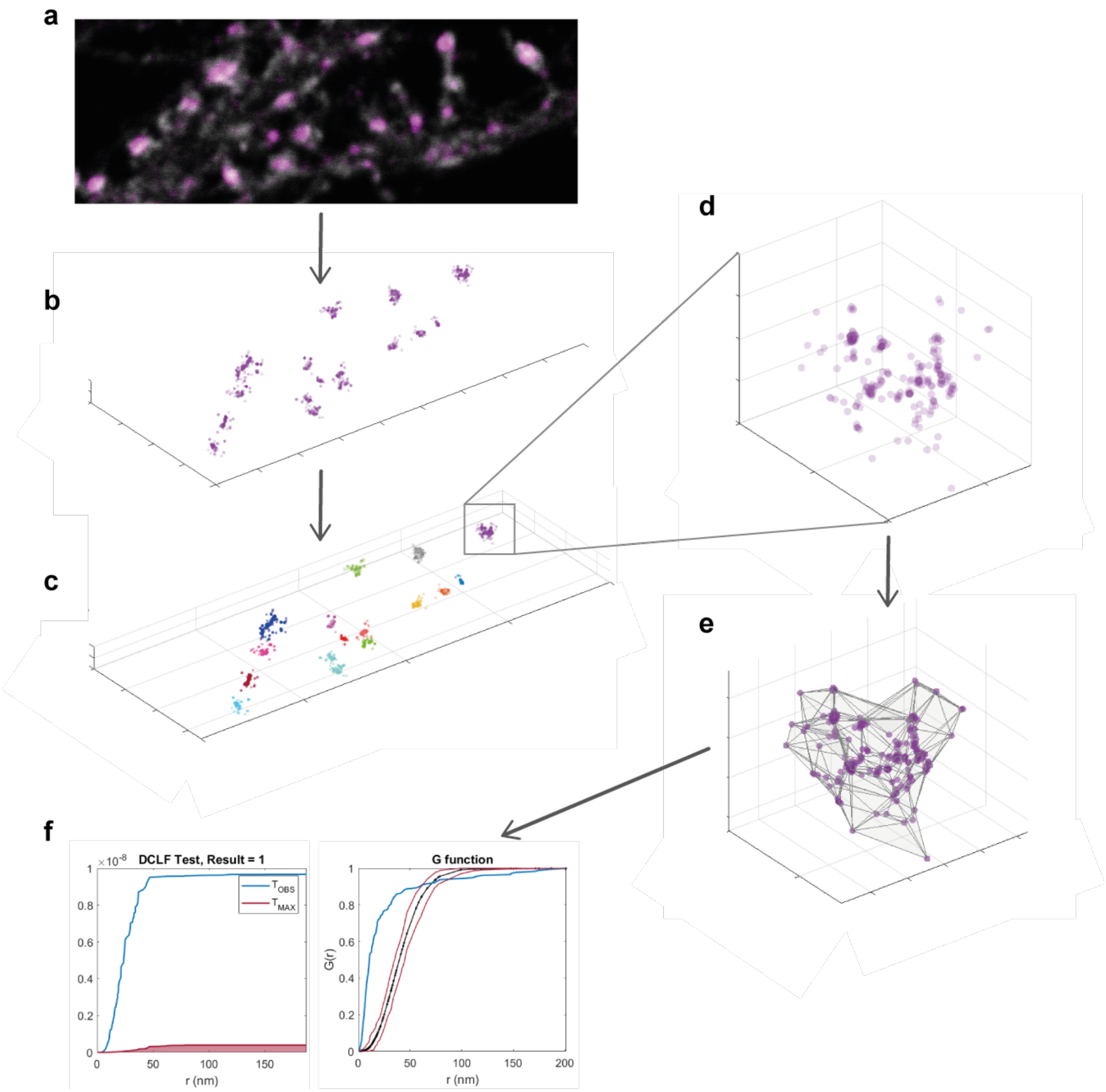

Figure S 5. Data processing workflow in MINFLUX cluster analyses

Measurements in one field of view (a) containing several synapses (b) are clustered with custom DB scan (c). Individual PSD clusters (d) are analyzed based on the alpha shape geometry (e) and their distribution is compared to random particle organization as determined by Monte Carlo simulations with G function and DCLF test (f).

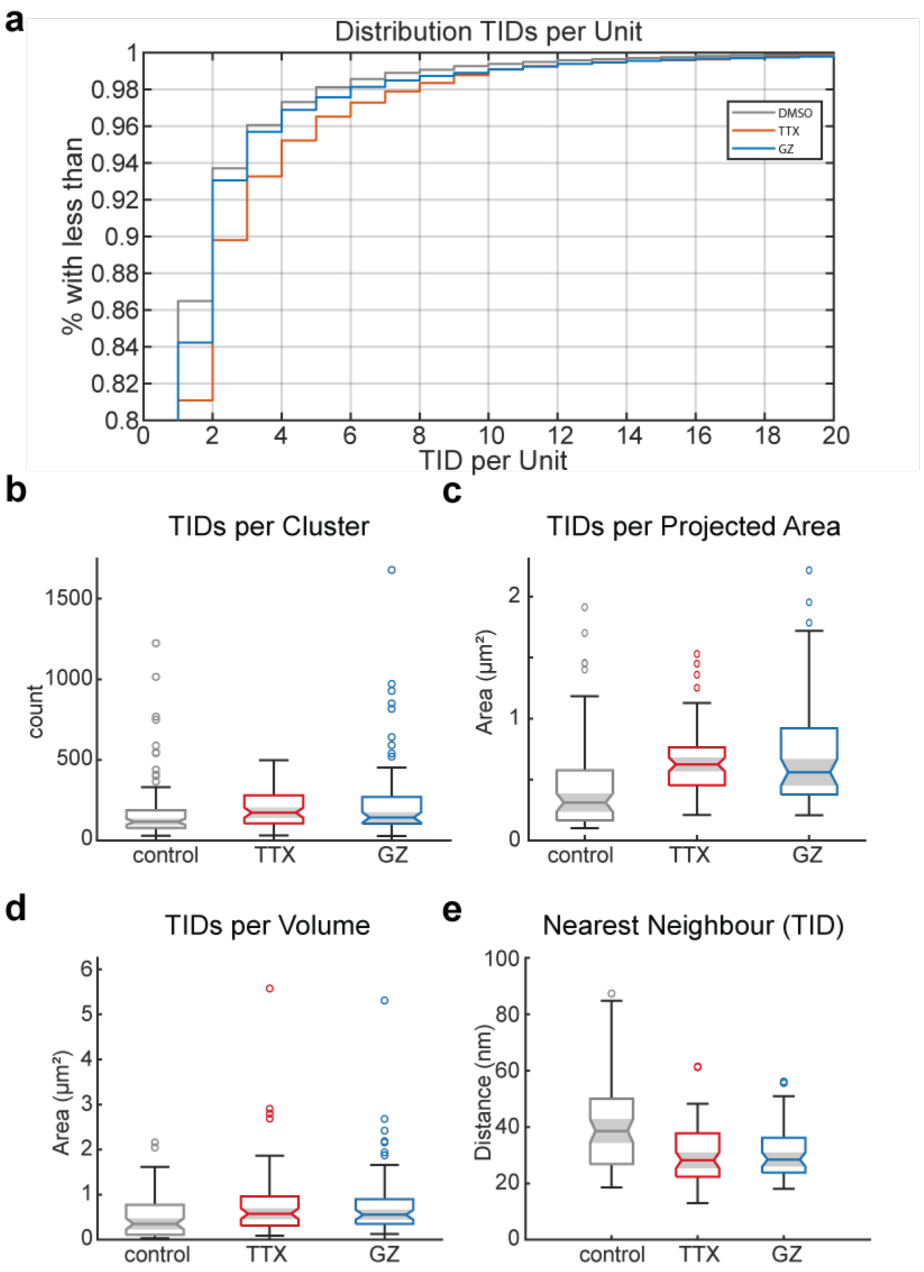

Figure S 6. MINFLUX characterization of activity dependent PSD-95 architecture based on trace IDs
(a) Cumulative distribution function of TIDs per PSD unit depending on treatment. (b), (c), (d) Quantification of trace IDs per cluster, per cluster projected area in xy-plane and per cluster volume, respectively. (e) Nearest Neighbor distances (using Euclidian metric) between each TID.

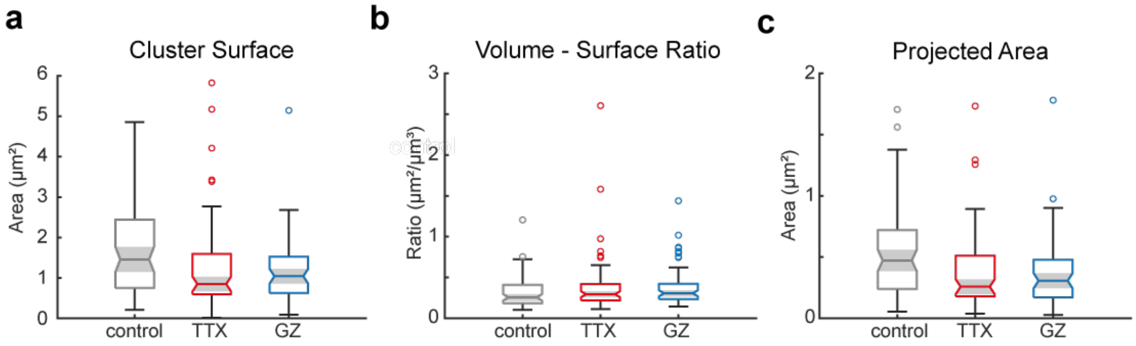

Figure S 7. MINFLUX characterization of activity dependent PSD-95 cluster morphology
(a) Quantification of cluster superficial area. (b) Cluster volume per surface ratio. (c) Quantification of cluster projected Area (in xy-plane).

Table S1 Correlation coefficients and corresponding p-values of correlation matrices of Fig. 3 and 4

	coefficient						P values					
		No	CV	Comp	3Dd	2Dd		No	CV	Comp	3Dd	2Dd
NT	CV	0.70532508					CV	3.19E-06				
	Comp	1.68E-01	0.28128342				Comp	3.42E-01	0.10706439			
	3Dd	0.06662083	-6.03E-01	-0.34239878			3Dd	0.70814467	1.60E-04	0.04745614		
	2Dd	0.62571625	-0.04935065	-0.06860199	0.78731856		2Dd	7.58E-05	0.78165219	0.69986158	3.32E-08	
	NN	-0.36977615	0.26783804	0.08724217	-7.96E-01	-0.82001528	NN	0.03136234	0.12565338	0.62369921	1.80E-08	2.96E-09
DMSO	CV	0.61011572					CV	6.22E-09				
	Comp	0.36671812	4.40E-01				Comp	0.00121191	7.84E-05			
	3Dd	0.03499463	-7.26E-01	-2.18E-01			3Dd	0.76565472	1.64E-13	0.06066186		
	2Dd	4.03E-01	-0.38540541	0.09869132	8.77E-01		2Dd	0.00034072	0.00063881	0.39956646	6.45E-25	
	NN	-0.41428805	0.32540541	-9.97E-02	-7.74E-01	-8.93E-01	NN	0.00021982	0.00438938	0.394533	3.69E-16	5.11E-27
TTX	CV	7.56E-01					CV	1.58E-14				
	Comp	-2.31E-02	1.13E-01				Comp	0.84744113	0.34255567			
	3Dd	-0.27982474	-8.20E-01	-1.68E-01			3Dd	0.01728422	1.19E-18	0.15758554		
	2Dd	0.11115488	-0.48138144	0.17705319	8.27E-01		2Dd	0.35259985	1.86E-05	0.13679441	3.70E-19	
	NN	-0.06938136	0.40677857	-0.01688211	-0.70650846	-0.75384269	NN	0.56251129	0.00039132	0.88806554	4.10E-12	2.13E-14
GZ	CV	0.74706155					CV	4.71E-12				
	Comp	1.77E-01	1.55E-01				Comp	1.72E-01	2.34E-01			
	3Dd	0.1339327	-4.52E-01	-0.04082496			3Dd	0.30345493	2.57E-04	0.75474642		
	2Dd	5.50E-01	0.00074035	0.32834479	8.18E-01		2Dd	4.32E-06	0.99548185	0.00978151	9.05E-16	
	NN	-0.67672374	-0.23104178	-0.22014807	-0.55415124	-0.78434691	NN	2.14E-09	0.07321512	0.08822698	3.60E-06	7.59E-14

Chapter 5 – Perspective

Optical nanoscopy today is constantly developing and improving. This ever-evolving new field of imaging methodology opens up new possibilities, but also challenges for life science and research applications (Dankovich and Rizzoli 2021). Thereby one single imaging method might not provide all levels of information required to understand complex and dynamic biological processes. It is therefore necessary to carefully select and combine different imaging approaches to effectively collect information on each specific biological question (Valli et al. 2021; Lemon and McDole 2020; Jacquemet et al. 2020). While MINFLUX can offer unprecedented resolution in imaging data it cannot yet achieve sufficient throughput for large quantitative studies required for heterogenous populations. Therefore, it needs complementing strategies such as STED or confocal microscopy to add quantitative information, albeit at lower resolution. Strategic selection and combination of different nanoscopy methods is thus a promising approach to understand the synaptic molecular landscape.

In this thesis, state of the art microscopy techniques were applied for the quantitative analysis of the postsynaptic compartment. We systematically quantify several different proteins at the postsynapse as well as synaptic makers to correlate synaptic traits with synaptic composition and thereby connect synaptic structure and function.

This was achieved by combining multicolour nanoscopy, gene editing tools, and labelling strategies in neuronal cultures, synaptic stimulation and activity markers, microscopy techniques with the highest achievable resolution at the required throughput, and quantitative semi-automated analysis routines. Thereby the described studies greatly benefit from the strategic combination of expertise from neurobiology, chemistry, data science, and optical physics.

This interdisciplinary approach allowed us to tailor and optimize the experimental setup – starting from sample preparation, over image acquisition, image segmentation to data processing and simulation - to each specific biological question, and aiming at achieving the highest possible output of information. Although the experimental approach was tailored to its needs, several technical aspects still put limitations on this study.

Firstly, our *ex vivo* model system of dissociated cultures, while providing optimal specimen aspects for our selected imaging approaches, might not fully reflect the complexity of a 3D synaptic environment as found in organisms. Non-neuronal components of intact brain tissue such as glial cells (as part of the tripartite synapse) or the extracellular matrix can have strong effects on synaptic signalling (Dankovich and Rizzoli 2022; Noriega-Prieto and Araque 2021). Therefore, our quantitative measures provide information on the basic mechanisms of synapses but might differ from findings of *in vivo* studies. A confirmation of the results in *in vivo* models or acute brain slices would be needed to further validate our results.

Secondly, our analyses focused mainly on 2D imaging data, which is advantageous for imaging speed and therefore sample throughput, but on the other hand renders a projection of the three-dimensional structure of individual synapses. This is a particular caveat when distinguishing between presynaptic and postsynaptic compartments that can overlap in cell culture models. To identify the synapse orientation manually is therefore sometimes difficult or could introduce artefacts into our analyses. Adding 3D information to STED experiments could therefore add a higher level of information but at the same time drastically increases image acquisition times and resolution.

Moreover, all our imaging experiments were performed in fixed cells to ensure optimal imaging conditions and a robust, reproducible sample preparation workflow. Hence, we were limited to end-point observations of otherwise dynamic processes. In future the increasing availability of live cell compatible probes for long-term nanoscopy methods and the increasing speed of the imaging process might enable to validate our findings in a live cell context.

While our efforts to gain quantitative information on the synaptic environment led to the characterization of a high number of synapses (hundreds to thousands per condition) our data can only represent a fraction of the entire synaptome. The heterogeneity of the synapse population within and across brain regions and their changes over time can therefore not or only partly be represented in our selection of sample (Cizeron et al. 2020). We exclusively used hippocampal neurons, without distinguishing the region from which they stemmed from. Furthermore, a first bias lies in the choice of cells which are being imaged.

A second bias lies in the (partly-) manual segmentation workflows, that might have favoured subsets of spines based on morphological features of the postsynapse. Especially shaft synapses can therefore be under-represented in the described studies. Further automatization in the image acquisition and segmentation workflow can be used to minimize such biases.

For our multicolour analyses, we were able to draw a link between different synaptic aspects such as size, morphology, organelle composition, activity, and the cytoskeleton, however in separate experiments. While it was possible to comparatively analyse some of these properties simultaneously, an overall comparison of all respective markers is still challenging, since the availability of spectral channels and orthogonal labels is limited. The ongoing development of multiplexing strategies will allow to compare multiple synaptic markers simultaneously instead of separately (Butkevich et al. 2021; Sograte-Idrissi et al. 2020; Oleksiievets et al. 2022; Narayanasamy et al. 2021). This then could reduce the influence of sample variability, allow for additional information related to the interplay of the different structures, and ultimately increase the throughput.

A general limitation not only for multiplexing approaches lies in the quality of the probe used for targeting the structures of interest. Since in fluorescence microscopy we visualize fluorophores and not target proteins directly, even the perfect imaging experiment can only be as specific as the applied fluorescent reporter. Most reagents used during these studies do not achieve complete labelling of target structures or can even introduce background labelling. Although individual protocols were always optimized to achieve best possible results with the given reagents, the end result is limited by the individual affinity and specificity of the probes. Thereby especially the specificity of immunolabelling has to be considered and tested. The use of protein tags and direct binding fluorescent probes which do not rely on epitope accessibility can be superior to antibodies or nanobodies. However, they require the genetic manipulation of the cells and, in the case of small direct binding probes, only few of them are currently available.

In future, the approaches described in this thesis together with the reinforcement of correlative imaging approaches and integrated automated image processing will help to establish a high-detailed dynamic molecular map of the synapse. This will help to understand synaptic plasticity in the context of learning and memory.

Previous scientists have set fundamentals of our biological understanding with the limited methods available to them at the time. With the growing possibilities that new nanoscopic methods can offer it is now our responsibility to fill the gaps of knowledge, that previously could not be answered, to further refine previous findings by limited methods at now constantly increasing resolution and thereby to push forward the accumulation of new discoveries in life sciences.

References

Butkevich, Alexey N.; Weber, Michael; Cereceda Delgado, Angel R.; Ostersehlt, Lynn M.; D'Este, Elisa; Hell, Stefan W. (2021): Photoactivatable Fluorescent Dyes with Hydrophilic Caging Groups and Their Use in Multicolor Nanoscopy. In *Journal of the American Chemical Society* 143 (44), pp. 18388–18393. DOI: 10.1021/jacs.1c09999.

Cizeron, Mélissa; Qiu, Zhen; Koniaris, Babis; Gokhale, Ragini; Komiyama, Noboru H.; Fransén, Erik; Grant, Seth G. N. (2020): A brainwide atlas of synapses across the mouse life span. In *Science (New York, N.Y.)* 369 (6501), pp. 270–275. DOI: 10.1126/science.aba3163.

Dankovich, Tal M.; Rizzoli, Silvio O. (2021): Challenges facing quantitative large-scale optical super-resolution, and some simple solutions. In *iScience* 24 (3), p. 102134. DOI: 10.1016/j.isci.2021.102134.

Dankovich, Tal M.; Rizzoli, Silvio O. (2022): The Synaptic Extracellular Matrix: Long-Lived, Stable, and Still Remarkably Dynamic. In *Frontiers in synaptic neuroscience* 14, p. 854956. DOI: 10.3389/fnsyn.2022.854956.

Jacquemet, Guillaume; Carisey, Alexandre F.; Hamidi, Hellyeh; Henriques, Ricardo; Leterrier, Christophe (2020): The cell biologist's guide to super-resolution microscopy. In *J Cell Sci* 133 (11). DOI: 10.1242/jcs.240713.

Lemon, William C.; McDole, Katie (2020): Live-cell imaging in the era of too many microscopes. In *Current opinion in cell biology* 66, pp. 34–42. DOI: 10.1016/j.ceb.2020.04.008.

Narayanasamy, Kaarjel K.; Stojic, Aleksandar; Li, Yunqing; Sass, Steffen; Hesse, Marina R.; Deussner-Helfmann, Nina S. et al. (2021): Visualizing Synaptic Multi-Protein Patterns of Neuronal Tissue With DNA-Assisted Single-Molecule Localization Microscopy. In *Frontiers in synaptic neuroscience* 13, p. 671288. DOI: 10.3389/fnsyn.2021.671288.

Noriega-Prieto, José Antonio; Araque, Alfonso (2021): Sensing and Regulating Synaptic Activity by Astrocytes at Tripartite Synapse. In *Neurochemical research* 46 (10), pp. 2580–2585. DOI: 10.1007/s11064-021-03317-x.

Oleksiievets, Nazar; Sargsyan, Yelena; Thiele, Jan Christoph; Mougios, Nikolaos; Sograte-Idrissi, Shama; Nevskyi, Oleksii et al. (2022): Fluorescence lifetime DNA-PAINT for multiplexed super-resolution imaging of cells. In *Communications biology* 5 (1), p. 38. DOI: 10.1038/s42003-021-02976-4.

Sograte-Idrissi, Shama; Schlichthaerle, Thomas; Duque-Afonso, Carlos J.; Alevra, Mihai; Strauss, Sebastian; Moser, Tobias et al. (2020): Circumvention of common labelling artefacts using secondary nanobodies. In *Nanoscale*. DOI: 10.1039/d0nr00227e.

Valli, Jessica; Garcia-Burgos, Adrian; Rooney, Liam M.; Vale de Melo E Oliveira, Beatriz; Duncan, Rory R.; Rickman, Colin (2021): Seeing beyond the limit: A guide to choosing the right super-resolution microscopy technique. In *The Journal of biological chemistry* 297 (1), p. 100791. DOI: 10.1016/j.jbc.2021.100791.

List of figures

Chapter 1 – Introduction and Overview

Chapter 2 - Synaptic Secretory Elements

Chapter 3 - Neurofilaments at the Postsynapse

Chapter 4 - PSD-95 Turnover and Nano-dynamics

List of abbreviations

APD	avalanche photodiodes
CFR	centre frequency ratio
CSR	complete spatial randomness
CYCL	cycloheximide
DBSCAN	density-based spatial clustering of applications with noise algorithm
DCLF	Diggle-Cressie-Loosmore-Ford
DIV	day *in vitro*
eps	search radius
ER	endoplasmic reticulum
ERGIC	ER-Golgi intermediate compartment
FWHM	full with half maximum
GFP	green fluorescent protein
GZ	gabazine
IgG	immunoglobulin
LTP	long-term potentiation
minPoints	minimum number of neighbours
NF	neurofilament
NFH	neurofilament heavy
NFL	neurofilament light
NFM	neurofilament medium
NMDA	N-methyl-D-aspartate
NN	median nearest neighbourhood distance
PALM	photoactivated localization microscopy
POI	protein of interest
PSD	postsynaptic density
PSF	point spread function
ROI	region of interest
SA	spine apparatus
sdAB	single domain antibody
SEM	standard error of the mean
STED	stimulated emission depletion
STORM	stochastic optical reconstruction microscopy
SYT1	synaptotagmin-1
TGN	trans-Golgi network
TID	trace identification
TTX	tetrodotoxin